Investigations of the Dry Snow Zone of the Greenland Ice Sheet Using QuikSCAT

Kevin R. Moon

A thesis submitted to the faculty of
Brigham Young University
in partial fulfillment of the requirements for the degree of

Master of Science

David G. Long, Chair
Richard W. Christiansen
Dah Jye Lee

Department of Electrical and Computer Engineering

Brigham Young University

August 2012

ABSTRACT

Investigations of the Dry Snow Zone of the Greenland Ice Sheet Using QuikSCAT

Kevin R. Moon
Department of Electrical and Computer Engineering
Master of Science

The Greenland ice sheet is an area of great interest to the scientific community due to its role as an important bellwether for the global climate. Satellite-borne scatterometers are particularly well-suited to studying temporal changes in the Greenland ice sheet because of their high spatial coverage, frequent sampling, and sensitivity to the presence of liquid water. The dry snow zone is the largest component of the Greenland ice sheet and is identified as the region that experiences negligible annual melt. Due to the lack of melt in the dry snow zone, backscatter was previously assumed to be relatively constant over time in this region. However, this thesis shows that a small seasonal variation in backscatter is present in QuikSCAT data in the dry snow zone. Understanding the cause of this seasonal variability is important to verify the accuracy of QuikSCAT measurements, to better understand the ice sheet conditions, and to improve future scatterometer calibration efforts that may use ice sheets as calibration targets.

This thesis provides a study of the temporal behavior of backscatter in the dry snow zone of the Greenland ice sheet focusing on seasonal variation. Spatial averaging of backscatter and the Karhunen-Loève transform are used to identify and study the dominant patterns in annual backscatter behavior. Several QuikSCAT instrumental parameters are tested as possible causes of seasonal variation in backscatter in the dry snow zone to verify the accuracy of QuikSCAT products. None of the tested parameters are found to be related to seasonal variation. Further evidence is given that suggests that the cause of the seasonal variation is geophysical and several geophysical factors are tested. Temperature is found to be highly related to dry snow backscatter and therefore may be driving the seasonal variation in backscatter in the dry snow zone.

Keywords: Greenland ice sheet, scatterometer calibration, QuikSCAT, seasonal variation, dry snow zone

ACKNOWLEDGMENTS

Thank you to Dr. David Long for your advice, guidance, and encouragement. You struck a good balance between guiding me to the next step and giving me enough freedom to pursue my ideas. I have become a much better researcher working for you.

Thank you to the Rocky Mountain NASA Space Grant Consortium and NASA for financially assisting me in my research.

To my parents Lee and Kathy Moon, thank you for encouraging me to be willing to take the paths that are not always the easiest.

To my wife Kyra, thank you for your faith and support in me. I have enjoyed the time we have spent working together in school. You inspire me to be continually learning and improving.

To my son Joseph, this is for you.

Table of Contents

List of Tables

List of Figures

Chapter 1

Introduction

Satellite-borne scatterometers are microwave radars designed to estimate the wind velocity over the earth's oceans. The wind estimates are useful for studying the earth's climate and for forecasting and monitoring weather patterns including hurricanes. Because of their global coverage, high resolution, and frequent sampling, satellite-borne scatterometers are ideal for estimating wind vectors [1].

In addition to their primary purpose of wind observation, spaceborne scatterometers have been used for tracking icebergs, mapping the sea ice extent [2], measuring deforestation in the Amazon [3], and monitoring important indicators of the global climate such as the Greenland and Antarctic ice sheets [4]. Scatterometers are well-suited to these studies for several reasons. First, satellite-borne scatterometers provide consistent and frequent observations of these regions. This is especially true in the polar regions where some satellites achieve multiple passes per day. Second, unlike optical wavelengths, microwaves penetrate clouds and do not require solar illumination. Thus measurements can be obtained night and day and in nearly all weather conditions. This results in consistent temporal and spatial coverage.

1.1 The Greenland Ice Sheet

Spaceborne scatterometers are particularly useful in studies of the Greenland ice sheet. The Greenland ice sheet is an area of great interest to the scientific community, which stems from its role as an important bellwether for the global climate. Greenland is almost entirely covered by a large ice sheet that contains 8% of the earth's ice and 11% of the global glacier surface area [5]. Because of its size, the Greenland ice sheet affects the global sea level as well as the earth's radiation budget.

The global sea level is affected by the mass balance of ice sheets such as those in Greenland and Antarctica. It is estimated that the Greenland ice sheet contains enough water to raise sea levels by 7 meters [5]. Because of this, many studies have focused on melt detection, accumulation, and changes in the mass balance of the Greenland ice sheet.

The earth's radiation budget is defined as the balance between the radiation absorbed and emitted by the earth's surface. Changes in melt extent and duration on Greenland can affect the radiation budget. Dry snow has a high albedo. Thus dry snow reflects most of the incident solar radiation. However, the presence of liquid water in snow reduces the albedo which results in an increase in solar radiation absorption [6].

Because of the ice sheet's influence on sea level and the radiation budget, knowledge of temporal changes in the ice sheet is crucial to understanding changes in the global climate. Due to the harsh climate and large size of the Greenland ice sheet, *in situ* (on-site) measurements are difficult to obtain with sufficient spatial coverage. In contrast, scatterometer measurements are available for the entire ice sheet with the earliest measurements collected in 1978. Additionally, recent scatterometers have observed the ice sheet multiple times per day. Scatterometer measurements are also useful for Greenland studies because of their sensitivity to snow grain size, the presence of liquid water, and subsurface features. This sensitivity allows scatterometers to be used in tracking snow accumulation, measuring melt extent and duration, and mapping the ice facies of the Greenland ice sheet.

1.2 Research Problem

The Greenland ice sheet is divided into zones or facies which are distinguished by their melting characteristics. The largest of these facies is the dry snow zone which is defined as the region where negligible melt occurs throughout the entire year. Understanding the properties of the dry snow zone is important because of its role in the earth's climate.

Since the presence of liquid water is the primary parameter affecting radar backscatter in snow and ice [4], backscatter was previously assumed to be relatively constant in dry snow since the dry snow zone experiences little to no melt. However, in [4] an anomaly in Seasat-A scatterometer (SASS) data in the dry snow region is briefly mentioned. My studies indicate that a similar unanticipated anomaly is present in QuikSCAT data. This anomaly is a seasonal variation in backscatter in the dry snow zone. The seasonal variation is characterized by a slight decrease in backscatter during the summer months. Although the decrease in backscatter is small (typically less than 1 dB), this seasonal variation is present throughout the entire dry snow zone. This suggests that the backscatter in the dry snow zone may not be as constant as was previously assumed.

Studies of the seasonal variation in backscatter are necessary for several reasons. First, it is important to know whether the cause of the seasonal variation is instrumental or geophysical. If the cause is instrumental, the accuracy of all scatterometer products could be compromised. Correction of the seasonal variation would then be necessary to ensure accuracy in the studies that depend on scatterometer observations.

Second, if the cause is geophysical, understanding the cause could lead to better understanding and measurement of ice sheet conditions. For example, if temperature is the cause of seasonal variation, then the variation in backscatter may be useful for estimating temperatures at the ice sheet surface.

Finally, predicting the seasonal variation could lead to improved scatterometer calibrations. Studies using scatterometer data require accurate calibration of the scatterometer [7]. Although scatterometers are calibrated prior to launch, system degradation requires scatterometers to be calibrated after launch as well [8]. Accurate post-launch calibration can be achieved by using radar backscatter data from natural land targets with isotropic and temporally constant backscatter. Currently, post-launch scatterometer calibration is performed using data collected from regions such as the Amazon rain-forest, the Greenland and Antarctic ice sheets, and the Sahara Desert, with calibration most often performed using data from the Amazon [9, 10, 11]. However, in [8], the authors find that the backscatter in parts of the Greenland ice sheet varies less than in other regions. This suggests that the Greenland ice sheet, specifically the dry snow zone, may be better suited for scatterometer calibration than other regions of the earth.

Predicting the seasonal variation in the dry snow zone could lead to further improvement in scatterometer calibration. Studying the seasonal variation may lead to a model that can be used to estimate future seasonal variation and correct the radar calibration. The improved calibration will result in greater accuracy in all scatterometer applications.

1.3 Thesis Statement

This thesis provides a study of the temporal behavior of backscatter in the dry snow zone of the Greenland ice sheet focusing on seasonal variation. The dominant patterns in backscatter in the dry snow zone are identified. Seasonal variation is found to be the dominating temporal pattern. Possible instrumental causes of seasonal variation are explored and ruled out. Evidence is then given that suggests that the cause of seasonal variation is geophysical with temperature as the leading candidate.

1.4 Research Contributions

This thesis presents three primary research contributions:

1. Observations of temporal behavior of backscatter in dry snow are provided. The Karhunen-Loève (KL) expansion or transform is used to identify and study the dominant patterns in annual backscatter behavior including seasonal variation.
2. Possible instrumental causes of seasonal variation are investigated and ruled out. These possible causes include incident angle variation, orbital drift, and local time of day variation.
3. Strong evidence of a geophysical cause of seasonal variation is given. Evidence is presented that suggests that temperature is the cause of seasonal variation.

1.5 Organization

This thesis is organized as follows. Background information is given in Chapter 2. This includes a discussion of the normalized radar cross section of scatterometers, the electromagnetic properties of ice and snow, the ice facies and their electromagnetic properties, an accumulation map of Greenland, the scatterometers used in this thesis, image reconstruction of scatterometer data, and *in situ* data used in this thesis. Chapter 3 provides some general observations of backscatter in the Greenland ice sheet focused on the dry snow zone. Chapter 4 explores the possible instrumental causes of seasonal variation while possible geophysical causes are explored in Chapter 5. Chapter 6 then concludes with suggestions for future work.

Chapter 2

Background

This chapter provides background information for the remainder of the thesis. First, the normalized radar cross section (NRCS) in the context of scatterometers is described. The electromagnetic properties of ice and snow are then given followed by a description of the ice facies and their electromagnetic properties. A brief description of the scatterometer data used in the thesis is given followed by an explanation of the Scatterometer Image Reconstruction (SIR) algorithm. This chapter then concludes with a description of the *in situ* data record used in this thesis.

2.1 Scatterometers and the NRCS

Scatterometers use active microwave remote sensing to obtain information about the earth. Scatterometers transmit electromagnetic energy in the microwave region of the electromagnetic spectrum. The part of the earth illuminated by the pulse reflects some of the energy to the receiver. For scatterometers, the receive and transmit antenna are typically the same. The received power P_r can be determined using the monostatic radar equation [12]

$$P_r = \frac{P_t G^2 \lambda^2 A}{(4\pi)^3 R^4} \sigma^0 \tag{2.1}$$

where P_t is the transmit power, G is the gain of the antenna, λ is the wavelength of the transmitted signal, A is the area of the illuminated region of the earth, R is the range from the antenna to the illuminated area, and σ^0 is the NRCS of the illuminated region.

The NRCS is a function of the radar operating frequency, incidence and azimuth angles, pulse polarization, and the scattering properties of the illuminated area. The incidence angle θ describes the angle between the propagating direction of the pulse and the surface normal. Azimuth angle ϕ describes the angle between the flight path of the scatterometer and the projection of the propagation path onto the plane of the scatterometer.

The scattering properties of the illuminated area are generally divided into surface scattering and volume scattering. Both depend on the electromagnetic properties of the illuminated area and can contribute to σ^0.

2.2 Electromagnetic Properties of Ice and Snow

Surface scattering occurs when the incident pulse reflects off the boundary between two distinct mediums. This scattering depends on the roughness and the reflection coefficient at the surface.

Volume scattering occurs when the pulse penetrates the surface, reflects off buried objects, and transmits back through the surface. In snow or ice, the buried objects that cause the scattering can include large ice structures as well as the snow grains. In dry snow, parameters such as snow density and grain size can affect σ^0. Volume scattering is the primary contributor to σ^0 in ice and snow.

In snow and ice, the presence of liquid water causes a large decrease in σ^0 and is the primary parameter that affects σ^0 [4]. As liquid water content increases in ice and snow, the conductivity increases which causes the reflection coefficient to increase. Thus melting causes surface scattering away from the radar to dominate over volume scattering. Additionally, an increase of liquid water in snow increases the extinction coefficient. More of the transmitted signal becomes attenuated which results in further decrease in volume scatter. Therefore, when melting occurs, backscatter decreases dramatically.

Figure 2.1 demonstrates this phenomenon. In dry snow, much of the signal penetrates the upper layer while some of the signal is reflected away by surface scattering. Some of the energy in the transmitted pulse reflects off the subsurface ice structure and back out of the snow to the receiver causing a high return. Volume scattering from individual snow grains is not represented in this figure although it is also present. In contrast, less of the signal transmits through the snow surface when the snow is wet. Surface scattering dominates and most of the signal is reflected away. The backscatter in this case depends on the surface roughness.

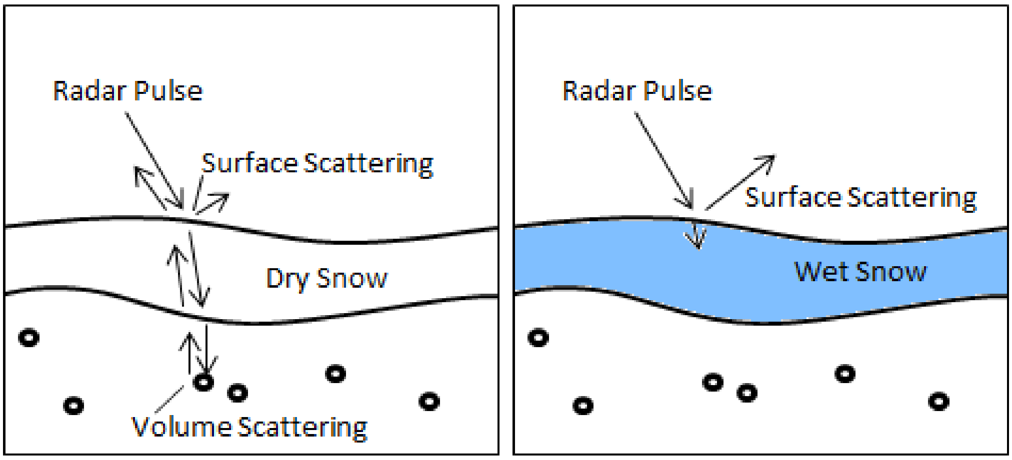

Figure 2.1: Diagram demonstrating scattering in dry (left) and wet snow (right). The small circles represent subsurface ice structures.

2.2.1 Melt Detection

Because of the sensitivity of σ^0 to liquid water, many studies have used scatterometers to detect melting on ice sheets [13, 4, 14, 15, 16, 17]. Melt characteristics can then be used to infer information about the ice sheet.

Multiple melt detection algorithms over Greenland have been developed for scatterometers and radiometers [13]. One of the algorithms designed for QuikSCAT is termed the Q-α method [13]. The Q-α method classifies a pixel as melting when σ^0 drops 3 dB below the winter mean. The 3 dB threshold corresponds to a 1% liquid moisture content of the snow and a 3.8 cm layer of wet snow.

One advantage of the Q-α method is that it is simple to implement. Another advantage is the melt extent identified by this method is consistent with other melt detection algorithms [13]. Because of these two advantages, I use the Q-α method with QuikSCAT data for melt detection in this thesis.

2.3 Ice Facies

The Greenland ice sheet is divided into zones or facies which are distinguished by their melting and refreezing characteristics. They were first identified using field data [18] as the ablation zone, the wet (soaked) snow zone, the percolation zone, and the dry snow zone. Fig. 2.2 shows an attempt to map the facies from [18].

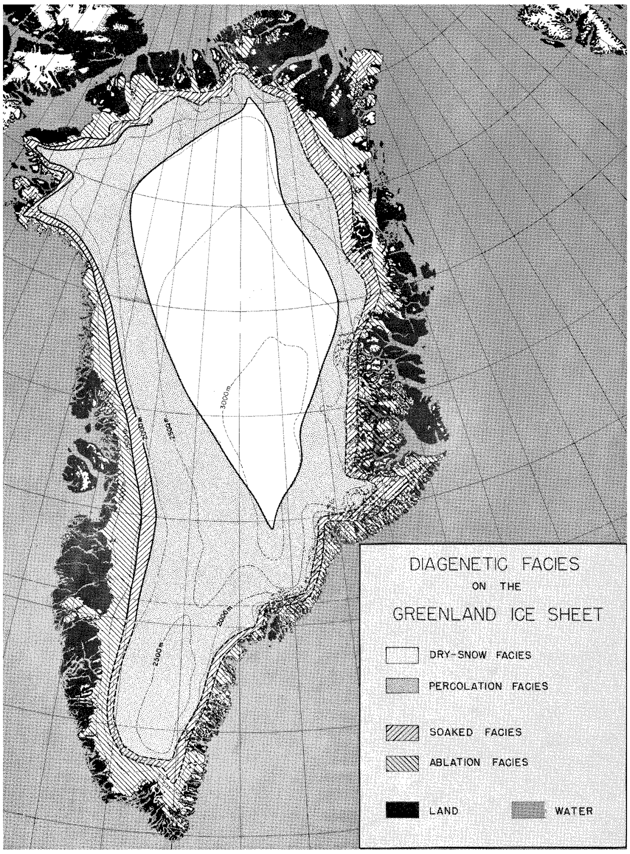

Figure 2.2: Benson [18] map of the Greenland ice facies from field data.

The sensitivity of σ^0 to liquid water can be exploited by satellite-borne scatterometers to map melting trends and properties of the Greenland ice sheet. The melt history and other key features have been used to map the location of the facies on Greenland and the Canadian Arctic ice caps [4, 15, 19, 16, 20, 21].

In the following, a description of each of the ice facies and their radar characteristics is given. For visualization, an illustration of a profile of the ice facies is given in Fig. 2.3.

2.3.1 Ablation Zone

The ablation zone is defined as the region of the ice sheet where the annual snow accumulation melts away leaving only bare ice. It is located at the outer edge of the Greenland ice sheet [23].

The ablation zone typically has lower backscatter during the winter than the wet snow zone. This is due to the comparatively smooth surface of the exposed ice in the ablation

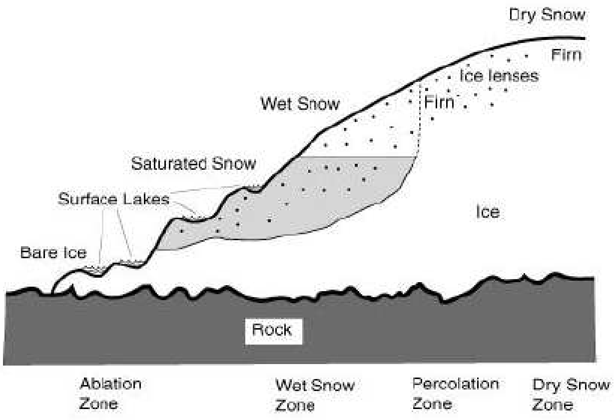

Figure 2.3: Illustration of the Greenland ice facies profile [22].

zone. However, in the summer, σ^0 is typically higher in the ablation zone than in the wet snow zone since wet snow has lower backscatter than bare ice [20]. For classification, the combination of low altitude with low winter backscatter generally denotes the ablation zone.

The σ^0 behavior in the ablation zone can cause inaccuracies in melt detection algorithms such as the Q-α method. If accumulation is low, the bare ice may be exposed early in the melt season. Thus σ^0 may return close to or even above the previous winter's backscatter levels even though the bare ice may be melting. σ^0 may even increase during melt if the exposed bare ice has a higher backscatter than the snow covered ice [15]. Because of this, the Q-alpha method and other similar melt detection algorithms are not as accurate in the ablation zone.

2.3.2 Wet Snow Zone

The wet snow zone is defined as the region where the accumulation between melt seasons is completely soaked in the summer [23]. Because of the soaked snow, the wet snow region experiences the lowest backscatter during the melt season. However, backscatter increases and returns to winter levels during refreeze as ice structures form and liquid water disappears.

Subsurface ice structures such as ice lenses and layers are the source of the highest backscatter in snow [4]. While these structures may be present in wet snow, the upper layer of wet snow typically freezes into a hard ice layer in winter. This layer has more surface scattering which results in a reduced backscatter from subsurface structures. This results in a lower winter backscatter in the wet snow zone than the percolation zone [15]. However, the presence of subsurface ice structures such as ice lenses and layers still contribute to a higher winter backscatter in the wet snow zone than in the ablation zone [20].

2.3.3 Percolation Zone

Snow in the percolation zone experiences less melt than snow in the wet snow zone. In the percolation zone, surface melt water percolates down through the snow. When refreezing occurs, the percolated water forms ice glands, lenses, and layers [23].

The backscatter in the percolation zone varies throughout the year. During the melt season, σ^0 quickly drops due to the presence of liquid water. However upon refreeze, σ^0 increases to the highest level of all the facies [4]. Based on field tests, the high winter backscatter in the percolation zone is attributed to the ice lenses and layers formed during the refreeze period [24].

2.3.4 Dry Snow Zone

The dry snow zone is the largest facie and is defined as the region of the ice sheet that experiences negligible melt throughout the year [23]. Because of this, the dry snow zone is limited to higher altitudes and latitudes.

Compared to the other facies, the backscatter response of dry snow is relatively constant throughout the year. However, σ^0 does vary spatially. For example, differences in accumulation rates cause spatial variance in σ^0 on the Greenland ice sheet. In regions of low accumulation, σ^0 is relatively high while regions with high accumulation are characterized by lower σ^0. Low accumulation exposes the surface snow grains for longer periods which results in larger grains. Additionally, wind scouring of the previous summer surface may contribute to higher backscatter in areas of low accumulation [4]. These spatial differences led Long and Drinkwater [4] to separate the dry snow zone into two regions.

Seasonal variations in σ^0 that appear to be independent of accumulation have also been discovered in the dry snow zone. These seasonal variations are described in Chapter 3 and discussed in the succeeding chapters.

2.3.5 Long and Drinkwater Map of the Ice Facies

A map of the Greenland ice sheet facies developed by Long and Drinkwater [4] is shown in Fig. 2.4. This map was developed using three months of data obtained in 1978 from the Seasat-A scatterometer (SASS).

The primary difference between Figs. 2.2 and 2.4 is the extent of the dry snow zone. The dry snow zone is much larger in Fig. 2.4 than in Fig. 2.2. There are several possible explanations for this. First, the Benson map was derived from comparatively sparse field data. Thus it is likely that the Benson map is not entirely accurate. Second, the Long and Drinkwater map is derived from only a few months of data that cover part of the melt and refreeze seasons. Thus the dry snow extent mapped in Fig. 2.4 may be inaccurate. Finally, it is likely that the extent of the facies varies from year to year depending on weather patterns. This variability makes it difficult to obtain truth data for validating facies mapping algorithms.

2.3.6 Accumulation Map

Since accumulation affects backscatter, knowledge of accumulation rates is important to the work of this thesis. The average and standard deviation of the accumulation rate on the Greenland ice sheet for the period 1958-2007 from [25] are given in Fig. 2.5. These accumulation rates are derived using output from the Fifth Generation Mesoscale Model modified for polar climates (Polar MM5) calibrated with firn core and meteorological station data [25]. Figure 2.5 shows that accumulation is generally higher in the southern regions of the Greenland ice sheet than the northern region. This is consistent with [4] where the southern region of the dry snow zone (high accumulation) is characterized by low σ^0 while the northern region of the dry snow zone (low accumulation) is characterized by high σ^0. Figure 2.5 also shows that the standard deviation of accumulation rate is lowest in the interior of the ice sheet which is where the dry snow zone is located.

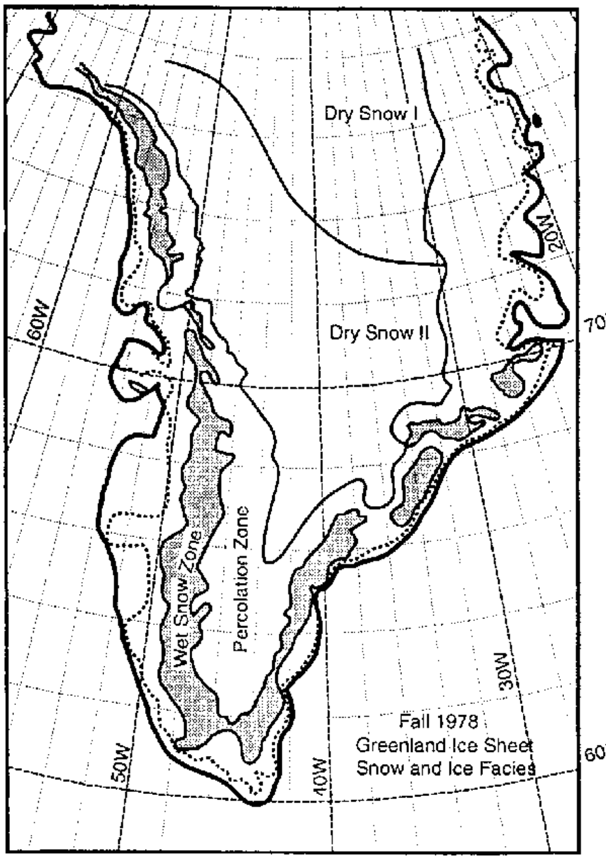

Figure 2.4: Long and Drinkwater [4] map of the Greenland ice facies using SASS data.

2.4 Scatterometer Data Sets

Data from multiple scatterometers are used in this thesis. A brief description of these scatterometers is given in the following.

2.4.1 QuikSCAT

The data and images studied in this thesis are primarily from QuikSCAT. QuikSCAT is a 13.4 GHz scanning pencil beam scatterometer with both an inner and outer beam. The inner beam is horizontally polarized with a fixed incidence angle of 46° while the outer beam is vertically polarized with an incidence angle of 54°. Each beam has a wide range of azimuth angles. The scanning geometry of QuikSCAT is given in Fig. 2.6.

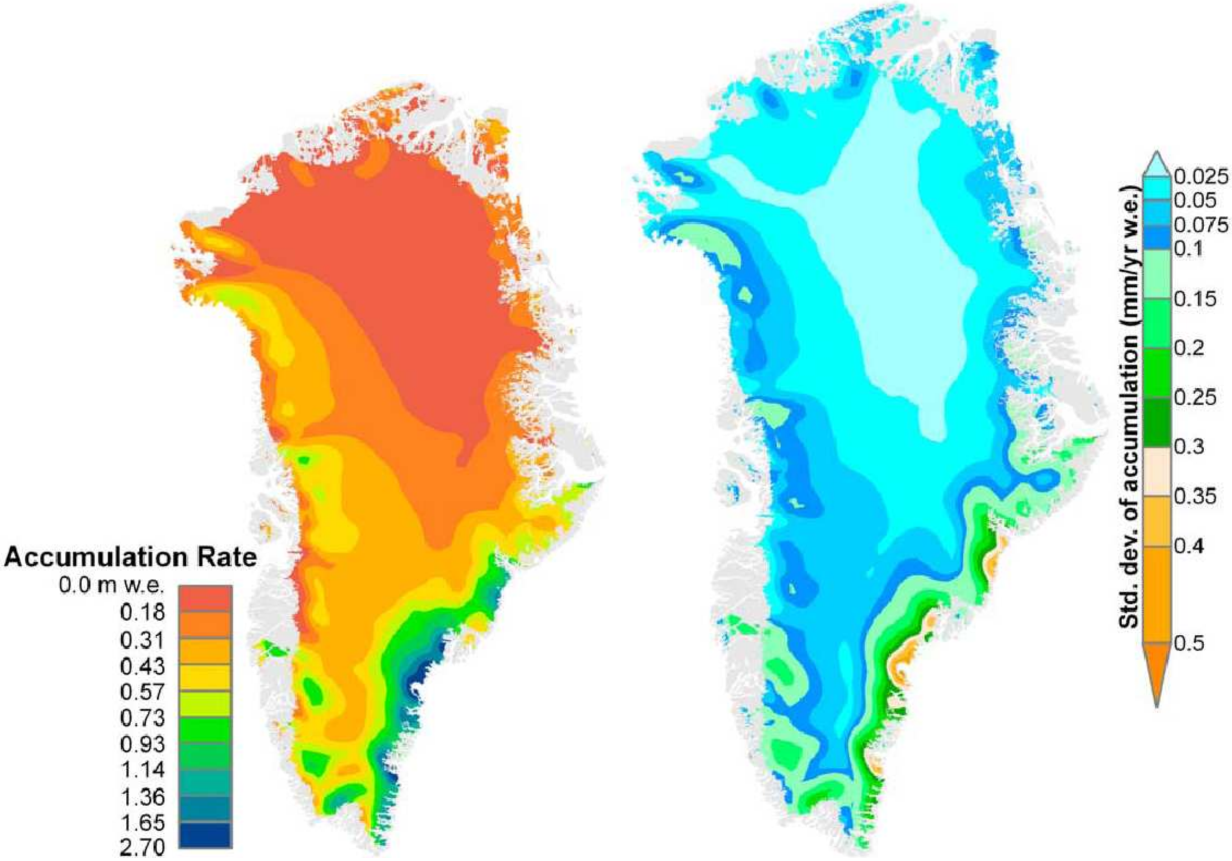

Figure 2.5: Information about accumulation on the Greenland ice sheet. W.e. stands for wet equivalent. Left: Average accumulation rate for the period 1958-2007 [25]. Right: Standard deviation of accumulation rate for the period 1958-2007 [25].

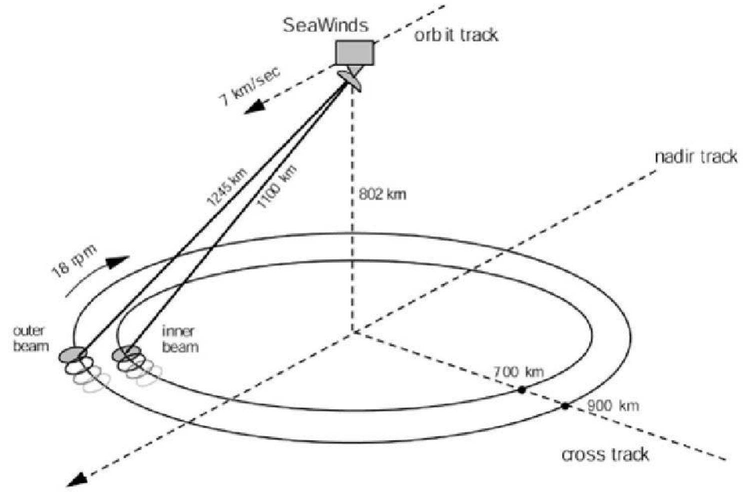

Figure 2.6: QuikSCAT scanning geometry [26].

QuikSCAT operated from July 1999 to November 2009, providing over ten years of data. Due to QuikSCAT's orbital pattern, QuikSCAT completes several passes per day in the Arctic and Antarctic regions making it ideal for studying these regions.

QuikSCAT has two different resolutions termed "eggs" and "slices". The egg resolution is the size of the antenna footprint on the ground which is approximately 25 km by 35 km. Through range and Doppler processing, each egg is divided into 12 slices which have an approximate resolution of 25 km by 6 km [27]. In this thesis, only the vertically polarized egg resolution σ^0 measurement of QuikSCAT is used. This facilitates easier comparison and application of the results of this thesis to other scatterometers that have similar resolution and polarization such as the Advanced Scatterometer (ASCAT).

2.4.2 Other Scatterometers

Although QuikSCAT [28] is the principle scatterometer used in this thesis, data and results from other scatterometers are considered in Chapter 4. These scatterometers include SASS [29], the European remote sensing satellite (ERS-2) [30], and ASCAT [31]. SASS operated in the Ku-band while ERS-2 and ASCAT operated in the C-band.

2.5 Image Reconstruction

Scatterometers have a relatively low spatial resolution that is not adequate for many applications. However, since scatterometers may pass an area multiple times per day, they can achieve dense spatial sampling at the expense of temporal resolution. The Scatterometer Image Reconstruction (SIR) algorithm is an iterative reconstruction method that uses this dense spatial sampling from multiple passes to achieve finer spatial resolution [32], [33].

When multiple measurements of incidence angle are available, the SIR algorithm assumes the following relationship between σ^0 and θ:

$$\sigma^0(\theta) = \mathcal{A} + \mathcal{B}(\theta - \theta_{ref}) \tag{2.2}$$

where θ_{ref} is a reference incidence angle (typically 40°) and $\mathcal{A}$ and $\mathcal{B}$ are constants that depend on the properties of the area in the pixel. The constant $\mathcal{A}$ gives the average σ^0

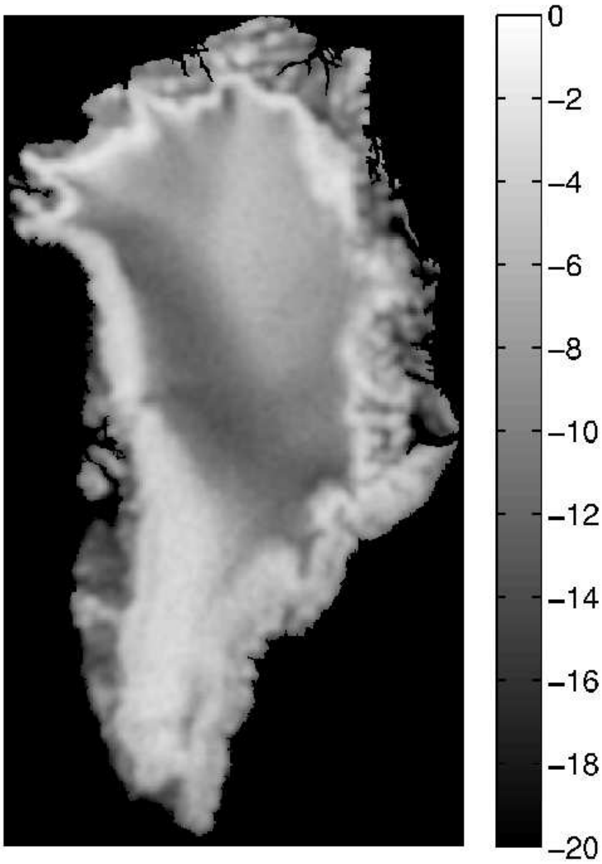

Figure 2.7: QuikSCAT $\mathcal{A}$ image in dB over Greenland on January 5, 2000. Ocean pixels are set to black.

during the imaging time at θ_{ref} while $\mathcal{B}$ gives the incidence angle dependence. Images of multiple regions of the earth are created using the values of $\mathcal{A}$ and $\mathcal{B}$.

For scatterometers such as QuikSCAT where the observation angle is fixed, only $\mathcal{A}$ images are created for the available polarizations. Thus only $\mathcal{A}$ images are used in this thesis. For QuikSCAT, egg images have a 4.45 km pixel resolution while slice images have a 2.225 km resolution. An example of a QuikSCAT $\mathcal{A}$ image is given in Fig. 2.7. In this image, some of the facies appear to be distinguishable such as the dry snow zone (the darker region in the center) and the percolation and wet snow zones (the brighter regions).

Several factors affect the accuracy of the SIR algorithm. First, the SIR algorithm assumes that σ^0 is constant during the imaging time. This assumption is not valid for all regions. For example, near-surface ocean winds can change rapidly during the day. The winds affect the geometry of the ocean surface which affects σ^0. Because of this variation during the imaging time, SIR images are not particularly useful over the ocean. Additionally, σ^0 can depend on the azimuth angle in certain regions [34], [35]. Since the SIR algorithm uses data from multiple passes, measurements are taken with multiple azimuth angles which can distort the measured σ^0 in these regions. However, σ^0 is relatively constant during the imaging time in many land and ice areas of the Earth. The high spatial and temporal resolution of SIR images have made them useful for studying these regions.

2.6 Automatic Weather Stations

To compare backscatter results with physical parameters such as temperature and wind speed, *in situ* data are obtained from Automatic Weather Stations (AWS) sponsored by the Greenland Climate Network (GC-Net) [36].

The AWS are distributed throughout the ice sheet and obtain hourly measurements of air temperature, wind speed, air pressure, and other parameters. Each station is equipped with multiple instruments for measuring air temperature. Fig. 2.8 shows a topographical map of Greenland with the location of many of the AWS.

Table 2.1 gives the number, name, and location of each AWS with data that overlap the duration of the QuikSCAT mission. Future tables that reference the AWS use only the station number.

2.7 Summary

Backscatter from scatterometers can be used to create radar images of remote locations such as the Greenland ice sheet. Using the electromagnetic properties of ice and snow, information about the ice facies can be inferred from analysis of these images. *In situ* data from AWS can be used to better understand conditions at the surface of the ice sheet that may affect backscatter.

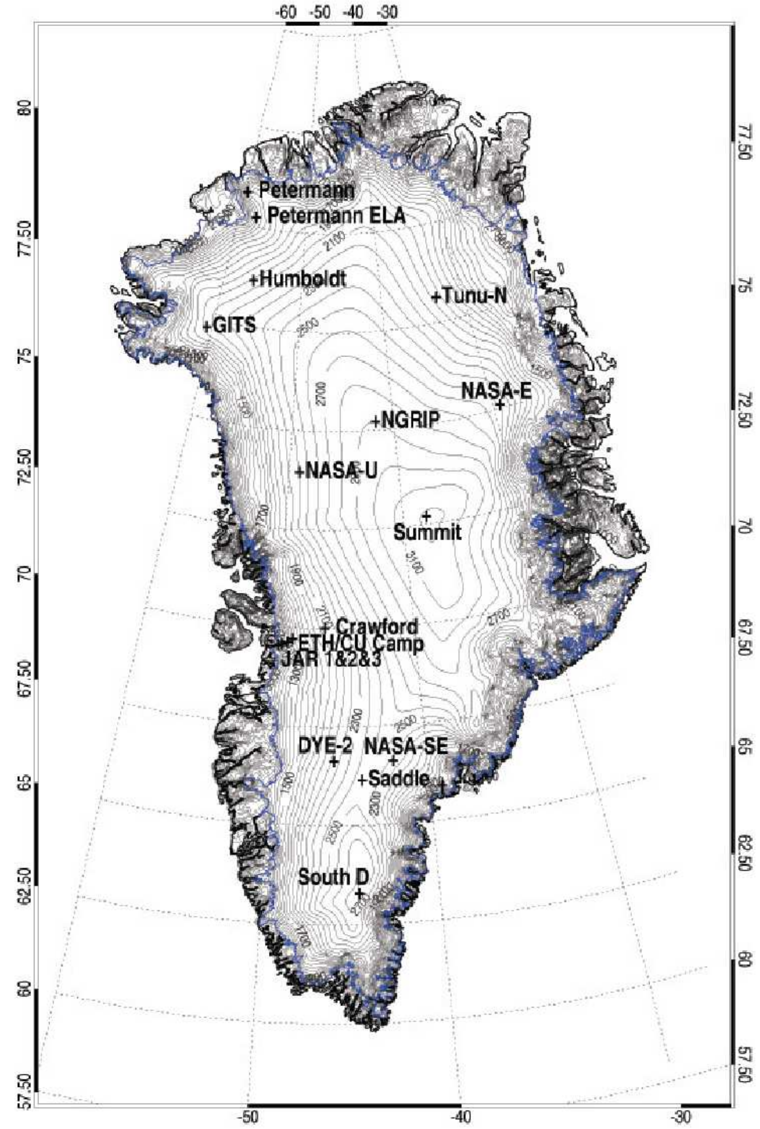

Figure 2.8: Topographical map of Greenland showing the location of the AWS on the Greenland ice sheet [36]. The blue line around the edge denotes the ice extent. Table 2.1 gives the name and number of all stations with data overlapping the QuikSCAT mission.

Table 2.1: The number, name, and location of each AWS. Adapted from [36]. Fig. 2.8 shows the location of some of these stations on a map of Greenland.

Station	Station Name	Latitude	Longitude	Altitude (m)
1	Swiss Camp	69°33′35”N	49°19′51”W	1176
2	Crawford Point1	69°52′42”N	46°59′48”W	2022
3	NASA-U	73°50′29”N	49°30′25”W	2334
4	GITS	77°08′16”N	61°02′24”W	1869
5	Humboldt	78°31′36”N	56°49′50”W	1995
6	Summit	72°34′46”N	38°30′19”W	3199
7	Tunu-N	78°00′59”N	33°59′00”W	2052
8	DYE-2	66°28′50”N	33°16′59”W	2099
9	JAR 1	69°29′42”N	49°42′14”W	932
10	Saddle	65°59′59”N	44°30′06”W	2467
11	South Dome	63°08′56”N	44°49′02”W	2901
12	NASA-E	75°00′02”N	29°59′50”W	2614
13	Crawford Point2	69°54′48”N	46°51′17”W	1990
14	NGRIP	75°05′58”N	42°19′59”W	2941
15	NASA-SE	66°28′30”N	42°29′55”W	2373
16	KAR	69°41′58”N	33°00′21”W	2579
17	JAR 2	69°24′53”N	50°05′34”W	507
19	JAR3	69°23′40”N	50°18′36”W	283
21	Peterman Gl.	80°41′01”N	60°17′32”W	37
23	NEEM	77°30′08”N	50°52′28”W	2454

Chapter 3

General Observations

This chapter gives some general observations of the Greenland ice sheet based on QuikSCAT data. First SIR images of Greenland are shown and discussed followed by a description of the method used to map the dry snow zone. Then the temporal behavior of σ^0 in the dry snow zone is analyzed using the KL expansion. All scatterometer data in this chapter comes from QuikSCAT.

3.1 SIR Images of the Greenland Ice Sheet

As mentioned in Sec. 2.2, the presence of liquid water is the primary parameter that affects σ^0 in snow. Thus the backscatter of the Greenland ice sheet changes as the melt and refreeze seasons begin and end. This section provides a general idea of the temporal behavior of backscatter throughout the ice sheet by displaying and discussing a time series of SIR images of Greenland focusing on the melt and refreeze seasons in a typical year.

Figure 3.1 displays such a time series of Greenland in the year 2000. In this year, σ^0 remains relatively constant at each pixel location until approximately JD 163. By this day, a decrease in σ^0 in the southern region of the ice sheet is visible. This decrease likely corresponds to melt. Some time later, melting has begun in the northeastern and northwestern edges of the ice sheet and has moved further inland in the south. This is visible in the image corresponding to JD 180 as lower backscatter in these regions. After this, severe melting occurs in the south over the next month or so as identified by the very low backscatter visible in JD 198 and JD 215. Some refreezing occurs soon after this as evidenced by the increased backscatter in JD 232. Refreezing is nearly completed, but is then interrupted by another melt event in the southwestern region. However, this melt event is much shorter than the

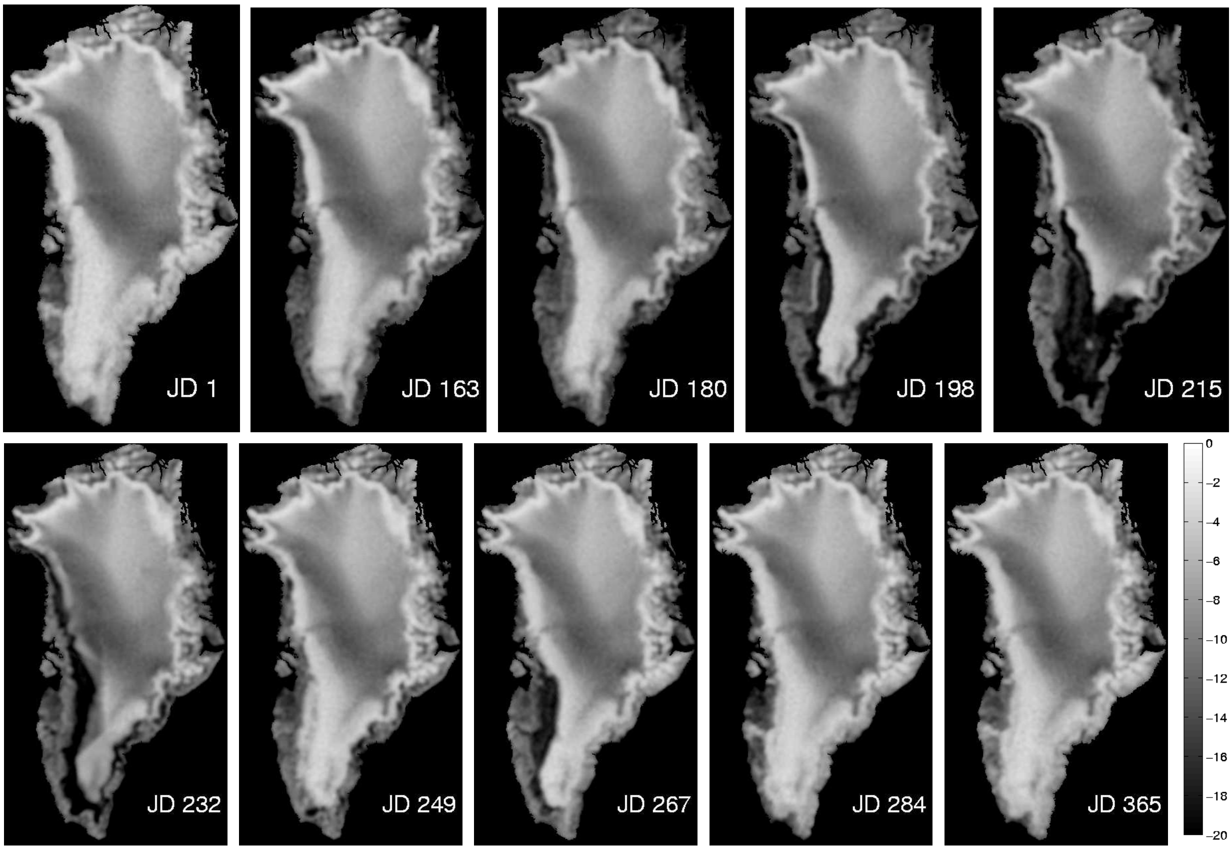

Figure 3.1: Time series of QuikSCAT SIR images of the Greenland ice sheet in 2000 emphasizing the changes in σ^0 during the melt and refreeze seasons.

previous events and the refreeze season is completed soon after (see the image corresponding to JD 284).

The analysis of Fig. 3.1 demonstrates how melting trends and other key features of the ice sheet can be identified using SIR images. Changes in σ^0 during the year can be used to classify and study the ice facies of the Greenland ice sheet. In succeeding sections, the Q-alpha method, which is based on changes in σ^0, is used to map melting and thus identify the dry snow zone.

3.2 Mapping the Dry Snow Zone

Because the dry snow zone is defined as the region where negligible melt occurs throughout the year, it can be mapped by using a melt detection algorithm. What does not

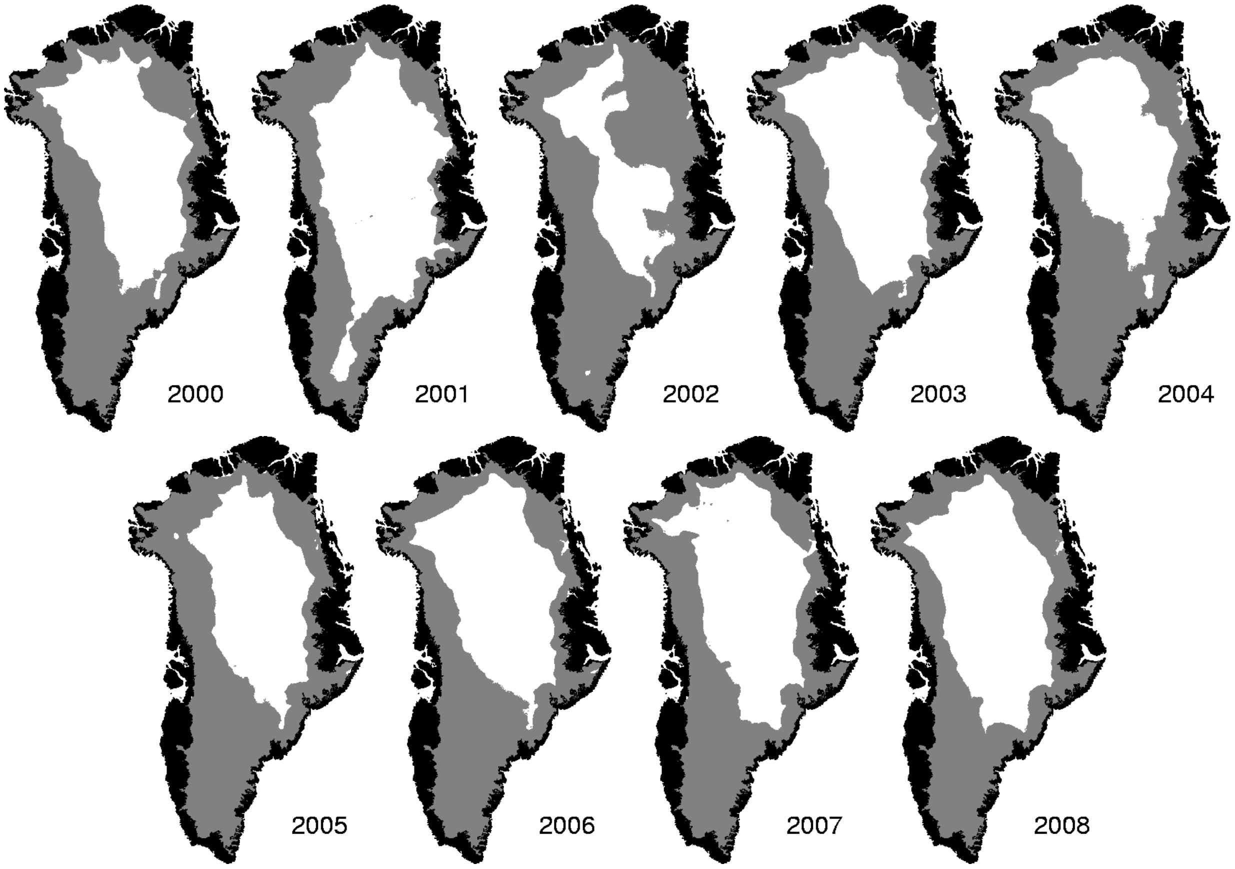

Figure 3.2: Maps of the dry snow zone on the Greenland ice sheet using QuikSCAT SIR images and the Q-α melt detection method. Dry snow and the ocean are white. Ice that is not dry snow is gray and bare land is black.

melt is, by definition, the dry snow zone. Therefore, in this thesis, pixels are classified as dry snow if no melt is detected for the entire year.

The melt detection algorithm used for dry snow classification in this thesis is the Q-α method [13]. The first step in this method is to calculate the winter backscatter mean at each pixel. This is done by averaging σ^0 over the first 60 days of the current year and the last 30 days of the previous year for each pixel. A pixel is classified as melting on a given day if σ^0 drops below the melt threshold on that day. The melt threshold for each pixel is then 3 dB below the winter mean. Further details about the Q-α method are given in Sec. 2.2.1. A pixel is classified as dry snow if it is not classified as melting throughout the entire year.

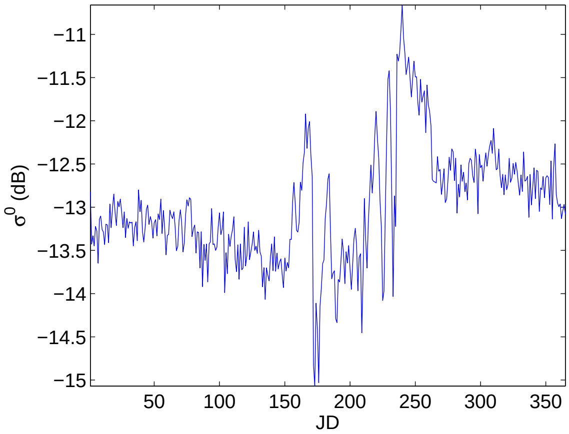

Figure 3.3: Backscatter over time at 47.4214° W and 73.1722° N in 2004 from QuikSCAT SIR images. Altitude at this point is 494 m.

3.2.1 Intra-annual Consistency

Figure 3.2 shows a map of the dry snow zone using QuikSCAT and the Q-α method for the years 2000-2008. The maps show that this method of dry snow classification has intra-annual spatial consistency. Most of the pixels classified as dry snow are next to each other in regions with higher latitude and altitude. The exceptions are typically located near the edge of the ice sheet (for examples see the northeast corners of the ice sheet in the years 2004 and 2006). The altitude at these regions is close to sea level (see Fig. 2.8) which suggests that these pixels should instead be classified as part of the ablation zone. These regions are not likely to be dry snow since they are generally separated from the main region of dry snow. Furthermore, plotting σ^0 over time at a point within one of these spuriously classified regions shows that σ^0 is somewhat erratic during the melt season (see Fig. 3.3). This behavior is more consistent with the ablation zone than the dry snow zone (see Sec. 2.3.1). Thus it is likely that these regions have been misclassified.

To mitigate ablation zone misclassification, altitude thresholding is used. The dry snow zone is typically located in higher altitudes while the ablation zone is in the lowest altitudes. Selecting a threshold in altitude should help differentiate between the two zones.

The altitude threshold is chosen with the aid of a histogram of the altitude of pixels classified as dry snow. The histogram is computed from a year where some pixels are

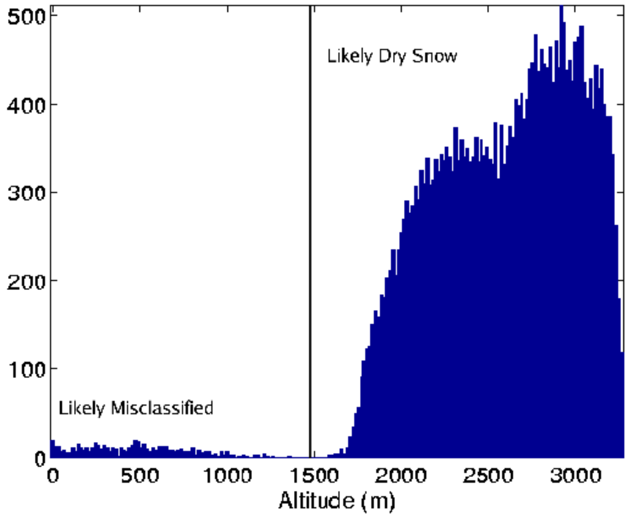

Figure 3.4: Histogram of altitude for pixels classified as dry snow in 2004 using the Q-α melt detection method (see text). The vertical line is the selected altitude threshold.

misclassified, and where the remaining dry snow pixels are consistent with other years. For these reasons, I chose the year 2004.

Figure 3.4 gives a histogram of the altitude of all pixels initially classified as dry snow in this year. Note that in the altitude range of 1380–1580 m, no pixel is classified as dry snow. I therefore chose the middle of this range (1480 m) as the threshold. As demonstrated in Fig. 3.5, the threshold succeeds at limiting the dry snow classification to the interior of the ice sheet.

3.2.2 Interannual Consistency

The maps in Figs. 3.2 and 3.5 demonstrate that there is significant interannual variation in the dry snow extent. In particular, the dry snow zone in the year 2002 is considerably smaller than in other years. This is due to an unusual melt event associated with a weather event. The high pressure ridge in this event brought unusually warm air onto the ice sheet raising the upper limit of the melt extent [15]. Excluding this year, a general dry snow region is visible although the edges may fluctuate from year to year. The interannual consistency of the dry snow classification demonstrates that the classification method is useful for classifying dry snow. Additionally, the interannual variability demonstrates that the classification method is sensitive to changes in the ice sheet.

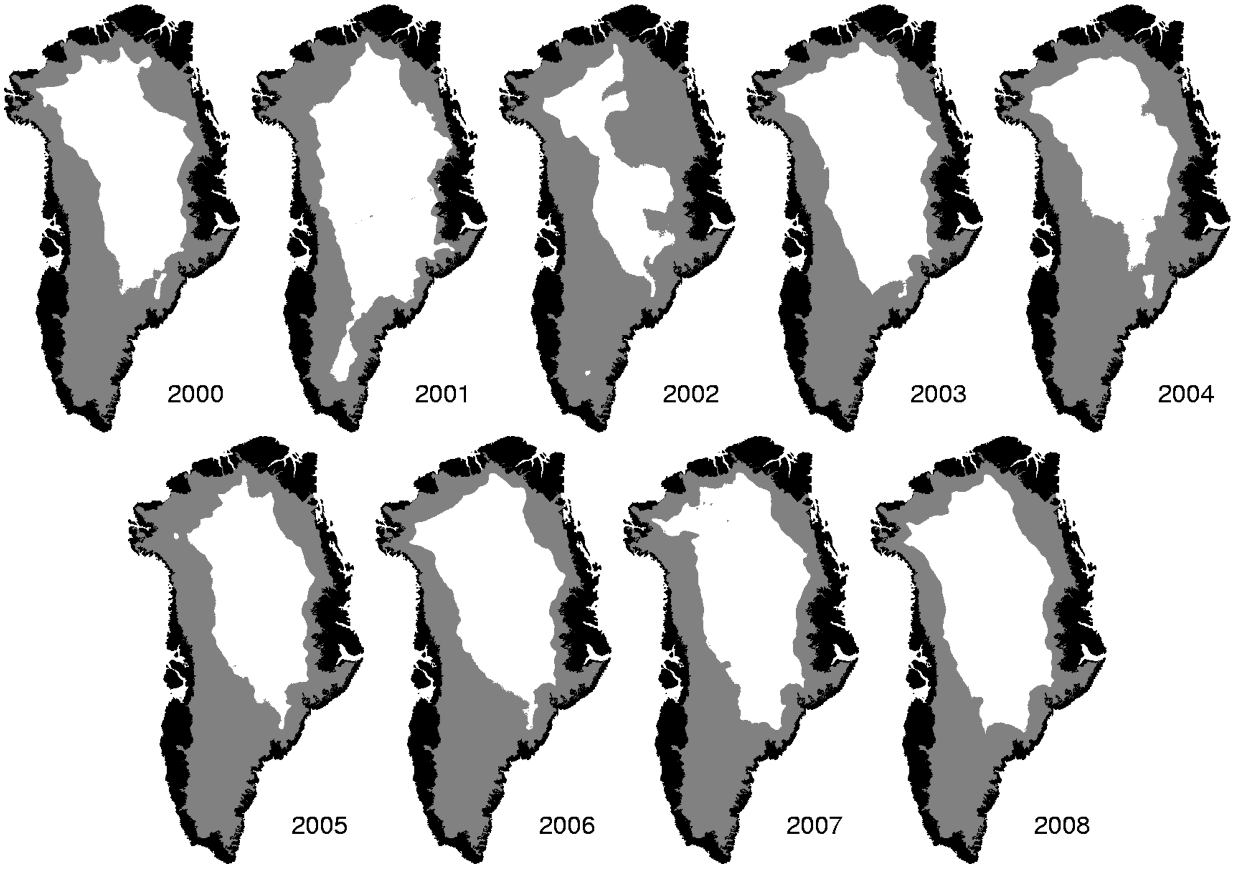

Figure 3.5: Maps of the dry snow zone on the Greenland ice sheet using the Q-α melt detection method and an altitude threshold of 1480 m. Dry snow and the ocean are white. Ice that is not dry snow is gray and bare land is black.

Table 3.1: Number of 4.45 × 4.45 km pixels classified as dry snow each year using the method in Fig. 3.5. The total number of pixels of the ice sheet is 84547.

Year	2000	2001	2002	2003	2004	2005	2006	2007	2008
# of Pixels	37438	46405	21401	42447	31580	33300	38080	39407	42184

Table 3.1 gives the number of pixels classified as dry snow each year after altitude thresholding. Note that in some years, the dry snow zone occupies slightly more than half of the entire ice sheet.

3.3 Analysis of Temporal Behavior of Dry Snow Zone Backscatter

Understanding the temporal behavior of dry snow aids in understanding climate as well as the transitions of dry snow to percolation zone and vice versa. This behavior can be analyzed by using the KL transform.

The KL transform represents a signal as a linear combination of an orthogonal basis derived from properties of the signal. The basis vectors generated by the KL transform are the eigenvectors of the correlation matrix of the signal. Since the KL expansion generates the basis that minimizes the mean-squared-error [37], the basis vectors represent the dominant patterns in the backscatter behavior.

3.3.1 Preliminary Work

In this application, some preliminary work must be performed before using the KL transform on the available data in the dry snow zone. A data matrix with zero mean in both dimensions is formed in the following. Let the random vector $\mathbf{x}$ represent the σ^0 of an entire year in the dry snow zone of the Greenland ice sheet. Then $\mathbf{x}$ has length m equal to the number of days of available data in the given year, and $\mathbf{x}_i$ is the observation of $\mathbf{x}$ at the i^{th} pixel in the dry snow zone. The data matrix X is then formed as

$$X = \begin{pmatrix} \mathbf{x}_1 & \mathbf{x}_2 & \dots & \mathbf{x}_N \end{pmatrix}^T \tag{3.1}$$

where $(\cdot)^T$ is the transpose operator, and N is the number of pixels classified as dry snow within the given year. The matrix X is an $N \times m$ matrix where the value at the i^{th} row and k^{th} column is the backscatter for the i^{th} pixel on the k^{th} day of the year. In this application, the ordering of the pixels does not matter.

Within the dry snow zone, annual σ^0 varies spatially according to factors such as multi-year snow accumulation and past melt events [4]. For example, the average annual backscatter for QuikSCAT of a pixel in the northeastern parts of the dry snow zone can achieve -5 dB compared to -14 dB in some of the central regions. In this study, we are primarily concerned with the temporal behavior of σ^0 in the dry snow zone and not the relative difference in average σ^0 from pixel to pixel. Therefore, I eliminate this difference by calculating the mean of each row in X to create an $N \times 1$ vector $\bar{\mathbf{x}}$. This is equivalent to forming a vector of the temporal mean of each pixel. The vector $\bar{\mathbf{x}}$ is then subtracted from each column of X. This can be represented as

$$Y = X - \begin{pmatrix} \bar{\mathbf{x}} & \bar{\mathbf{x}} & \dots & \bar{\mathbf{x}} \end{pmatrix}. \tag{3.2}$$

The mean of each row of the resulting matrix Y is zero.

The KL expansion of a vector requires that each element of the random vector be zero mean [37]. This means that to use the data in the transform, each column of Y must be zero mean. Subtracting the transpose of the vector mean $\bar{\mathbf{y}}$ from each row in Y accomplishes this. $\bar{\mathbf{y}}$ is estimated by calculating the sample vector mean using each row of Y as a sample vector. This is equivalent to forming a row vector from the mean of each column of Y. This provides a $1 \times m$ row vector which is equal to the transpose of the sample vector mean.

In this case, $\bar{\mathbf{y}}$ is the spatial average of σ^0 in the dry snow zone. The spatial average of σ^0 contains more information about the temporal behavior of σ^0 in the dry snow zone than the basis vectors generated by the KL transform. Thus it is important to include the spatial average in the analysis of σ^0.

To finish the preliminary work, the transpose of $\bar{\mathbf{y}}$ is subtracted from each row in Y to yield a data matrix Z with each column and row having zero mean. This can be represented as

$$Z^T = Y^T - \begin{pmatrix} \bar{\mathbf{y}} & \bar{\mathbf{y}} & \dots & \bar{\mathbf{y}} \end{pmatrix}. \tag{3.3}$$

Since the corresponding random vector $\mathbf{z}$ is zero-mean, the KL transform of the random vector $\mathbf{z}$ can be performed using the sample vectors $\mathbf{z}_i$ corresponding to the rows of Z.

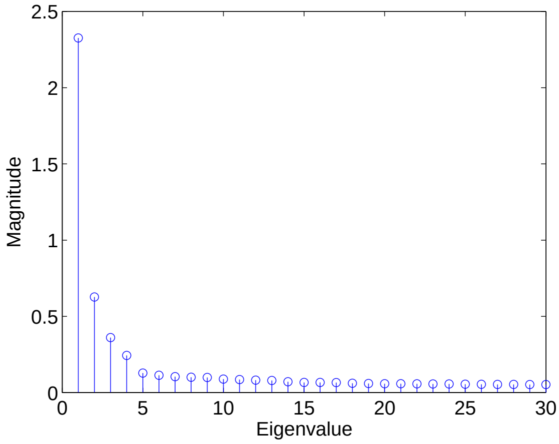

Figure 3.6: The magnitude of the 30 largest eigenvalues of S in the year 2000 using QuikSCAT data.

3.3.2 The KL Transform

The first step in the KL expansion is to compute the covariance matrix of $\mathbf{z}$. I use the sample covariance matrix S where

$$S = \frac{1}{N-1} \sum_{i=1}^{N} \mathbf{z}_i \mathbf{z}_i^T . \tag{3.4}$$

The matrix S is then factored into the form $S = U \Lambda U^T$ where Λ contains the eigenvalues of S and the columns of the matrix U are the eigenvectors of S. The eigenvectors form the set of basis vectors for the expansion [37].

To efficiently represent the temporal behavior of σ^0, a basis with a relatively low dimension while limiting loss in accuracy is desired. However, the basis formed from the full KL expansion has a dimension of m which is no better than using the original signal. Instead, a lower dimensional basis with a fixed dimension n that minimizes the mean squared error is desired. The basis that fits this criteria is the set of eigenvectors of S that correspond to the n maximum eigenvalues in magnitude [37].

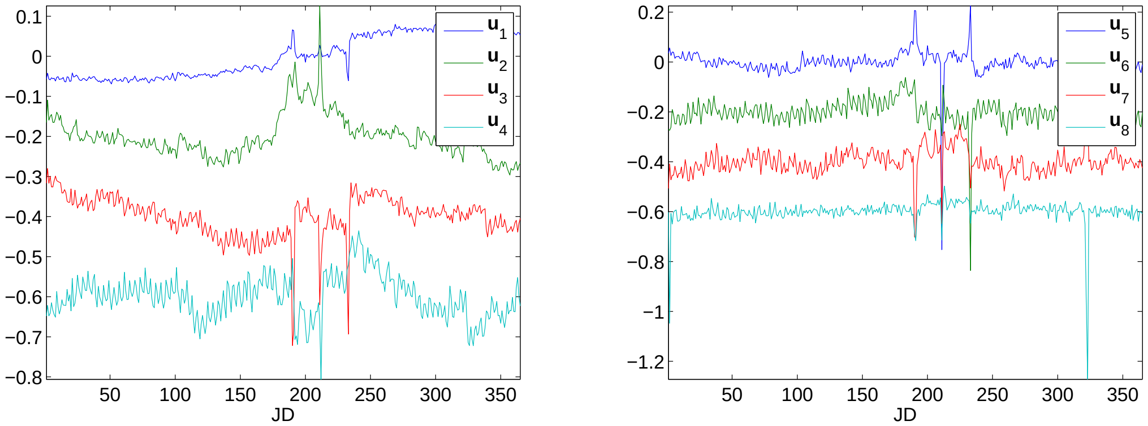

Figure 3.7: The eigenvectors ($\mathbf{u}_i$) of S where $\mathbf{u}_i$ corresponds to the i^{th} largest eigenvalue of S in the year 2000. The y-axis is in dB and each vector is zero-mean. For easier comparison, the lines are shifted vertically by 0, −0.2, −0.4, and −0.6, respectively, in each plot.

3.3.3 Results

Figure 3.6 shows the largest eigenvalues of S using data from the year 2000 while Fig. 3.7 shows the eigenvectors corresponding to the 8 largest eigenvalues of S. The magnitude of the eigenvalues rolls off quickly which indicates that relatively few eigenvectors can be used as the basis with limited loss in accuracy.

Choosing n

Since the eigenvalues quickly decrease in magnitude, only the first eight eigenvectors are shown here. The first eigenvector (labeled $\mathbf{u}_1$) demonstrates a general linear trend which accounts for any difference in backscatter between the beginning and end of the year. The second eigenvector ($\mathbf{u}_2$) is relatively constant throughout the year except during the summer months which are characterized by an increase in σ^0 (or decrease depending on the sign).

The third eigenvector ($\mathbf{u}_3$) displays several instances of a “reset” behavior, generally following a precipitous drop in σ^0. This is consistent with the behavior observed in some regions near the edge of the dry snow zone. The fourth eigenvector ($\mathbf{u}_4$) also appears to be associated with some of the reset events displayed in $\mathbf{u}_3$. It may also compensate for some of the error caused by the other eigenvectors.

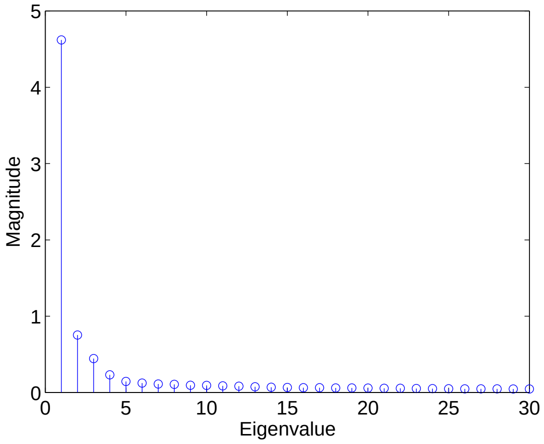

Figure 3.8: The magnitude of the 30 largest eigenvalues of S using QuikSCAT data from the years 2000 to 2008. Most of the information in the process is contained in the largest few eigenvalues.

The fifth through eighth eigenvectors ($\mathbf{u}_5$ to $\mathbf{u}_8$) are mostly distinguished by the location of spikes in σ^0 in time. These spikes likely correspond to warm weather episodes causing an increase in liquid water towards the edges of the dry snow zone. All years show this behavior, though the time of the spikes appears to vary from year to year.

Since we are primarily interested in the general trends of σ^0, $n \leq 4$ can be chosen in this case. This is consistent with Fig. 3.6 which shows that most of the information is contained within the first few eigenvectors.

Although the basis set chosen from a given year minimizes the mean squared error for that year, it is not guaranteed to minimize the error for other years. To compare results from all years, the KL transform is performed on a data matrix formed from data from 2000 to 2008 to obtain a basis set that minimizes the overall error. To mitigate the effects of the spikes on the eigenvectors, I drop the days affected by the spikes and interpolate to fill the gaps. This is performed on each pixel prior to forming the data matrix X.

Figure 3.8 shows that most of the information is contained in the first few eigenvectors in this case as well. Comparing the eigenvectors in Fig. 3.9 to the eigenvectors generated using individual years demonstrates that a version of $\mathbf{u}_1$ is present in all years. Additionally, similar versions of $\mathbf{u}_2$ and $\mathbf{u}_3$ are present in multiple years while a version of $\mathbf{u}_4$ is present in a few years. The remaining eigenvectors appear to mainly compensate for small irregularities

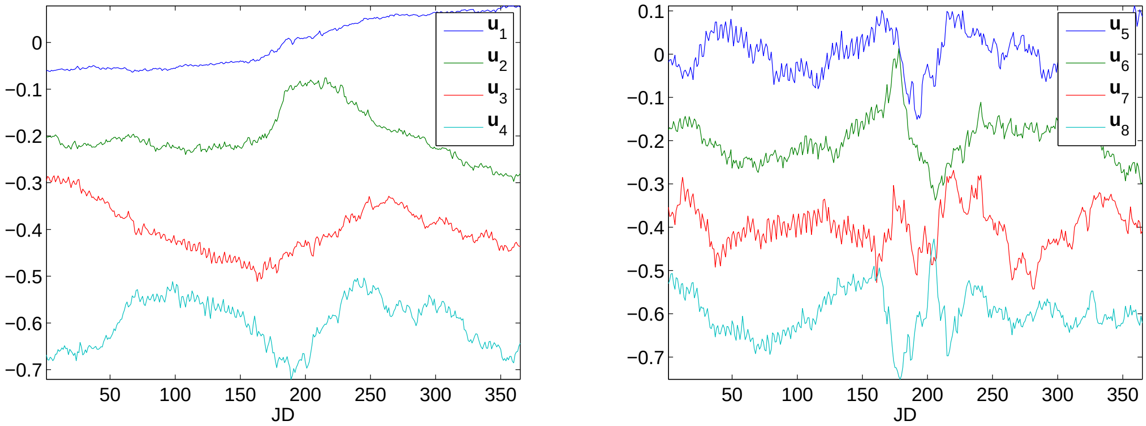

Figure 3.9: The eigenvectors ($\mathbf{u}_i$) of S where $\mathbf{u}_i$ corresponds to the i^{th} largest eigenvalue of S from 2000 to 2008. The y-axis is in dB and each vector is zero-mean. For easier comparison, the lines are shifted vertically by 0, -0.2, -0.4, and -0.6, respectively, in each plot.

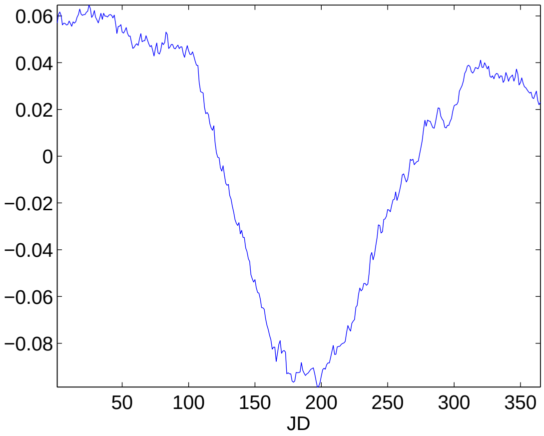

Figure 3.10: Normalized average of the data from 2000 to 2008. This is the estimate of $\bar{\mathbf{y}}$ where the data matrix Y includes data from 2000 to 2008 . This average vector is denoted as $\mathbf{r}$ in Eq. (3.5).

from year to year. Combining this information with Fig. 3.8, I choose $n = 4$ for the analysis.

Least-Squares Estimation

To better understand the temporal behavior of σ^0 in dry snow, the coefficients of the average (see Fig. 3.10) and the first four eigenvectors are estimated for each pixel for each

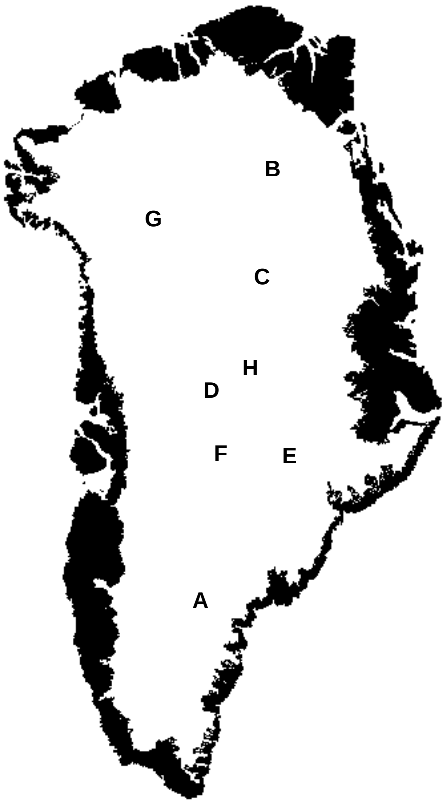

Figure 3.11: Map of Greenland showing the location of regions discussed in this section.

year. In other words, the coefficients for the following equation are estimated using the least squares method for each year:

$$\sigma^{\mathbf{0}}{}_i = a + b_1\mathbf{r} + b_2\mathbf{u}_1 + b_3\mathbf{u}_2 + b_4\mathbf{u}_3 + b_5\mathbf{u}_4 + \mathbf{n}_i \tag{3.5}$$

where the vector $\sigma^{\mathbf{0}}{}_i$ contains the values of σ^0 for the entire year at the i^{th} pixel, a is the average backscatter for the year, $\mathbf{n}_i$ is noise, and $\mathbf{r}$ is the normalized average of all the data from 2000 to 2008 as shown in Fig. 3.10. Figure 3.11 shows the location of regions discussed in the following while Figs. 3.12–3.17 show images of the estimated coefficients from 2000 to 2008.

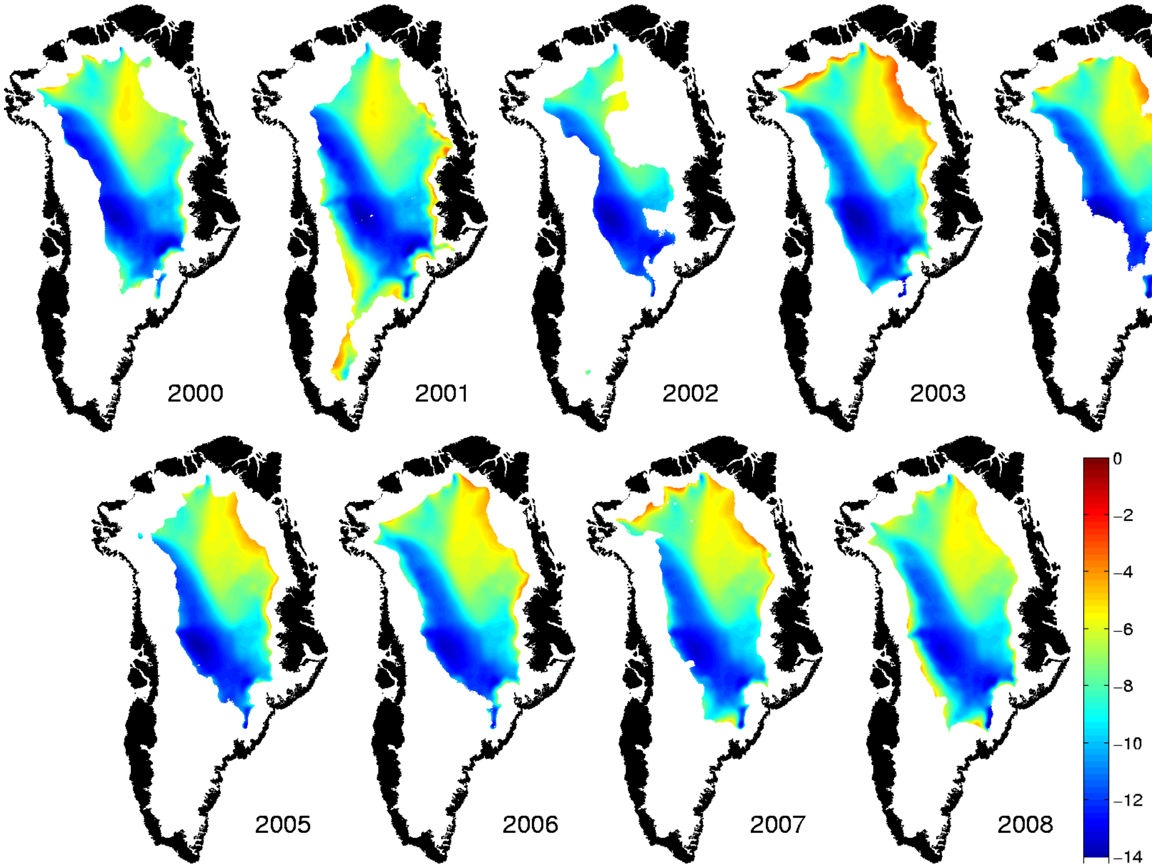

Figure 3.12: Estimated values for a from Eq. (3.5).

Discussion

The long-term location of the dry snow zone can be deduced from Fig. 3.12. Long-term dry snow excludes regions that are only occasionally classified as dry snow using melt detection algorithms. An example of such a region is found in the southern part of the Greenland ice sheet in 2001 (labeled A in Fig. 3.11). This region typically melts each year and is classified as either wet snow or part of the percolation zone. However, in 2001 it did not melt. The buried ice lenses and layers from past melt maintain a high average backscatter in this region (typically greater than -7 dB). Similar small regions can be found in the northern part of the ice sheet. Since accumulation is lower in the northern part of the dry snow zone, backscatter is generally higher. Thus the average backscatter for the occasional dry snow regions is generally greater than -5 dB. An example of this region is visible in the northeastern part of the ice sheet in 2003 (labeled B).

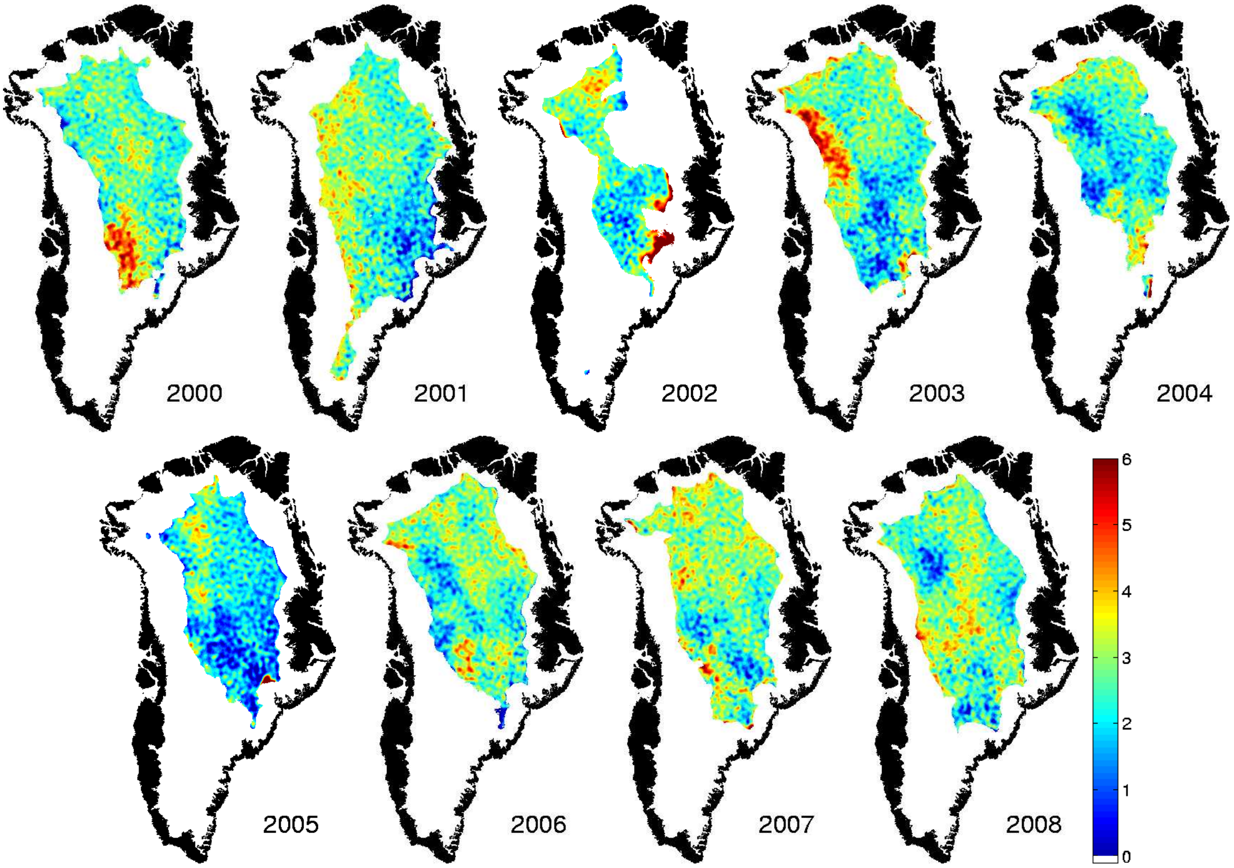

Figure 3.13: Estimated values for b_1 from Eq. (3.5).

Conversely, long-term dry snow includes regions that only occasionally exhibit melt. The average backscatter remains low compared to that of the percolation or wet snow zones in these regions despite the occasional melt event. An example of this is found in the northeastern part of the ice sheet in 2002 (labeled C).

Figure 3.12 shows that the average backscatter (a) in the dry snow zone stays relatively constant over time. However, since the eigenvector $\mathbf{u}_1$ has an increasing pattern, the values of b_2 may indicate changes in the average backscatter that may be difficult to see in Fig. 3.12.

An example of a region that appears to indicate changes in a is in the central part of Greenland at 43.3439° W and 72.0257° N (labeled D). Table 3.2 gives the values of b_2 at this position from 2000 to 2008. The difference between the first and last elements in $\mathbf{u}_1$ is about 0.14. If no other basis vectors are assumed to influence the average backscatter, then

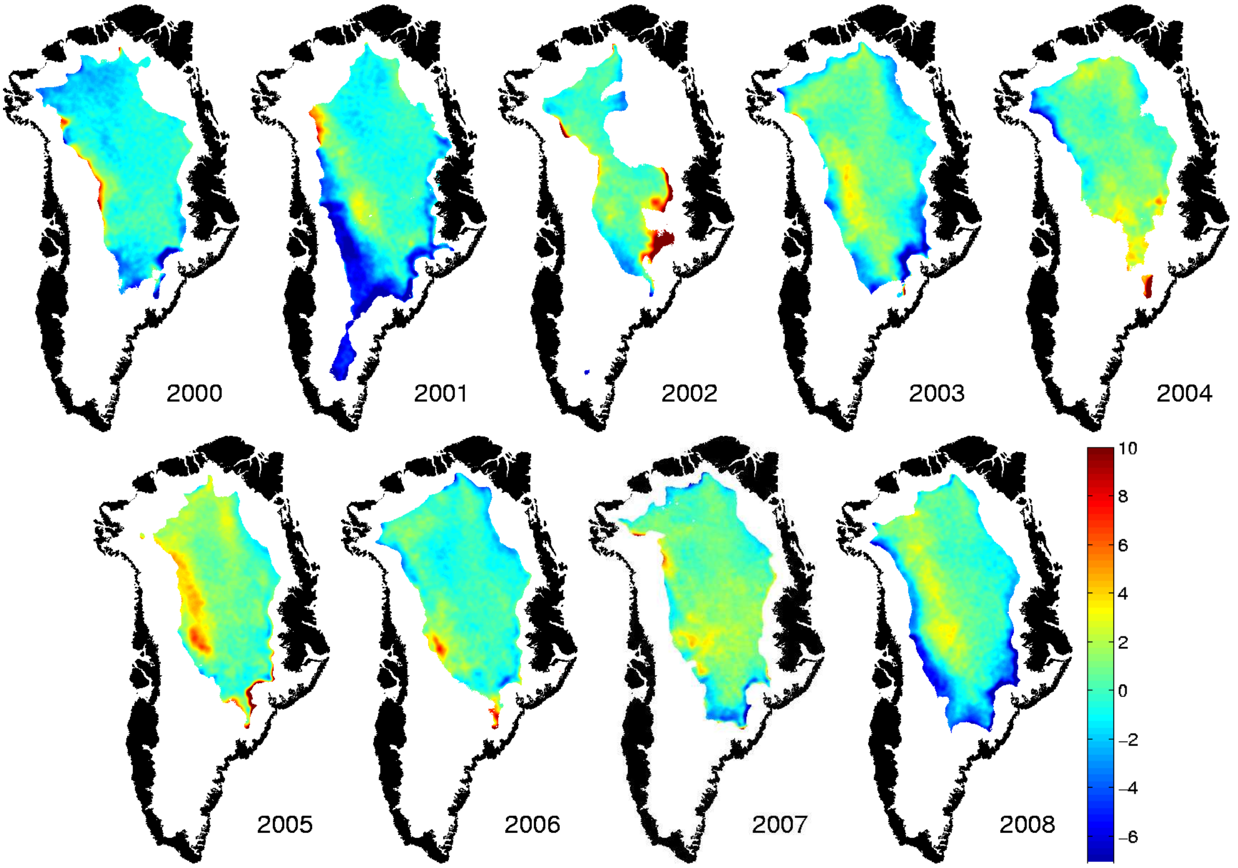

Figure 3.14: Estimated values for b_2 from Eq. (3.5).

the expected increase in a at this point from 2000 to 2008 based on the values in Table 3.2 is 2.9 dB. However, the actual increase in a at this point was only 0.55 dB. This suggests that the other vectors influence the value of the average backscatter. This is consistent with Figures 3.9 and 3.10 which show that the vectors $\mathbf{r}$, $\mathbf{u}_2$, and $\mathbf{u}_3$ all end with a slightly lower value. Based on the sign and magnitude of the corresponding coefficients, these vectors affect the average backscatter. Therefore, although the values of b_2 may indicate small changes in average backscatter, the coefficients of other vectors should be considered when looking for changes in a over time. An example of this is given in Fig. 3.18 on page 37 which shows the backscatter at 43.3439° W and 72.0257° N in 2002. At this point, $b_2 = 0.8$. However, the backscatter ends the year at a slightly lower level despite the positive value of b_2.

Information can still be gleaned from regions with high positive values of b_2. Towards the edges of the dry snow zone, a "reset" behavior sometimes occurs in σ^0. This reset is

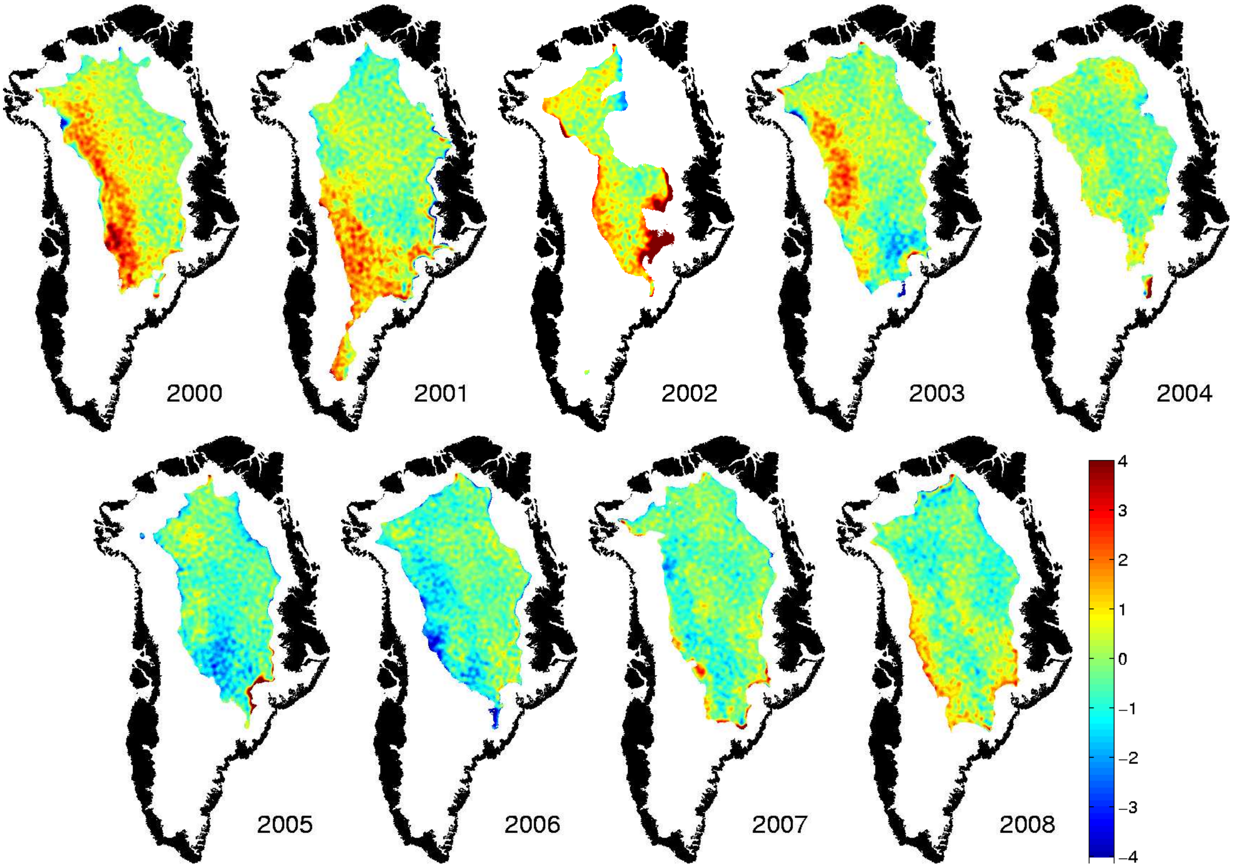

Figure 3.15: Estimated values for b_3 from Eq. (3.5).

Table 3.2: Values of b_2 at 43.3439° W and 72.0257° N. This point is labeled D in Fig. 3.11.

Year	2000	2001	2002	2003	2004	2005	2006	2007	2008
b_2	-0.7	3.3	0.8	2.2	2.2	5.7	1.7	3.1	2.7

characterized by a sudden increase in σ^0 in late summer or fall. The backscatter then remains at approximately the same level for the remainder of the year. The reset is typically preceded by a decrease in σ^0 that does not exceed the melt threshold. A clear example of this reset behavior is given in Fig. 3.19 on page 38. This figure is in 2002 in the southeastern region of the dry snow zone where the values of b_2 are large (labeled E in Fig. 3.11). Note that the model of Eq. (3.5) reconstructs the reset behavior reasonably well.

The reset behavior seen in Fig. 3.19 is commonly present in the percolation zone. The reset in the percolation zone is caused by refreezing percolated water into ice lenses

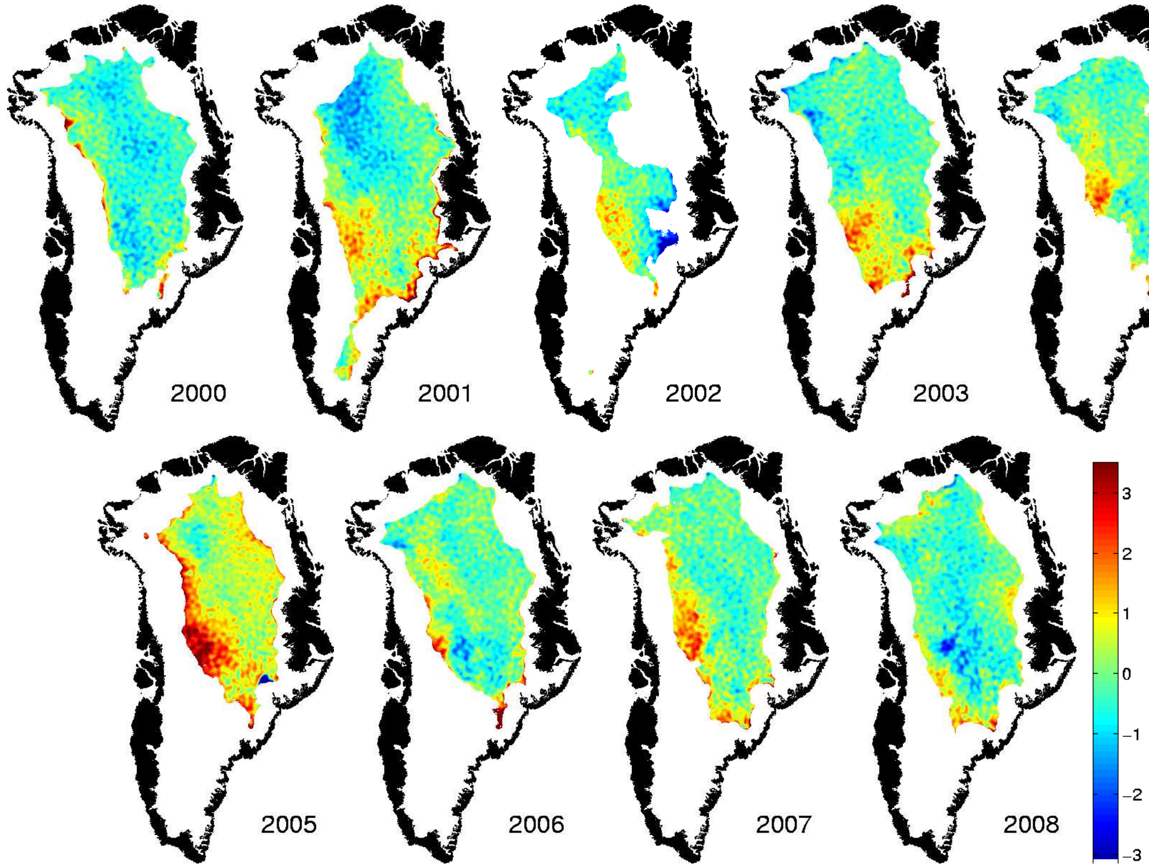

Figure 3.16: Estimated values for b_4 from Eq. (3.5).

and other subsurface structures. These structures result in higher backscatter after refreeze than before melting. The presence of the reset behavior in pixels classified as dry snow suggests that these pixels are not truly dry snow. Further implications of the presence of reset behavior in pixels classified as dry snow are discussed in Chapter 5.

Although all of the vectors in Eq. (3.5) are required to accurately estimate σ^0, reset regions are generally associated with high values of b_2. Based on experimentation, typical values of b_2 associated with reset behavior are $b_2 > 7$ although resets can be found where b_2 is as low as 4 in some cases.

Figure 3.14 shows that negative values of b_2 are typically located around the edges of the dry snow zone. Examination of Fig. 3.14 shows that negative values of b_2 are typically preceded by a few years of melting or positive values of b_2. Melt in previous seasons likely resulted in subsurface ice structures which result in an increase in σ^0. However, as snow

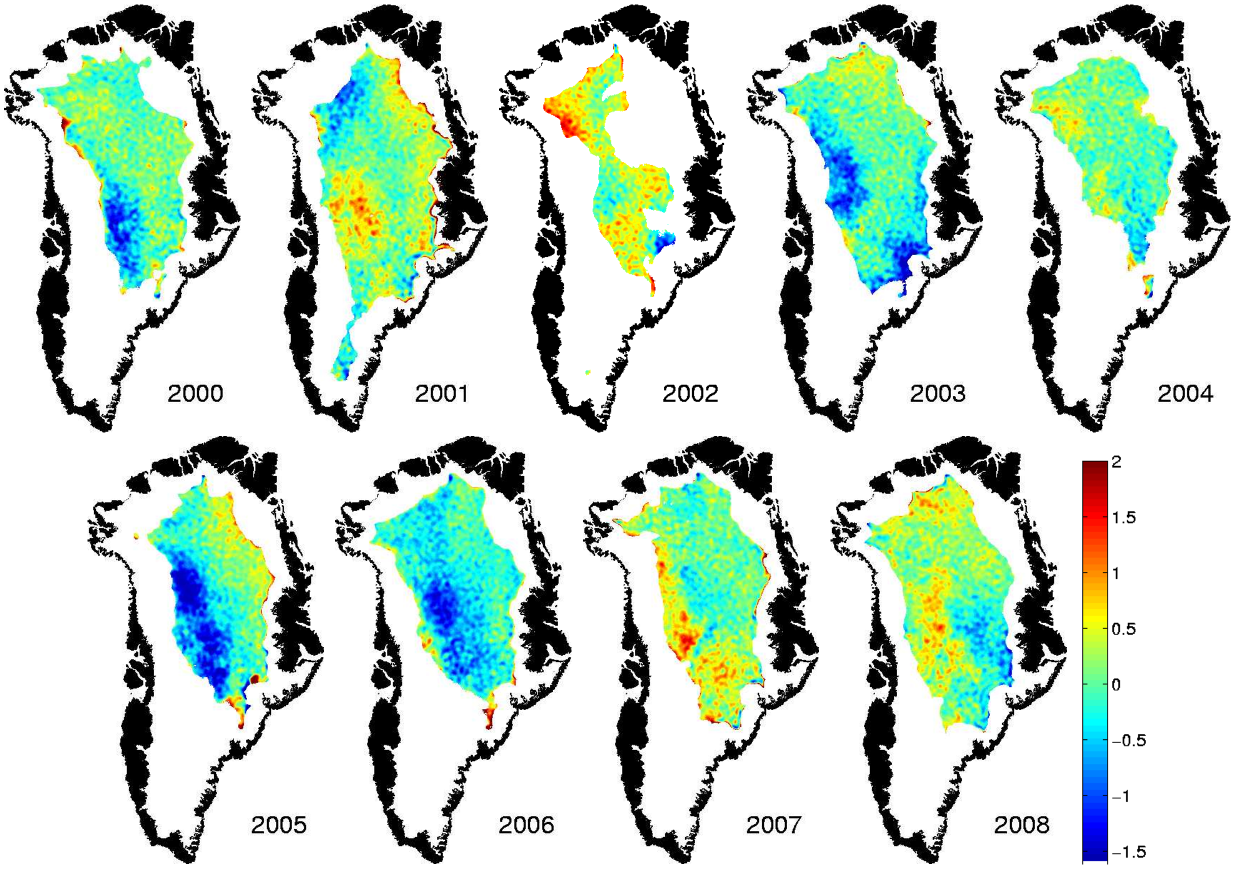

Figure 3.17: Estimated values for b_5 from Eq. (3.5).

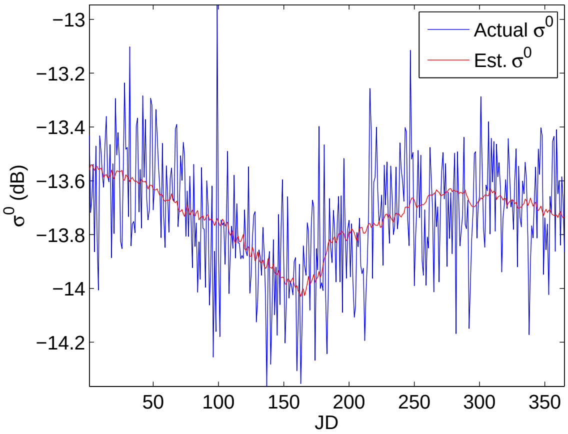

Figure 3.18: Estimated and actual backscatter at 43.3439° W and 72.0257° N in 2002. This point is labeled D in Fig. 3.11 and has an overall decrease in σ^0 despite a positive value of b_1.

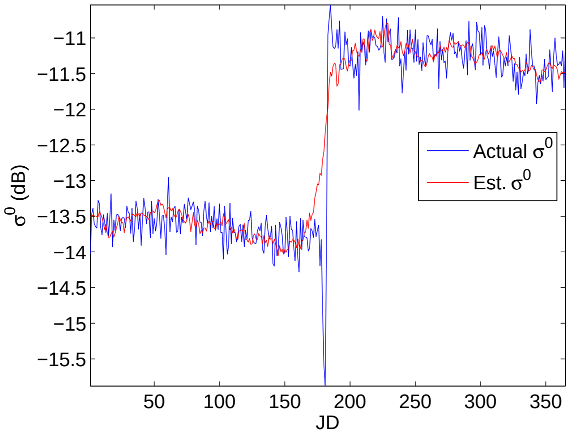

Figure 3.19: Actual σ^0 and estimated σ^0 at 34.2290° W and 69.9493° N in 2002. This point is labeled E in Fig. 3.11. The estimation is performed using the least squares fit of Eq. (3.5). The estimated values are $a = -12.4$, $b_1 = 9.1$, $b_2 = 22.6$, $b_3 = 14.0$, $b_4 = -2.9$, and $b_5 = -1.3$.

accumulates without melting in succeeding years, the subsurface structures are buried. This results in a decrease in backscatter which is indicated by a negative value of b_2.

The estimated values of b_1 are given in Fig. 3.13. This figure shows that b_1 is typically positive throughout the entire dry snow zone. This suggests that the general form of the vector $\mathbf{r}$ is present in σ^0 in the entire dry snow zone. Figure 3.10 shows that $\mathbf{r}$ is characterized by a decrease in backscatter during the summer months followed by a return to approximately the winter backscatter levels. Since this pattern of backscatter behavior appears to be seasonal, it is termed “seasonal variation”. An example of the seasonal variation in backscatter at a single location is contained in Fig. 3.18.

Since $\mathbf{r}$ is the spatial average of all the data in the dry snow zone from 2000 to 2008, the seasonal variation is the dominant pattern in backscatter behavior in the dry snow zone. This is reiterated in Fig. 3.20 which shows the spatial average of the dry snow zone for each year from 2000 to 2008. This figure shows that the spatial average displays the same general seasonal variation from year to year. While the depth of the decrease and the winter return level towards the end of the year may vary somewhat, the same general pattern of a decrease in σ^0 followed by an increase in σ^0 is present in each year. Thus seasonal variation is present in the dry snow zone in each year.

Since the seasonal variation is the dominating feature of backscatter in the dry snow zone, it is important to study the cause of seasonal variation for several reasons. First, it is important to know whether the cause of seasonal variation is instrumental or geophysical. Instrumental causes of seasonal variation in σ^0 could have important implications on the accuracy of scatterometer images. Second, if the cause is geophysical, understanding the cause could lead to better understanding and measurement of ice sheet conditions. Third, understanding the cause of seasonal variation could lead to a model that can predict the seasonal variation. Predicting the seasonal variation could then lead to improved scatterometer calibrations. For these reasons, Chapters 4 and 5 are dedicated to determining the cause of seasonal variation in the dry snow zone.

Several large regions of high b_1 values exist in 2000 (F), 2002 (E), and 2003 (G). In 2002, the high values of b_1 in the southeastern part of the dry snow zone are associated with a reset (see Fig. 3.19). However, this is not the case in 2000 and 2003. Figure 3.21 compares σ^0 for pixels with high (G) and low (H) values of b_1 in 2003. This figure shows that a high b_1 is simply associated with a larger decrease in σ^0. Similar results are found in 2000.

The coefficient b_1 is also used in succeeding chapters to quantify the magnitude of the seasonal variation. This is done by first finding the difference between the maximum and the minimum of the vector $\mathbf{r}$. This difference is 0.16 dB. The approximate magnitude of the seasonal variation at a given pixel is the estimated value of b_1 at the pixel multiplied by 0.16.

The coefficients of the remaining vectors ($\mathbf{u}_2$, $\mathbf{u}_3$, and $\mathbf{u}_4$) are more difficult to interpret. Based on observations of σ^0 in the dry snow zone, these vectors help to provide variations in seasonal variation. For example, negative coefficients for $\mathbf{u}_2$ combined with a positive b_1 could indicate a deeper and longer decrease in σ^0 during the summer months while positive coefficients could indicate a shorter decrease in σ^0. Similarly, the coefficients for both $\mathbf{u}_3$ and $\mathbf{u}_4$ are suggestive of spatial variations in the general seasonal variation. A full discussion of the coefficients of these vectors is beyond the scope of this thesis. However, the spatial consistency of the coefficients displayed in Figs. 3.15, 3.16, and 3.17 suggests that the vectors are related to some geophysical cause.

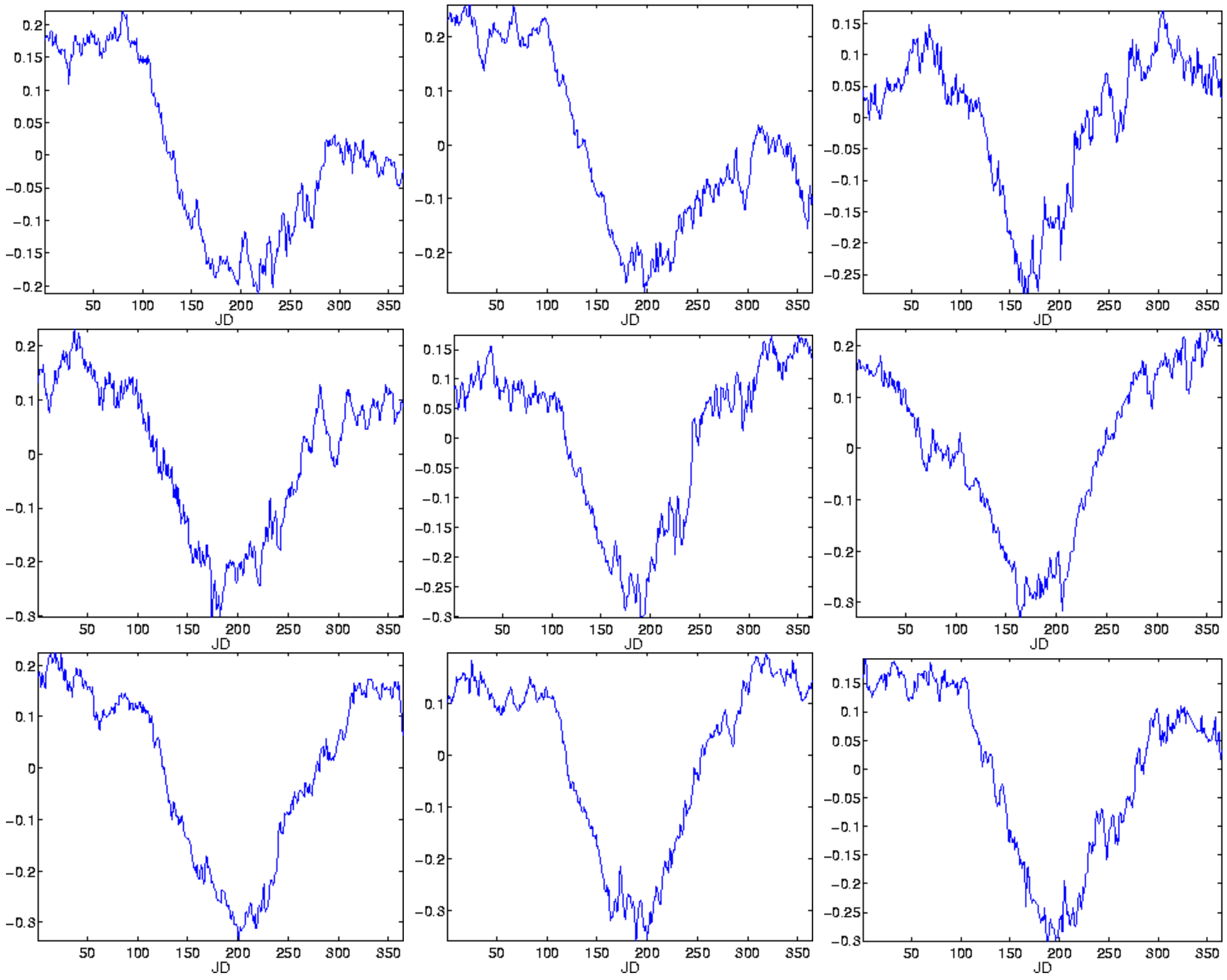

Figure 3.20: Spatial averages of backscatter in the dry snow zone. Top row from left to right: Spatial average for 2000, 2001, and 2002. Middle row from left to right: Spatial average for 2003, 2004, 2005. Bottom row from left to right: Spatial average for 2006, 2007, and 2008.

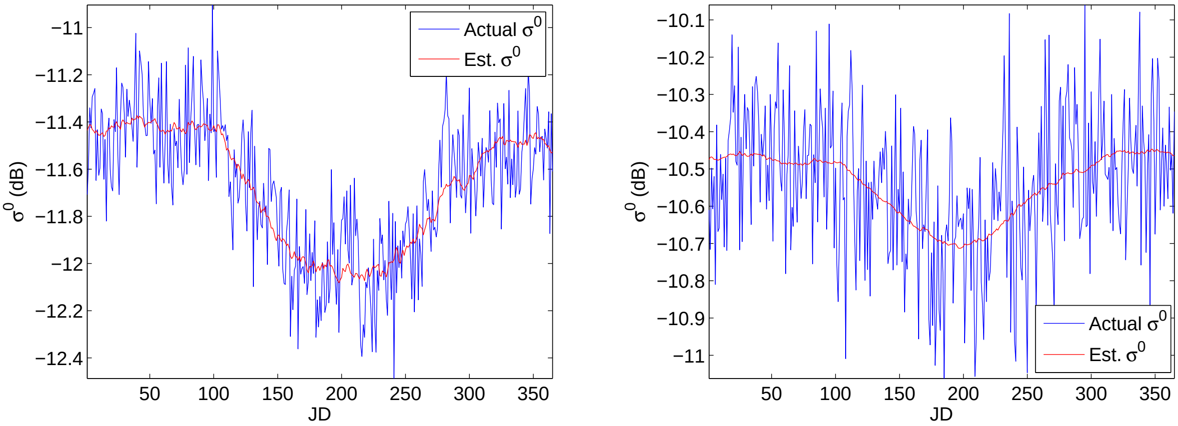

Figure 3.21: Estimated and actual backscatter at 54.6462° W and 77.0466° N (left, $b_1 = 5.7$, labeled G) and 38.2474° W and 72.7047° N (right, $b_1 = 1.4$, labeled H) in 2003.

3.4 Summary

QuikSCAT SIR images of the Greenland ice sheet are useful for identifying melting trends and other key features of the ice sheet. The images are used to identify the dry snow zone using the Q-α melt detection method and altitude thresholding. This method of dry snow zone identification displays interannual consistency as well as some variability that takes into account changes in the ice sheet.

The KL transform is used to identify and study the dominant patterns in annual backscatter behavior. Some of these patterns are used to detect specific behaviors in σ^0 such as the reset behavior seen in Fig. 3.19. Additionally, spatially averaging σ^0 shows that seasonal variation is the dominant pattern (see Figs. 3.10 and 3.20). The implications of seasonal variation warrant study of the causes of seasonal variation in the succeeding chapters.

Chapter 4

Investigation of Possible Instrumental Causes of Seasonal Variation

Possible causes of the observed seasonal variation in the backscatter of dry snow include instrumental effects. Instrumental causes of seasonal variation could have important implications on the accuracy of scatterometer images. This chapter identifies and tests several QuikSCAT instrumental parameters that may be related to the observed seasonal variation in backscatter.

Possible instrument-based causes of seasonal variation include incidence angle variation and orbital drift which can cause variation in imaging time and azimuth angle. Since σ^0 in snow depends on these parameters, the seasonal variation in σ^0 in the dry snow zone could be caused by seasonal variation in these parameters. Multiple points classified as dry snow within the Greenland ice sheet are tested. It is found that it is unlikely that instrumental parameters are causing the seasonal variation. Further evidence is then provided that suggests that the cause is geophysical and not instrumental. This evidence includes the spatial consistency of seasonal variation, the presence of seasonal variation in Antarctica, and the observation of similar seasonal backscatter characteristics in other scatterometers.

4.1 Incidence Angle Variation

Due to QuikSCAT's design, there is little variation in the incidence angle (θ). Nevertheless, the possible effects of seasonal variation in incidence angle are tested.

For each pixel in the SIR algorithm, multiple measurements are used to calculate σ^0. Each measurement may have a slightly different incidence angle. Thus there are multiple measurements of θ associated with each pixel. The reported pixel value is the average of these measurements. If the average θ varies with season, and $\frac{\partial \sigma^0}{\partial \theta}$ is sufficiently large, the changing average θ may cause an apparent change in σ^0. This is tested in the following.

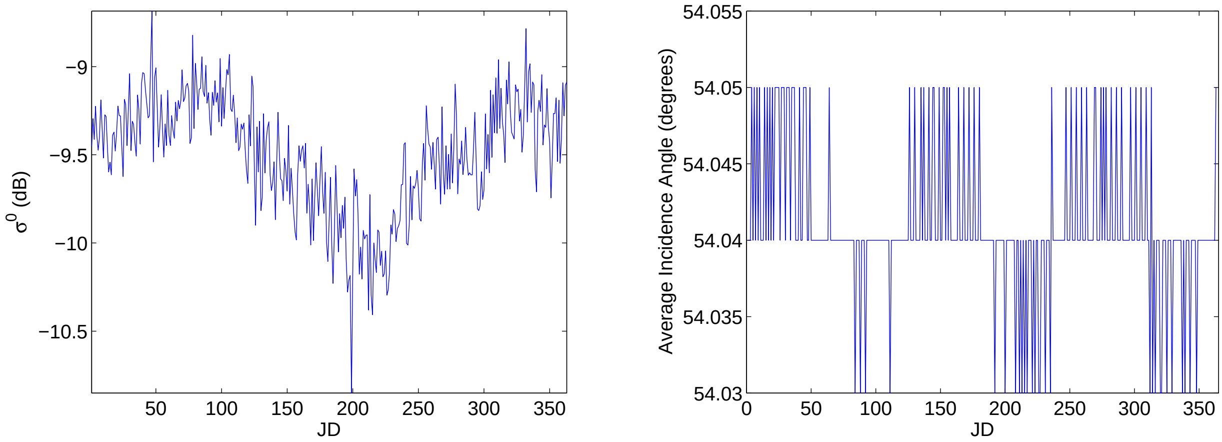

(a) Backscatter

(b) Average incidence angle

Figure 4.1: QuikSCAT (a) σ^0 and (b) average incidence angle (θ) in 2006 at 59.2229° W and 77.1670° N. Average incidence angle measurements are quantized to 0.01° in the source L1B file.

Figure 4.1 shows the average incidence angle at $-59.2229°$ longitude and $77.1670°$ latitude in 2006. For this time period, $\theta \in [54.03°, 54.05°]$ which is a very small range. Backscatter incidence angle dependence over ice can be up to 0.25 dB/deg for QuikSCAT [38]. This means that backscatter variation on the ice sheet due to incidence angle variation can only account for up to 0.005 dB at this point. At this point, $b_1 = 4.2$ which gives a value of 0.67 dB for the approximate magnitude of the seasonal variation. Comparing these values shows that incidence angle variation can only account for less than 1% of the seasonal variation in σ^0.

Furthermore, Fig. 4.1 shows that θ does not vary seasonally in the same general manner as σ^0. Thus I conclude that the seasonal variation in σ^0 is not caused by incidence angle variation. Studies of other points in the dry snow region yield similar results.

4.2 Orbital Drift

QuikSCAT was designed to have an orbital pattern with a four day repeat cycle during which it completes fifty-seven revolutions. This means that the position of the satellite was intended to be approximately the same every four days, or equivalently every fifty-seven

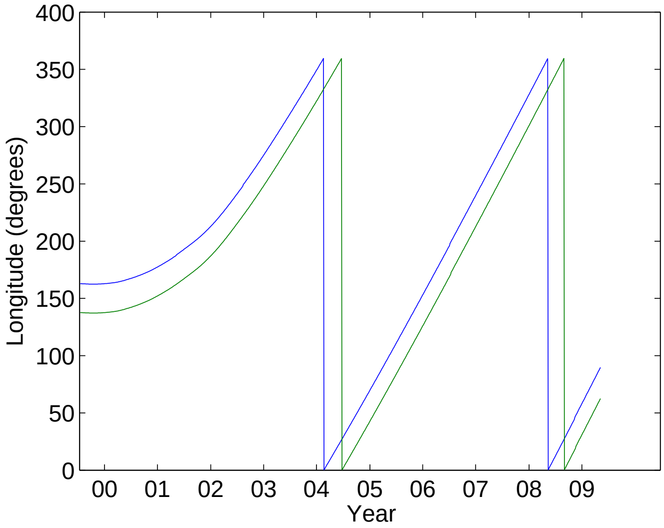

Figure 4.2: Longitude of the ascending node for the QuikSCAT satellite every 57 revolutions for two different passes beginning with revolutions 430 and 431. The discontinuities are caused by wrapping.

revolutions. This pattern was initially tightly controlled after QuikSCAT's launch in 1999. However, this control soon ceased and the orbit began to drift. The satellite drift pattern can be determined by plotting the longitude of the ascending node every fifty-seven revolutions over the duration of the mission. Figure 4.2 shows that the longitude of the ascending node varies little initially. However, the longitude begins to shift approximately at the beginning of 2000 and eventually achieves a rate of nearly 1° per 57 revolutions or equivalently 91° per year.

As the orbit shifts, the local time of day and the azimuth angle of the measurements used to create backscatter images also shift. Since σ^0 over snow can depend on the local time of day and azimuth angle, orbital drift may cause seasonal variation if the drift pattern matches with the seasonal variation. However, this is not the case. According to the QuikSCAT data files, the minimum difference in longitude between two separate passes is about 6.5°. These passes occur at approximately the same local time but for different days in the four day cycle. This means that at a drift rate of 91° per year, σ^0 should have a cycle of about 26 days instead of a full year if the drift is affecting σ^0. Since this is not observed it

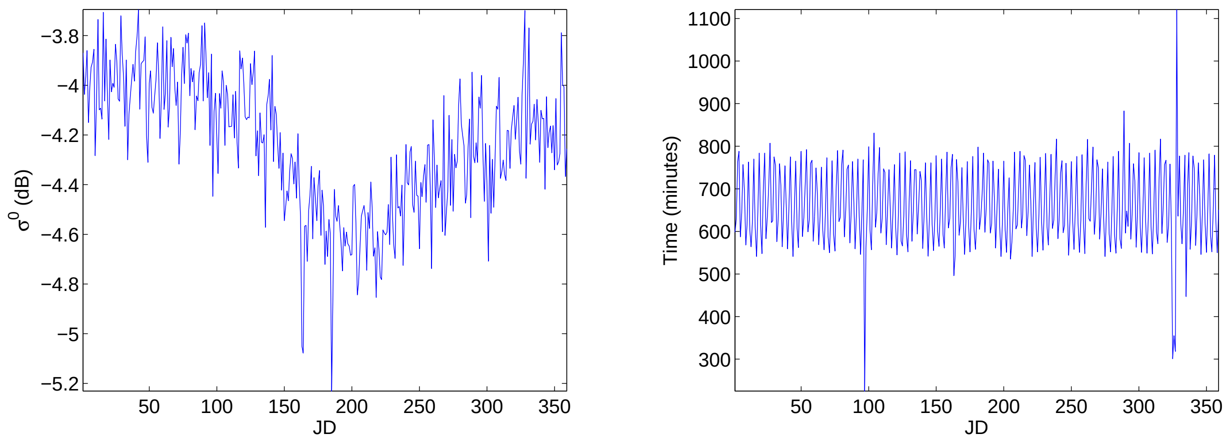

(a) Backscatter

(b) Average time (minutes after 12:00 AM local time) of all passes

Figure 4.3: QuikSCAT (a) σ^0 and (b) the average time for each day in 2007 at 28.7282° W and 77.5432° N.

is unlikely that the seasonal variation is caused by orbital drift. However, for confirmation, variations in the local time of day and in azimuth angle are examined in the following.

4.2.1 Local Time of Day Variation

In this section variations in the local time of day of the SIR images are investigated. SIR all-pass images are created using data from multiple passes. Since snow conditions vary throughout each day, especially if melt is involved, the local time of day of the passes can influence the backscatter results. Thus large variations in the image local time of day can cause variations in σ^0. The average local time of day is used for the same reasons that the average incidence angle is used in Sec. 4.1.

Figure 4.3 shows an example of backscatter dependence on the local time of day towards the end of the year. For most of the year, the average local time of day at this point is periodic with several cycles. One of these periods is approximately 26 days as expected. However, at JD 325 the temporal variance of the average time increases until about JD 333. This increase in the temporal variance of the average time corresponds to an increase in the temporal variance of σ^0 for this day range.

While this shows that variations in the average local time of day may be correlated with variation in σ^0, the seasonal variation in Fig. 4.3(a) does not correspond to any significant variation in the average local time of day (see Fig. 4.3(b)). In other words, the average local time of day does not vary seasonally. Thus I conclude that it is unlikely that the seasonal variation in σ^0 is caused by local time of day variation. Studies at other locations yield similar results.

4.2.2 Azimuth Angle Variation

Orbital drift can also affect the azimuth angle. Backscatter dependence on azimuth angle (azimuth modulation) is caused by different formations in the ice or snow. One type of snow formation that causes azimuth modulation of σ^0 in Antarctica is sastrugi [39, 40, 41]. Sastrugi are ridges of snow similar to sand dunes that are formed by wind and lie parallel to the wind direction. Sastrugi can range in size from a few to over a hundred meters [42]. Due to their shape, sastrugi can affect surface scattering depending on the azimuth angle.

Azimuth modulation of σ^0 is not as strong in Greenland as in Antarctica although it is also likely caused by sastrugi [43]. However, azimuth modulation may still be significant in the dry snow zone. Therefore, azimuth angle variation could contribute to seasonal variation in σ^0 in the dry snow zone. However, this is unlikely. Figure 4.4 shows a plot of QuikSCAT azimuth angle measurements over time at the Greenland summit in 2008. The figure shows that the azimuth angle measurements have a period of approximately 26 days which is consistent with the orbital drift period. However, this figure also shows that azimuth angle does not have a seasonal period that is consistent with the seasonal period observed in σ^0. Thus it is unlikely that azimuth angle variation is causing the seasonal variation in σ^0.

4.3 Other Parameters

In addition to incident angle, local time of day, and azimuth angle, other parameters of the satellite were examined including the number of pulses per telemetry frame; spacecraft position, velocity, and location; frequency shift; and calibration factors. None of these parameters demonstrate behavior correlated with the seasonal variation in σ^0 in the dry snow zone. Therefore, it is unlikely that the cause of seasonal variation is instrumental.

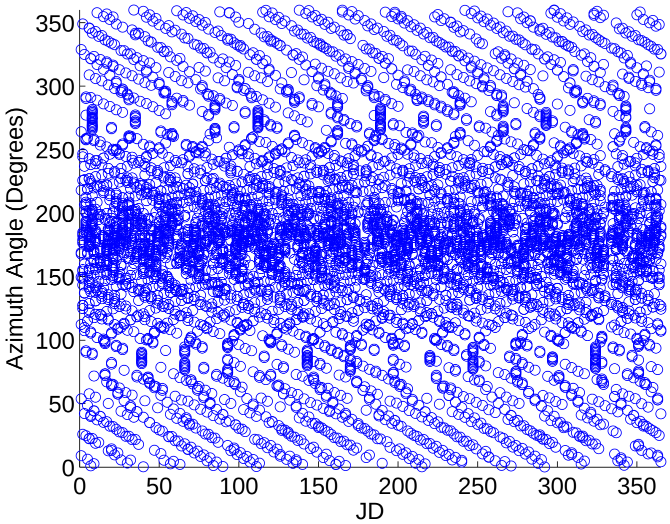

Figure 4.4: Scatter plot of the azimuth angle for each QuikSCAT measurement over time in 2008 at the Greenland summit. The azimuth angle has a period of about 26 days due to orbital drift. The 26 day period is most easily observed at higher and lower angles.

4.4 Evidence Against Instrumental Causes

This section provides further evidence that the cause of seasonal variation in σ^0 is not instrumental and is thus geophysical. The evidence includes the spatial consistency of seasonal variation, the presence of seasonal variation in Antarctica, and seasonal variation in σ^0 derived from other scatterometers.

4.4.1 Spatial Consistency of Seasonal Variation

If seasonal variation is caused by instrumental effects, the magnitude of seasonal variation in σ^0 in the dry snow zone would be either spatially uniform across the ice sheet or would be noise-like. However, the spatial distribution of seasonal variation suggests that the seasonal variation has a geophysical cause. Figure 3.13 gives a measure of the magnitude of the seasonal variation in the dry snow zone. This figure shows that the magnitude displays spatial consistency throughout the ice sheet. Additionally, the magnitude varies regionally. This distribution is consistent with a regionally varying geophysical cause. Therefore, since the distribution of the magnitude of the sesasonal variation is neither uniform nor noise-like, it is unlikely that the seasonal variation is caused by instrumental effects.

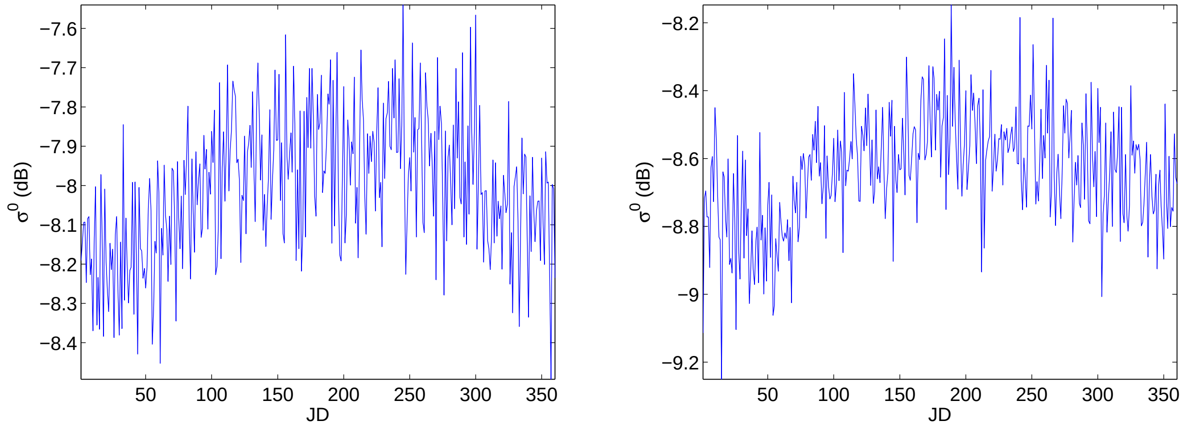

Figure 4.5: QuikSCAT σ^0 over time in 2008 in Antarctica at (left) 115.9889° E and 75.2389° S and (right) 124.1333° E and 74.6194° S.

4.4.2 Seasonal Variation in Antarctica

If instrumental effects cause the observed seasonal variation in σ^0, then the seasonal variation should be similar in other polar regions. To help determine whether seasonal variation can be observed elsewhere in the polar regions, several points in a region of Antarctica that is similar to the Greenland dry snow are investigated. This region experiences no melt, is high in altitude, and experiences low azimuth modulation.

Figure 4.5 shows σ^0 over time for two different points on the Antarctic ice sheet in 2008. A similar seasonal variation in σ^0 is visible except that the decrease in σ^0 occurs in the earlier months of the year which corresponds to the Antarctic summer. If the cause of seasonal variation is instrumental, the decrease in σ^0 would likely occur at the same time of year for both Greenland and Antarctica. Since it does not, this suggests that the cause of seasonal variation in σ^0 is instead geophysical.

4.4.3 Seasonal Variation in Other Scatterometers

To further test whether the seasonal variation in backscatter in the dry snow zone of Greenland is driven by instrumental effects, data from SIR images of Greenland from other scatterometers are compared to data from QuikSCAT SIR images. The orbit, geometry, and other instrumental parameters of ERS-2, SASS, and ASCAT are distinctly different

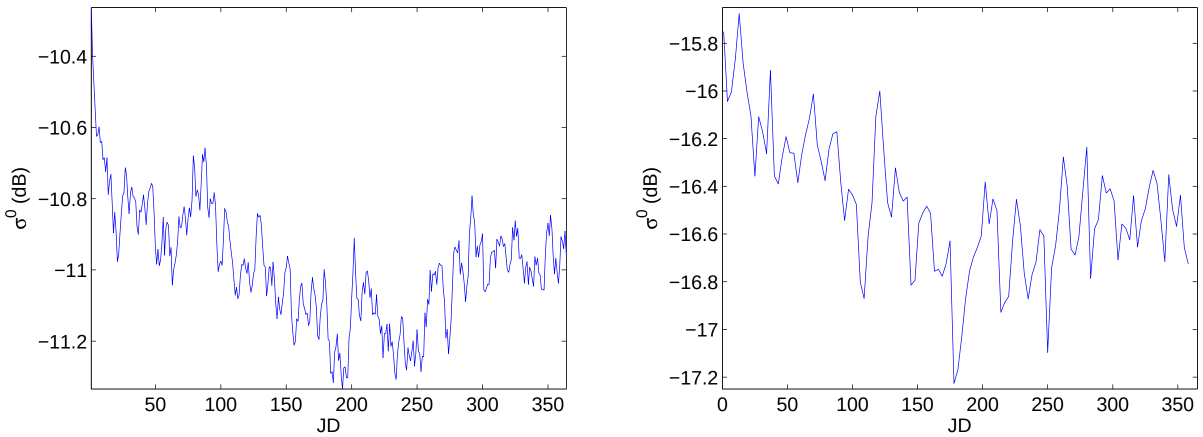

Figure 4.6: Backscatter at the Greenland Summit in 2000 using (left) QuikSCAT and (right) ERS-2 data. QuikSCAT data is smoothed with a 5-day moving average for easier comparison.

from QuikSCAT. If the same seasonal cycling is observed in these other scatterometers, it is unlikely that the QuikSCAT-observed cycling is due only to instrumental effects. However, if seasonal variability in σ^0 has a geophysical cause, it should be visible by other scatterometers. For comparison, $\mathcal{A}$ images from ERS-2 and ASCAT are used.

Figure 4.6 shows σ^0 at the summit in the year 2000 using data from QuikSCAT and ERS-2. This figure shows trends consistent with seasonal variation in both scatterometers. However, the trend is not as strong in the ERS data. This is likely due to the different operating frequency and the lower spatial resolution and temporal resolution of ERS versus QuikSCAT.

Seasonal variation is also present in ASCAT data. Figure 4.7 demonstrates this by showing σ^0 at the summit in the year 2009 using data from QuikSCAT and ASCAT. This figure shows that for ASCAT σ^0 also decreases slightly during the summer months. Other points in the dry snow zone verify the presence of seasonal variation in σ^0 in the dry snow zone for both ASCAT and ERS-2.

Similar temporal behavior in σ^0 in the dry snow zone can also be found in SASS data [4]. Since seasonal variation in σ^0 in the dry snow zone is found in multiple scatterometers at different wavelengths, it is highly unlikely that seasonal variation is driven by instrumental effects. This suggests that the cause of seasonal variation in σ^0 is geophysical.

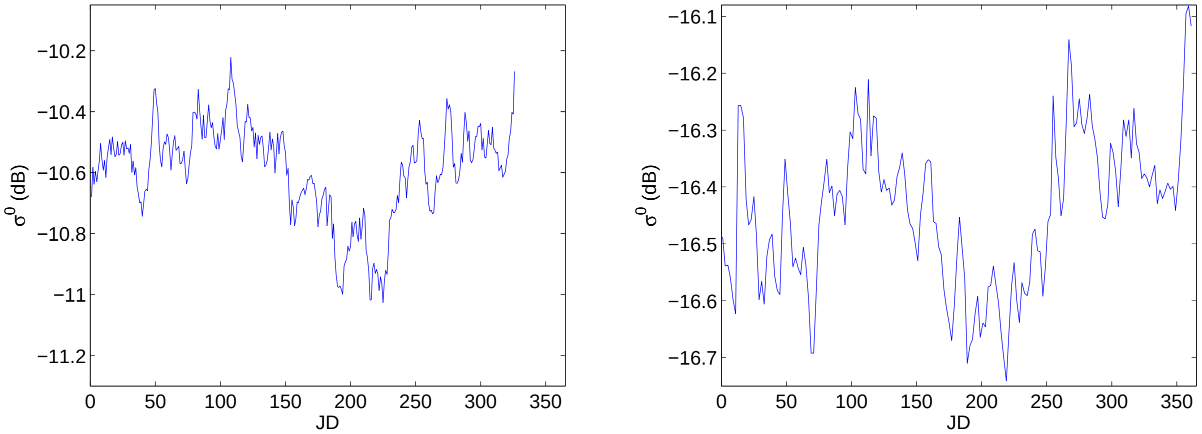

Figure 4.7: Backscatter at the Greenland Summit in 2009 using (left) QuikSCAT and (right) ASCAT data. QuikSCAT data is smoothed with a 5-day moving average for easier comparison. Note that the QuikSCAT data record ends with JD 327 in 2009.

4.5 Summary

None of the tested instrumental parameters including incidence angle, local time of day, and azimuth angle are found to have variations consistent with seasonal variations in σ^0 in the Greenland dry snow zone. Seasonal variation in σ^0 consistent with the seasons of the southern hemisphere is found in Antarctica. Additionally, seasonal variation in σ^0 is present in multiple scatterometers at different wavelengths. This evidence shows that it is highly unlikely that seasonal variation is caused by instrumental effects. Therefore, I conclude that the cause of the seasonal variation in σ^0 in the dry snow zone is geophysical.

Chapter 5

Investigation of Possible Geophysical Causes of Seasonal Variation

The analysis presented in Chapter 4 rules out instrumental parameters as the cause of seasonal variation in σ^0 in the dry snow zone of the Greenland ice sheet. Strong evidence is also given in Chapter 4 that suggests that the cause is geophysical. This chapter investigates several geophysical parameters that may cause seasonal variation in backscatter. These parameters include azimuth modulation, wind speed, and temperature. Temperature is found to be the most likely cause of seasonal variation.

5.1 Azimuth Modulation

As mentioned in Sec. 4.2.2, azimuth modulation is caused by different formations in the ice or snow including sastrugi. These formations may change throughout the year as snow accumulates and wind speeds change. Seasonal changes in these formations could result in variations in azimuth modulation which may account for the seasonal variation in backscatter in the dry snow zone.

A second-order and fourth-order Fourier series are typically chosen to model backscatter dependence on azimuth angle over Greenland [44] and Antarctica [45], respectively. For Greenland,

$$\sigma^0(\phi) = C + M_1 \cos(\phi - \phi_1) + M_2 \cos(2\phi - \phi_2) \tag{5.1}$$

where C is the average backscatter, M_1 and M_2 are the magnitudes of the first- and second-order azimuth modulation respectively, and ϕ_1 and ϕ_2 are the respective directions or orientations of the azimuth modulation.

The parameters C, M_1, M_2, ϕ_1, and ϕ_2 in Eq. (5.1) are estimated for a 30-day sliding window using the L1B data from 2008 at the summit of Greenland. To more easily estimate the parameters with the least squares method, Eq. (5.1) is reduced to an approximately linear function using the angle difference identity

$$\cos(\alpha - \beta) = \cos\alpha \cos\beta + \sin\alpha \sin\beta. \tag{5.2}$$

To measure the change in azimuth modulation over time, define

$$M(\phi) = M_1 \cos(\phi - \phi_1) + M_2 \cos(2\phi - \phi_2). \tag{5.3}$$

This gives the dependence of σ^0 on ϕ. The average dependence of σ^0 on ϕ in an area is then $M(\bar{\phi})$ where $\bar{\phi}$ is the average azimuth angle in the area. The value $M(\bar{\phi})$ over time indicates the change in σ^0 over time due to changes in azimuth modulation.

Table 5.1 gives the estimated values of the parameters in Eq. (5.1), $\bar{\phi}$, and $M(\bar{\phi})$ near the summit in 2008. Many of the estimated values of M_1, M_2, ϕ_1, and ϕ_2 are not statistically significant, suggesting that azimuth modulation does not play a significant role in seasonal variability of σ^0.

This is further demonstrated in Fig. 5.1. This figure shows the actual backscatter and the estimated values of C and $C + M(\bar{\phi})$ over time near the summit. Figure 5.1(b) shows that seasonal variation is visible in C which does not depend on azimuth angle. Adding $M(\bar{\phi})$ to C results in only a slight deepening of the decrease in σ^0. Therefore it is unlikely that azimuth modulation is the driving force behind seasonal variation in σ^0 in the dry snow zone.

5.2 AWS Data

Succeeding sections in this chapter use data from the AWSs. The data used include air temperature and wind measurements. Hourly air temperature and wind measurements on Greenland come from AWSs located on the ice sheet (see Sec. 2.6, especially Fig. 2.8 and Table 2.1). To more easily compare these measurements and σ^0, both data records must have the same time scale. Since σ^0 is given only daily, the average daily AWS measurement (i.e.

Table 5.1: Estimated parameters of Eq. (5.1) at the Greenland summit in 2008. C, M_1, M_2, and $M(\bar{\phi})$ are in dB while ϕ_1, ϕ_2, and $\bar{\phi}$ (average azimuth angle) are in radians.

JD Range	C	M_1	ϕ_1	M_2	ϕ_2	$\bar{\phi}$	$M(\bar{\phi})$
1-30	-10.2266	0.101	1.229	0.022	-0.520	3.1670	-0.018
15-45	-10.0955	0.048	2.480	0.028	0.551	3.1503	0.062
30-60	-10.2467	0.042	2.860	0.027	-1.047	3.2072	0.050
45-75	-10.2728	0.045	2.541	0.024	-2.661	3.0951	0.018
60-90	-10.2408	0.061	2.416	0.044	-2.150	3.0588	0.031
75-105	-10.2752	0.044	1.974	0.068	-2.115	3.1179	-0.014
90-120	-10.3053	0.058	1.750	0.041	-2.648	3.1612	-0.028
105-135	-10.3334	0.111	1.389	0.028	2.441	3.2049	-0.046
120-150	-10.4299	0.135	1.455	0.036	0.976	3.0392	0.012
135-165	-10.5250	0.100	1.409	0.006	2.404	3.1267	-0.019
150-180	-10.5373	0.075	0.124	0.026	0.703	3.1420	-0.055
165-195	-10.5293	0.029	0.588	0.041	-0.107	3.1944	0.015
180-210	-10.5548	0.012	-1.065	0.014	0.531	3.2027	0.008
195-225	-10.5244	0.070	0.675	0.063	1.852	3.1225	-0.074
210-240	-10.5160	0.113	0.785	0.095	1.478	3.1764	-0.067
225-255	-10.5258	0.050	-0.005	0.035	0.787	3.1081	-0.027
240-270	-10.4788	0.050	-1.378	0.040	0.898	3.1595	0.017
255-285	-10.4001	0.008	-1.461	0.005	-1.761	3.1604	-0.002
270-300	-10.3372	0.049	-2.299	0.053	-2.937	3.1275	-0.019
285-315	-10.2896	0.037	-2.168	0.020	1.861	3.1729	0.017
300-330	-10.1899	0.051	-0.370	0.031	0.306	3.1051	-0.019
315-345	-10.1859	0.014	-0.839	0.033	-1.160	3.1395	0.004
330-360	-10.1938	0.034	2.815	0.103	-2.915	3.1148	-0.067

air temperature, wind speed, and wind direction) is calculated and used for each station. This eliminates the diurnal temperature cycle and helps to mitigate noise in the AWS record.

Due to the harsh climate on the ice sheet, the AWS data records often have periods of missing data. Prior to comparing the AWS measurements and σ^0, the data records must be checked for missing data.

Table 5.2 shows the number of days missing temperature data for each station available from 2000 to 2008. According to this table, all of the stations have either less than 18 or more than 36 days of missing data. This provides a range for a threshold to determine how much missing data can be tolerated in the analysis. Additionally, choosing a threshold

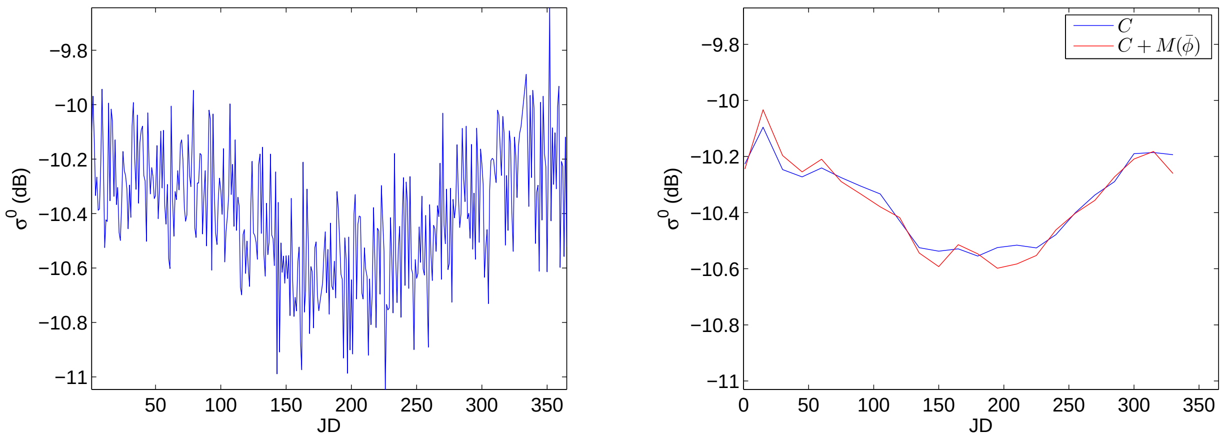

(a) Backscatter

(b) Estimated values from Eq. (5.1).

Figure 5.1: (a) Actual backscatter and (b) estimated values of C and $C + M(\bar{\phi})$ over time near the summit (37.75° W and 72.53° N).

Table 5.2: The number of days missing data in the average daily temperature record and σ^0. Stations and years with x's have bad or little available data in those years.

AWS	2000	2001	2002	2003	2004	2005	2006	2007	2008
1	0	73	0	0	265	6	168	x	x
2	0	0	0	0	14	124	0	48	0
3	5	6	130	153	1	224	72	x	302
4	134	88	60	251	214	193	x	x	x
5	6	4	0	0	0	0	248	87	244
6	0	0	3	0	3	0	0	0	0
7	5	12	0	16	37	0	0	0	243
8	0	11	0	6	0	0	0	0	0
9	117	146	0	12	0	3	0	0	x
10	0	x	0	x	0	1	0	0	0
11	0	0	0	235	0	0	57	0	182
12	6	7	0	14	0	0	87	151	241
13	0	215	x	x	x	x	x	x	x
14	7	5	4	17	0	1	265	0	0
15	0	0	0	0	0	0	12	344	x
16	0	206	x	x	x	x	x	x	x
17	0	0	0	0	0	4	273	153	295
19	x	0	0	0	218	x	x	x	x
21	x	x	154	0	1	5	243	x	x
23	x	x	x	x	x	x	207	166	180
σ^0	1	8	2	0	0	0	2	6	5

Table 5.3: Melt duration in days as determined by the Q-α method at each station and facie classification. Stations and years with x's have been thrown out as determined by the amount of missing days of data in Table 5.2 and the threshold given in the text. Facie classifications are dry snow (DS), percolation (P), wet snow (W), and ablation (A) zones. Combinations of the facies classifications indicate uncertainty or annual variability.

AWS	2000	2001	2002	2003	2004	2005	2006	2007	2008	Facie
1	93	x	87	73	x	86	x	x	x	P/W
2	18	2	30	15	32	x	38	x	8	P/W
3	2	0	x	x	3	x	x	x	x	DS/P
5	0	1	1	0	0	4	x	x	x	DS/P
6	0	0	0	0	0	0	0	0	0	DS
7	0	0	10	0	x	0	0	0	x	DS/P
8	39	11	24	33	51	41	43	74	29	P/W
9	x	x	182	20	86	94	79	78	x	A
10	13	x	4	x	12	9	15	38	5	P/W
11	2	0	1	x	3	7	x	11	x	DS/P
12	0	0	4	0	0	0	x	x	x	DS/P
13	15	x	x	x	x	x	x	x	x	P/W
14	0	0	0	0	0	0	x	0	0	DS
15	7	0	7	4	4	9	10	x	x	DS/P
16	0	x	x	x	x	x	x	x	x	DS
17	96	24	101	2	17	57	x	x	x	A
19	x	358	363	365	x	x	x	x	x	A
21	x	x	x	67	43	43	x	x	x	P/W

in this range ensures that only records with less than 5% missing data are used. Note that a threshold in this range eliminates all data from stations 4 and 23.

The purpose of the AWS data is to determine the cause of seasonal variation in σ^0 in the dry snow zone. To help with this, a correlation analysis is performed. To determine which stations are contained in the dry snow zone, the Q-α method described in Chapter 3 is used. A pixel is classified as dry snow if no melt occurs throughout the entire year. Table 5.3 gives the melt duration for each station. Only those stations classified as dry snow at least once from 2000 to 2008 are used in the analysis. This includes stations 3, 5, 6, 7, 11, 12, 14, 15, and 16. The reason for this is that melting introduces non-linear behavior into σ^0. Since the correlation coefficient measures the linear relationship between two variables, the correlation coefficient at such points gives little insight into the relationship between the AWS data and backscatter.

Some of the stations are located near the edge of the dry snow zone and percolation zone. Melting sometimes occurs at these stations due to their proximity to the dry snow line. Some examples include stations 5, 7, and 11. These stations are included in the analysis since the snow at these stations is occasionally classified as dry snow.

5.3 Wind Speed and Direction

Wind plays an important role in the conditions of the ice sheet. Surface structures such as sastrugi that cause azimuth modulation are formed by wind erosion. Wind direction can influence the orientation of these structures while wind speed can affect the size. While azimuth modulation is unlikely to contribute to seasonal variation in σ^0, wind may affect snow in other ways. Strong wind may cause snow crystals to break apart resulting in a compact snow layers which result in lower backscatter [46]. Wind speed also affects surface hoar formation [47] which may affect backscatter. Additionally, wind speed can affect snow temperature by affecting wind pumping. Wind pumping is caused by wind blowing over the snow surface. Depending on the wind speed and the surface geometry, the air pressure changes which affects the transfer of air through the snow. This can affect snow temperature by transferring warm air into the snow [48]. The warmer air can cause a change in snow conditions resulting in changes in backscatter.

A full analysis of the effects of wind speed and direction on σ^0 in dry snow is beyond the scope of this thesis. However, a basic correlation analysis gives insight into whether wind is directly related to the seasonal variation in σ^0. Wind measurements are taken from AWS and averaged according to the procedure in Sec. 5.2. Generally the correlation coefficient between the wind measurements and σ^0 is negative and small in magnitude (typically less than 0.2). Figure 5.2 shows scatter plots of σ^0, air temperature, wind speed, and wind direction at stations 5 and 6 in 2003. The scatter plots give some insight into the relationship between these parameters and are representative of other locations in the dry snow zone. Table 5.4 gives the correlation coefficients corresponding to Fig. 5.2.

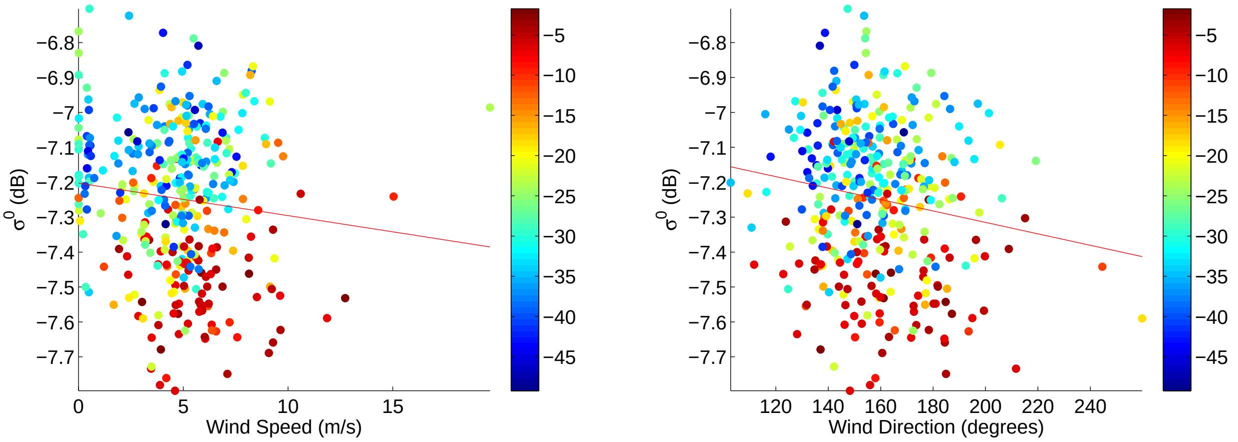

(a) Backscatter vs. wind speed and air temperature at station 5.

(b) Backscatter vs. wind direction and air temperature at station 5.

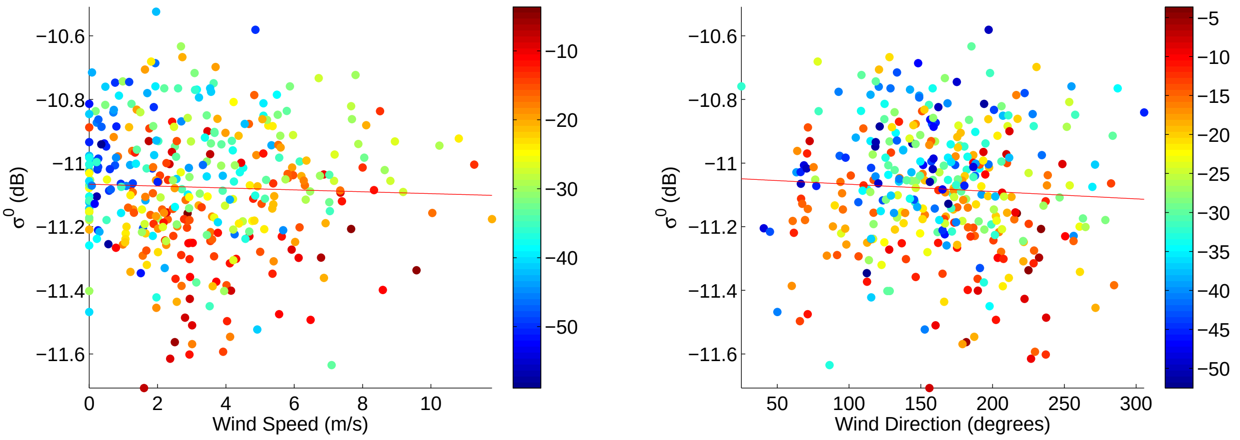

(c) Backscatter vs. wind speed and air temperature at station 6.

(d) Backscatter vs. wind direction and air temperature at station 6.

Figure 5.2: Scatter plots and fitted lines in 2003 of σ^0, air temperature, and (a) wind speed at station 5, (b) wind direction at station 5, (c) wind speed at station 6, and (d) wind direction at station 6. The colors correspond to air temperature in C.

Table 5.4: Correlation coefficients of backscatter with wind speed, wind direction, and air temperature in 2003 at the stations used in Fig. 5.2.

AWS	Wind Speed	Wind Direction	Air Temperature
5	-0.111	-0.157	-0.617
6	-0.036	-0.060	-0.380

Figure 5.2(a) shows a scatter plot of σ^0, wind speed, and temperature at station 5. The correlation coefficient between wind speed and σ^0 at this point is -0.111. This is consistent with the scatter plot which shows a slight negative relationship between wind speed and σ^0. However, the scatter plot shows that there is a stronger relationship between temperature and σ^0. At this point, the correlation coefficient of temperature and σ^0 is -0.617 which is more significant. Temperature and wind speed also appear to be slightly related in this scatter plot. This suggests that the correlation between wind speed and σ^0 may be due to the correlation between temperature and σ^0 and the correlation between temperature and wind speed.

Figure 5.2(c) shows a scatter plot of σ^0, wind speed, and temperature at station 6 in 2003. The correlation coefficient at this point is only -0.036. The scatter plot confirms this which shows that there is no significant relationship between wind speed and σ^0. However, a relationship between backscatter and temperature is present although it is not as clear as in Fig. 5.2(a). This is consistent with a lower (in magnitude) correlation coefficient at this point of -0.380. The low correlation coefficient between wind speed and σ^0 and the higher correlation coefficient between temperature and σ^0 suggest that wind speed may not be directly related to seasonal variation in σ^0 in the dry snow zone.

Wind direction may also affect σ^0. A scatter plot of σ^0, wind direction, and temperature at station 5 in 2003 is given in Fig. 5.2(b). The scatter plot shows a slightly negative correlation between wind direction and σ^0 which is consistent with a correlation coefficient of -0.157. However, as in Fig. 5.2(a), temperature and σ^0 are highly related while temperature and wind direction appear to be slightly correlated. Thus the correlation between wind direction and σ^0 may be due to the correlation between wind direction and temperature.

Figure 5.2(d) gives an example of a station where the wind direction is not significantly correlated with σ^0. This figure shows a scatter plot of σ^0, temperature, and wind direction at station 6 in 2003. This figure does not show a clear relationship between wind direction and σ^0 which is consistent with a low correlation coefficient of -0.060. The low correlation suggests that it is unlikely that wind direction is directly related to the seasonal variation in σ^0.

In conclusion, it is unlikely that the observed seasonal variation in σ^0 in the dry snow zone is directly related to wind speed and direction. The comparatively higher correlation coefficients (in magnitude) of temperature and σ^0 suggest that temperature may be the dominant cause of seasonal variation in σ^0. The relationship between temperature and σ^0 is examined more fully in Sec. 5.4.

5.4 Temperature

An interesting feature of the seasonal variation in dry snow is that it is similar to backscatter behavior in regions where melting occurs such as in the percolation and wet snow zones. The primary difference in the backscatter behavior between these regions and the dry snow zone is the magnitude of the decrease in σ^0. The similarities suggest that temperature may be a factor in seasonal variation in σ^0 in the dry snow zone.

Temperatures below freezing may affect snow backscatter in several ways. First, temperature affects the density of new snow as it accumulates [49], [50] which affects σ^0. Second, at temperatures below freezing, there is a liquid-like layer of water at the surface. The thickness of this layer depends on temperature [51, 52]. The thickness of this layer may influence backscatter values. Third, temperature may affect snow grain growth which also affects backscatter.

This section gives further evidence that temperature may be causing the seasonal variation. This evidence comes from an analysis of seasonal variation near the dry snow line, the correlation of air temperature and backscatter in dry snow, and electromagnetic modeling.

5.4.1 Seasonal Variation Near the Dry Snow Line

The dry snow line is defined as the division between the percolation zone and the dry snow zone [23] and is in the transition region between the dry snow zone and the percolation zone. If temperature is the leading cause of seasonal variation in σ^0, then the change in σ^0 due to melting in the percolation zone should transition smoothly into seasonal variation in the dry snow zone around the dry snow line.

The primary difference between the dry snow zone and the percolation zone is that snow in the percolation zone melts due to the higher temperatures. The presence of liquid water causes σ^0 in the percolation zone to drop rapidly when melting occurs.

Figure 5.3 displays the difference between the dry snow zone and the percolation zone. This figure gives σ^0 from QuikSCAT and air temperature from AWS over time at the summit and Crawford Point 1 (CP1) in 2003 (see Fig. 2.8 for the location of these stations). The summit is the highest point on the ice sheet and is within the dry snow zone. Figure 5.3(b) shows that the air temperature remains below 0° C at the summit the entire year. This is consistent with Fig. 5.3(a) which shows that σ^0 does not experience a precipitous drop commonly associated with melting. However, seasonal variation is still visible in Fig. 5.3(a).

Unlike at the summit, some melting does occur at CP1. Figure 5.3(d) shows that the air temperature does rise above 0° C several times at CP1 during the year. Figure 5.3(c) shows a corresponding drop in σ^0 during those times. Two characteristics of the backscatter behavior suggest that CP1 belongs to the percolation zone and not the wet snow zone. First, the total melt duration is not very long compared to typical locations in the wet snow zone. Second, σ^0 is slightly higher after the melt season than before melting began. This reset behavior is consistent with the formation of subsurface ice structures which are a defining characteristic of the percolation zone.

A smooth transition between the dry snow zone and the percolation zone is visible in 2003 near the dry snow line at points along the line connecting the summit and CP1. Moving along this line from CP1 to the summit results in an increase in altitude and latitude which results in an overall decrease in temperature. Figure 5.4 shows σ^0 over time for three points along this connecting line. The backscatter in 5.4(a) comes from a location in the percolation zone near the dry snow line. At this point, σ^0 drops precipitously for a day or two after which backscatter increases to a level about 1 dB higher than the days immediately preceding the melt event. This is similar to the behavior in Fig. 5.3(c) except less melt has occurred in Fig. 5.4(a).

The second pixel is located in the dry snow zone a short distance from the dry snow line. Figure 5.4(b) shows σ^0 over time at this pixel. At this point, no evidence of melt is

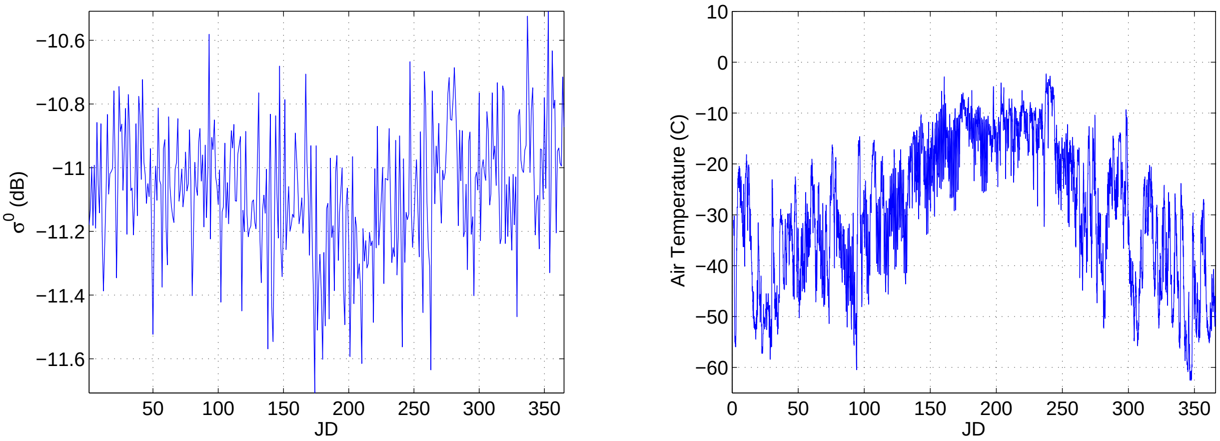

(a) Backscatter at the Summit

(b) Air Temperature at the Summit

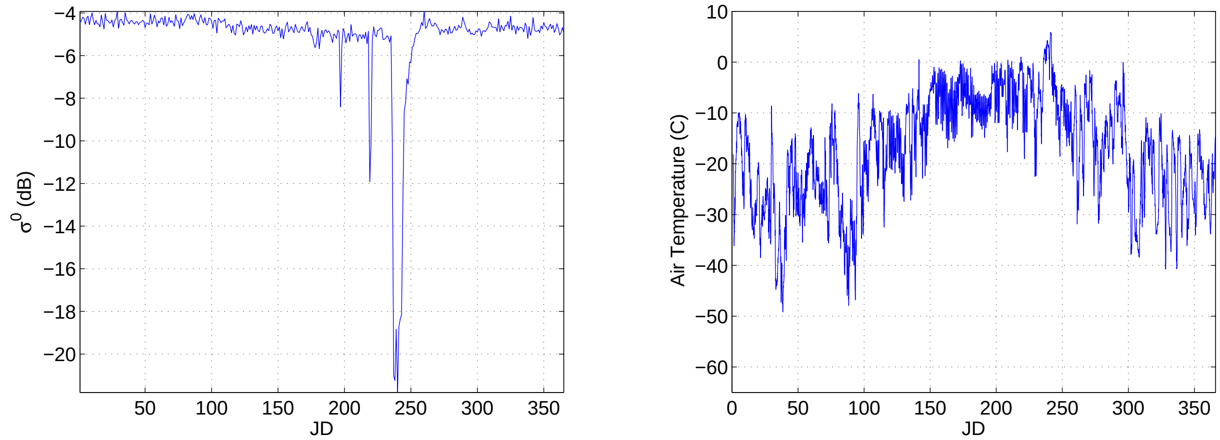

(c) Backscatter at CP1

(d) Air Temperature at CP1

Figure 5.3: Air temperature and QuikSCAT σ^0 over time in 2003 at the summit and CP1. The figures include (a) backscatter at the summit, (b) air temperature at the summit, (c) backscatter at CP1, and (d) air temperature at CP1.

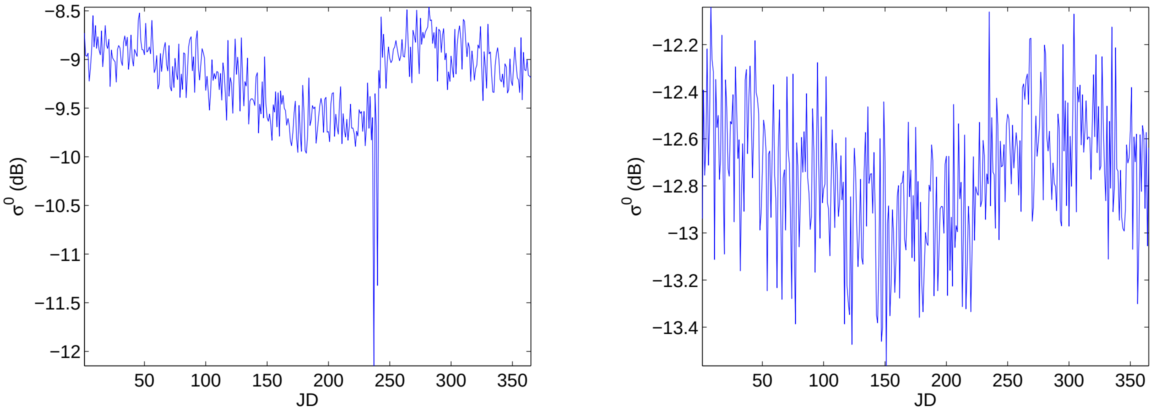

(a) Backscatter in the percolation zone near the dry snow line.

(b) Backscatter in the dry snow zone near the dry snow line.

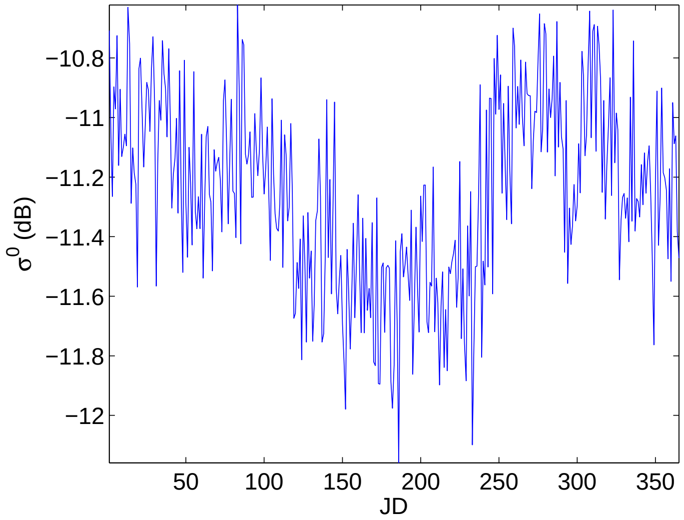

(c) Backscatter in the dry snow zone between points in (a) and (b).

Figure 5.4: Backscatter over time near the dry snow line in 2003 along the line between the summit and CP1. The points are located in the (a) percolation zone (at 45.2059° W and 70.5237° N) and the dry snow zone (at (b) 44.2724° W and 70.8562° N and (c) 44.7430° W and 70.6906° N). These plots demonstrate a transition in σ^0 behavior between the percolation zone and the dry snow zone.

Table 5.5: Calculated correlation coefficient of air temperature and σ^0 at the closest pixel. Bolded values correspond to locations within the dry snow zone.

AWS	2000	2001	2002	2003	2004	2005	2006	2007	2008
3	-0.204	**-0.567**	x	x	-0.240	x	x	x	x
5	**-0.523**	-0.372	-0.510	**-0.617**	**-0.519**	-0.312	x	x	x
6	**-0.478**	**-0.485**	**-0.389**	**-0.380**	**-0.444**	**-0.465**	**-0.482**	**-0.381**	**-0.478**
7	**-0.474**	**-0.613**	-0.279	**-0.598**	x	**-0.647**	**-0.704**	**-0.689**	x
11	-0.313	**-0.456**	-0.358	x	-0.066	-0.360	x	-0.124	x
12	**-0.559**	**-0.513**	-0.029	**-0.539**	**-0.582**	**-0.507**	x	x	x
14	**-0.539**	**-0.456**	**-0.467**	**-0.388**	**-0.511**	**-0.558**	x	**-0.557**	**-0.490**
15	-0.375	**-0.367**	-0.231	-0.481	-0.126	-0.428	-0.391	x	x
16	**-0.333**	x	x	x	x	x	x	x	x

contained within σ^0. However, the backscatter behavior here is a typical example of seasonal variation in dry snow.

Figure 5.4(c) shows the backscatter over time in the dry snow zone near the dry snow line and between the points in Figs. 5.4(a) and 5.4(b). Here σ^0 decreases and levels out during the summer months which is typical behavior for seasonal variation in the dry snow zone. However, at approximately JD 240, σ^0 abruptly increases in a manner similar to a refreeze event in melted snow despite the lack of evidence in σ^0 of a melt event. The behavior of σ^0 in Fig. 5.4(c) is similar to the σ^0 behavior in both Figs. 5.4(a) and 5.4(b). This suggests that the pixel in Fig. 5.4(c) is a transitional pixel between the other two pixels. Since temperature variation is the known cause of variation in σ^0 in the percolation zone, and since this transitional behavior is correlated with a decrease in overall temperature, this suggests that the variation in σ^0 in this transitional region and in the dry snow zone is also caused by temperature variation.

5.4.2 Correlation of Temperature and Backscatter

Figure 5.3 shows that temperature and σ^0 appear to be correlated even at temperatures below freezing. This section provides a detailed correlation analysis of air temperature and backscatter in the dry snow zone. Prior to calculating the correlation coefficient, the average daily temperature is calculated as described in Sec. 5.2.

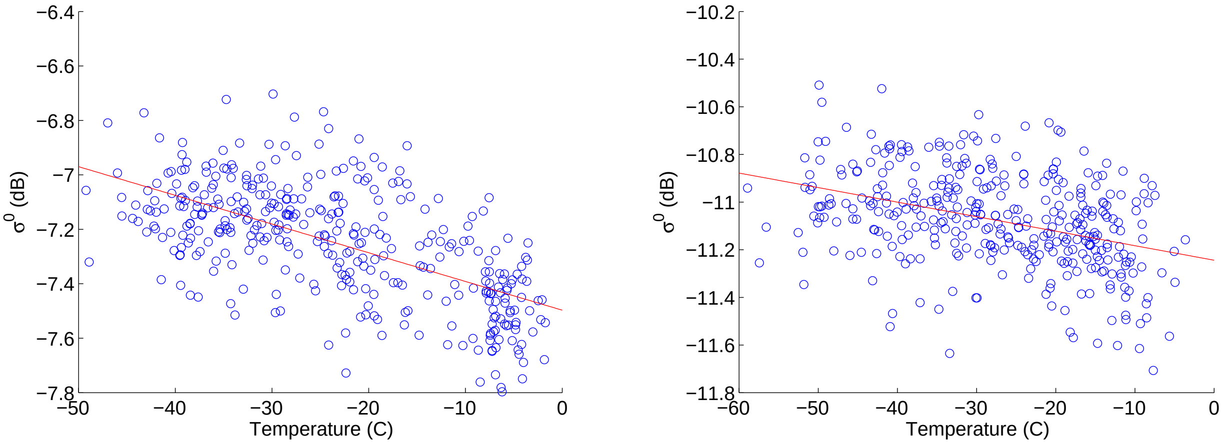

(a) Station 5

(b) Station 6

Figure 5.5: Scatter plot and fitted line in 2003 of backscatter and air temperature at stations (a) 5 and (b) 6.

Table 5.5 gives the calculated correlation coefficient of air temperature and σ^0 at each of the selected stations while Fig. 5.5 shows scatter plots of σ^0 and air temperature at stations 5 and 6 in 2003. The scatter plots show that temperature and σ^0 appear to be negatively correlated. Additionally the coefficients in Table 5.5 in the dry snow zone are significant. However, the coefficients are not as high in magnitude as would be expected if temperature is the primary determinant of seasonal variation. The range of correlation coefficients in the dry snow zone is from -0.333 to -0.704.

There are several possible explanations for the lower correlation coefficients. First, noise could be affecting the correlation coefficient. Figure 5.3 shows that noise is high in both air temperature and σ^0. High noise could mask the dependence of σ^0 on temperature and lower the magnitude of the correlation coefficient. Second, other factors such as accumulation can affect σ^0. Third, the parameters that depend on temperature and affect backscatter depend on snow temperature. While air temperature and snow temperature are related, they are not equal. Unfortunately, snow temperature measurements from AWS are not very reliable. Thus air temperature is used as a substitute.

Table 5.6: Calculated correlation coefficient of smoothed air temperature and smoothed σ^0 at the closest pixel. Smoothing was performed with a 7 day moving average. Bolded values correspond to locations within the dry snow zone.

AWS	2000	2001	2002	2003	2004	2005	2006	2007	2008
3	-0.231	**-0.664**	x	x	-0.325	x	x	x	x
5	**-0.656**	-0.634	-0.731	**-0.867**	**-0.776**	-0.448	x	x	x
6	**-0.723**	**-0.751**	**-0.668**	**-0.721**	**-0.679**	**-0.713**	**-0.771**	**-0.625**	**-0.741**
7	**-0.752**	**-0.842**	-0.330	**-0.837**	x	**-0.880**	**-0.890**	**-0.898**	x
11	-0.383	**-0.586**	-0.461	x	-0.055	-0.483	x	-0.123	x
12	**-0.832**	**-0.752**	-0.011	**-0.728**	**-0.874**	**-0.744**	x	x	x
14	**-0.731**	**-0.694**	**-0.695**	**-0.632**	**-0.800**	**-0.776**	x	**-0.811**	**-0.686**
15	-0.565	**-0.420**	-0.347	-0.658	-0.122	-0.555	-0.513	x	x
16	**-0.400**	x	x	x	x	x	x	x	x

Two methods can be used to mitigate noise: temporal smoothing and spatial averaging. Table 5.6 gives the resulting correlation coefficients after smoothing both air temperature and σ^0 using a 7 day moving average.

Comparing Tables 5.5 and 5.6 shows that smoothing the data does increase the magnitude of the correlation coefficient in the dry snow zone. The range of correlation coefficients becomes -0.400 to -0.898 with most values greater than 0.6 in magnitude.

There are four values of note in Table 5.6. The first three are associated with station 16 in 2000 and stations 11 and 15 in 2001. These are the only three stations in the dry snow zone with a correlation coefficient smaller than 0.6 in magnitude. These three stations are found in the southern part of Greenland where accumulation is higher (see Figs. 2.5 and 2.8 and Table 2.1). Figures 5.6(a)–5.6(c) show σ^0 over time at these three points. These points are similar in that σ^0 gradually decreases throughout the year. This is typical of areas with high accumulation and frequent melt. Since accumulation is dominating over seasonal variation at these points, the correlation coefficients are lower.

The fourth value (see Fig. 5.6(d)) is associated with station 12 in 2002. This station only had four days of melt in this year and is typically classified as dry snow. However, the correlation coefficient at this point in 2002 is virtually zero. The backscatter at this point displays two resets after the melt events. This non-linear behavior results in low correlation between backscatter and temperature. The non-linear behavior in σ^0 caused by melting is

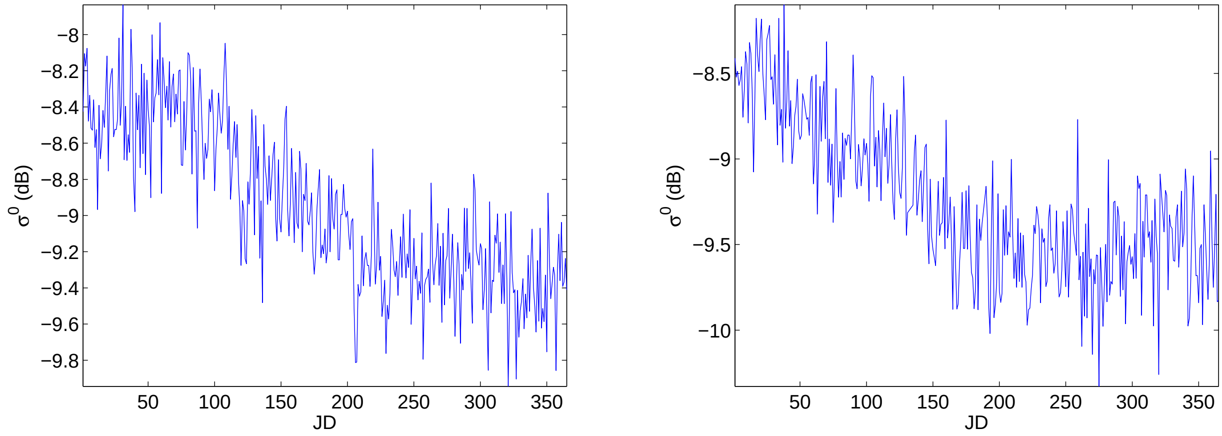

(a) Backscatter over time at station 16 in 2000.

(b) Backscatter over time at station 11 in 2001.

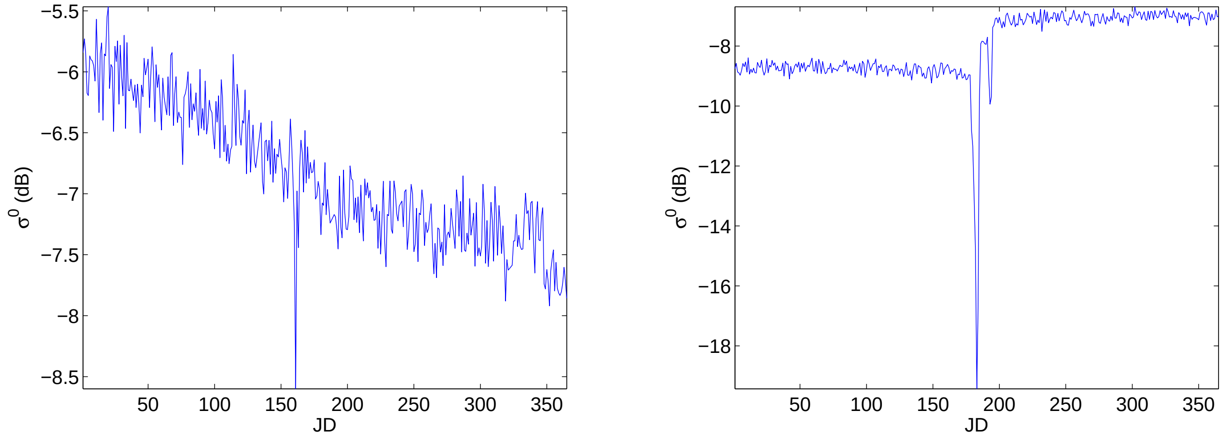

(c) Backscatter over time at station 15 in 2001.

(d) Backscatter over time at station 12 in 2002.

Figure 5.6: Backscatter over time at (a) station 16 in 2000, (b) station 11 in 2001, (c) station 15 in 2001, and (d) station 12 in 2002. The correlation coefficients at these stations are lower than other values in Table 5.6. Bolded values correspond to locations within the dry snow zone.

Table 5.7: Calculated correlation coefficient of temperature and the spatial average of σ^0 for each year of the entire dry snow zone (see Fig. 3.20). The bottom row gives the correlation coefficient for the spatially averaged temperature and the spatial average of σ^0. Bolded values correspond to locations within the dry snow zone.

AWS	2000	2001	2002	2003	2004	2005	2006	2007	2008
3	-0.748	**-0.696**	x	x	-0.806	x	x	x	x
5	**-0.782**	-0.778	-0.702	**-0.916**	**-0.831**	-0.793	x	x	x
6	**-0.741**	**-0.711**	**-0.683**	**-0.794**	**-0.809**	**-0.773**	**-0.858**	**-0.835**	**-0.799**
7	**-0.800**	**-0.779**	-0.744	**-0.893**	x	**-0.814**	**-0.892**	**-0.911**	x
11	-0.745	**-0.704**	-0.658	x	-0.773	-0.690	x	-0.781	x
12	**-0.794**	**-0.725**	-0.719	**-0.845**	**-0.855**	**-0.803**	x	x	x
14	**-0.777**	**-0.725**	**-0.698**	**-0.822**	**-0.833**	**-0.778**	x	**-0.863**	**-0.822**
15	-0.711	**-0.686**	-0.654	-0.756	-0.791	-0.743	-0.830	x	x
16	**-0.737**	x	x	x	x	x	x	x	x
Average	-0.813	-0.786	-0.737	-0.895	-0.865	-0.838	-0.925	-0.901	-0.810

also the reason for the lower correlation coefficients (in magnitude) outside of the dry snow zone in Table 5.6.

Spatial averaging can also be used to mitigate noise. Table 5.7 gives the correlation coefficients of temperature and the spatial average of σ^0 of the entire dry snow zone for each year. The bottom row gives the correlation coefficient of the spatial average of temperature and the spatial average of backscatter. Within the dry snow zone, the values are comparable to those in Table 5.6. However, outside of the dry snow zone, the correlation coefficients are higher in magnitude in Table 5.7 than in Table 5.6. In general, temperature is spatially correlated; e.g. warm weather in one pixel is accompanied by warm weather in nearby pixels. For the values of the correlation coefficients in Table 5.7, the spatial average of σ^0 is the same for all stations in a given year and is restricted to the dry snow zone. Therefore, non-linear σ^0 behavior associated with melt is not present in this spatial average. Since temperature is spatially correlated, the correlation coefficients at stations outside of the dry snow zone are similar in magnitude to the stations inside the dry snow zone. An example of this is stations 12 and 14.

The bottom row in Table 5.7 shows that the magnitude of the correlation coefficient of the spatial average of σ^0 and the spatial average of temperature is on average higher than the magnitude of the correlation coefficient of the spatial average of σ^0 and the temperature

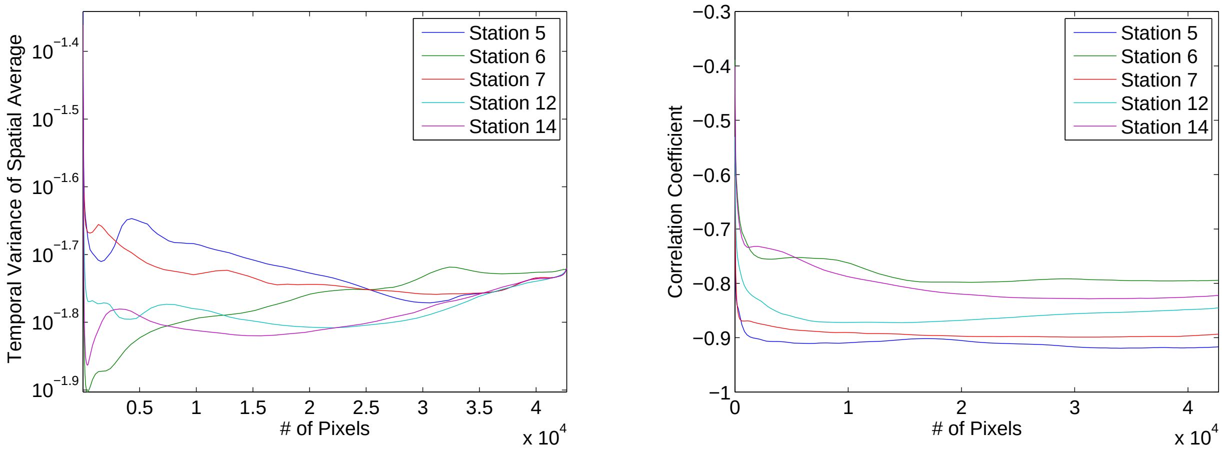

(a) Temporal Variance

(b) Correlation Coefficient

Figure 5.7: (a) Temporal variance and (b) the correlation coefficient with temperature of the spatial average of σ^0 as a function of the number of pixels used to calculate the average in 2003. The spatial average is initially centered around the station but limited to the dry snow zone (see text).

at the individual stations. This suggests that spatial averaging may affect the correlation coefficient in ways besides noise mitigation. The analysis in Appendix A demonstrates that spatial averaging can artificially inflate the correlation coefficient. However, simulation results in Appendix A also suggest that the more two locations are correlated, the less this occurs. Thus spatial averaging should be limited to small regions that are correlated in temperature and σ^0 to avoid artificial inflation of the correlation coefficient.

A possible range for the number of pixels that should be used in the spatial average to mitigate noise can be deduced from the results in Fig. 5.7. This figure shows the annual variance of the spatial average of σ^0 and the correlation coefficient of the spatial average and temperature in 2003 as a function of the number of pixels used to calculate the spatial average. The spatial average is calculated from a region initially centered around the AWS but restricted to the dry snow zone. This means that the center of the region eventually shifts away from the station as the region grows in size until the region is the entire dry snow zone.

The temporal variance of the spatial average is found by calculating the variance of the spatial average over the whole year. Due to seasonal variation, the variance is nonzero. However, spatially averaging σ^0 should mitigate noise and thus decrease the temporal variance as long as the pixels used in the averaging have correlated backscatter. This may explain the behavior of the temporal variance in Fig. 5.7(a). The variance of the spatial average rapidly decreases initially as the number of pixels used in the average increases. However, the variance achieves a local minimum typically between 361 and 625 pixels and begins increasing as the number of pixels used increases further. The increase in variance may be due to a decrease in correlation of the pixels. As less-correlated pixels are included in the average, the σ^0 behavior over time varies more widely resulting in an increased temporal variance.

For stations 6 and 14, the variance never decreases below the first local minimum while stations 5, 7, and 12 eventually achieve a lower variance. This behavior may be explained by the location of the stations. Figure 2.8 and Table 2.1 show that stations 6 and 14 are located in the interior of the dry snow zone while stations 5, 7, and 12 are located closer towards the edges. The results in Chapter 3 demonstrate that backscatter is somewhat more volatile towards the edges of the dry snow zone which results in a higher temporal variance in these regions. Since stations 6 and 14 are located in the less variant interior of the dry snow zone, the variance achieves the minimum by using pixels nearby the station. As the region increases in size, less correlated pixels and more of the edge pixels are included which results in an increase in the temporal variance.

A similar effect occurs in stations 5, 7, and 12. In these regions, the initial decrease in variance is likely due to noise mitigation. As less correlated pixels are included in the average, the temporal variance increases. But as the region grows to include more pixels from the central part of the dry snow zone, pixels with less temporal variance are included in the spatial average. As these pixels begin to dominate, the temporal variance again decreases.

The results from this discussion suggest that to mitigate noise effects on the correlation coefficient of σ^0 and temperature, the maximum number of pixels used in spatial averaging of σ^0 should be limited to the range of 361 to 625 pixels. Using more pixels than this may include less correlated pixels which may result in inaccurate results. This is consistent with Fig. 5.7(b) which gives the correlation coefficient of temperature and the spatial average of σ^0 as a function of the number of pixels used in the spatial average. This figure shows that most of the gain in the magnitude of the correlation coefficient occurs prior to the range of 361 to 625 pixels.

Summary

The results in this section demonstrate that air temperature is significantly correlated with σ^0 in the dry snow zone. Techniques such as temporal smoothing and spatial averaging maintain the general shape of the seasonal variation in σ^0 while mitigating noise. This results in higher correlation coefficient magnitudes. Thus temperature is related to the seasonal variation in σ^0 in the dry snow zone.

5.4.3 Electromagnetic Model

In this section, an electromagnetic model is developed from [49, 50, 53, 54, 55] which relates temperature at levels below freezing to backscatter by using theoretically and empirically derived relations between temperature and snow density, snow density and permittivity, and permittivity and backscatter. The results of the model using AWS data are then compared to QuikSCAT data.

The electromagnetic model is based on several simplifying assumptions which limit its accuracy. First, the Greenland ice sheet is assumed to be a single infinite layer of snow. Second, surface scattering is assumed to be negligible and snow crystals are assumed to remain the same size at all subfreezing temperatures. Third, backscatter is assumed to be unaffected by snow accumulation and wind speed. Fourth, the liquid-like layer of water is ignored. Fifth, the snow density is assumed to be constant with respect to depth. Finally, the temperature dependence of backscatter is restricted to between $-20°$ and $0°$ C. These assumptions simplify the model while limiting the accuracy. Unfortunately, including these factors in the model requires access to grain size measurements and other *in situ* data that is not available to me.

Relating Temperature to Snow Density and Permittivity

Snow density is defined as the mass of the snow divided by the volume of the snow. The units are given in g/cm^3. Data relating air temperature to snow density is found in [49] and [50]. From this data, an empirical relationship between temperature and snow density is derived for temperatures between $-20°$ and $0°$ C. Given a temperature t (Celsius), the density of new snow ρ_s is roughly given by

$$\rho_s = \frac{11}{1400}t + \frac{109}{700}. \tag{5.4}$$

Snow density affects permittivity. In [55], snow is modeled as spherically shaped ice crystals in some background medium. In the case of dry snow, the background is simply air. The real part of the permittivity of dry snow, ϵ'_{ds}, is found to be related to the snow density by

$$\epsilon'_{ds} = (1 + 0.51\rho_s)^3. \tag{5.5}$$

The imaginary part ϵ''_{ds} depends on the real part of the permittivity of dry snow and the permittivity of ice ϵ_i [55]. It is given as

$$\epsilon''_{ds} = 3v_i\epsilon''_i \frac{(\epsilon'_{ds})^2(2\epsilon'_{ds} + 1)}{(\epsilon'_i + 2\epsilon'_{ds})(\epsilon'_i + 2(\epsilon'_{ds})^2)} \tag{5.6}$$

where v_i is the volume fraction of ice in the snow given by $v_i = \rho_s/0.916$ where 0.916 is the density of pure ice. The parameter ϵ'_i is assumed to have a constant value of 3.15. The imaginary part of the permittivity of ice ϵ''_i depends on the operating frequency of the scatterometer and the conductivity of ice which does vary slightly with temperature [56].

Relating Permittivity and Snow Density to Received Backscatter

Assuming surface scatter is negligible, the backscatter of the scatterometer in an infinite layer of dry snow is given as [54]

$$\sigma^0(\theta) = \Upsilon^2(\theta)\frac{\sigma_v \cos(\theta')}{2\kappa_e} \tag{5.7}$$

where $\Upsilon(\theta)$ is the transmissivity of the air-snow surface, θ is the angle of incidence, σ_v is the volume backscattering coefficient, θ' is the transmitted angle, and κ_e is the extinction coefficient. Since the results are compared to QuikSCAT, a fixed θ of 54° is used while θ' is calculated using Snell's law. The parameters $\Upsilon(\theta)$, σ_v, and κ_e all depend on the permittivity of the snow. The transmissivity of the air-snow surface for a vertically polarized wave is given as [53]

$$\Upsilon = \frac{\mathbf{Re}(\eta' \cos\theta')}{\mathbf{Re}(\eta \cos\theta)}|T|^2 \tag{5.8}$$

where T is the transmission coefficient given as [53]

$$T = \frac{2\eta' \cos\theta}{\eta \cos\theta + \eta' \cos\theta'}, \tag{5.9}$$

and where η and η' are the intrinsic electrical impedance of air and snow respectively.

To calculate the extinction coefficient of dry snow, the layer of dry snow is modeled as "a dielectric medium consisting of *ice crystals* in an *air background*" [55]. The ice crystals in snow are assumed to be spherical in calculating κ_e. The extinction coefficient is then given as [55]

$$\kappa_e = \kappa_a + \kappa_s \tag{5.10}$$

where κ_a and κ_s are the absorption and scattering coefficients respectively. The absorption coefficient has two components

$$\kappa_a = \kappa_{ai} + \kappa_{ab}. \tag{5.11}$$

The κ_{ai} component corresponds to the absorption caused by the ice spheres while κ_{ab} corresponds to the absorption caused by the background. In the case of dry snow, the background is air. Therefore, $\kappa_{ab} = 0$ and if Rayleigh scattering is assumed then

$$\kappa_a = \kappa_{ai} = \frac{6\pi v_i}{\lambda}\mathbf{Im}(-K), \tag{5.12}$$

where λ is the wavelength in air and [55]

$$K = \frac{\epsilon_i - 1}{\epsilon_i + 2}. \tag{5.13}$$

Scattering in snow is caused by the ice particles in the snow. The expression for the scattering coefficient is given as

$$\kappa_s = \kappa_{si} = N_v Q_s \tag{5.14}$$

where Q_s is the scattering cross section of each ice particle, and N_v is the number density of the ice particles given as

$$N_v = \frac{v_i}{\frac{4}{3}\pi r^3} \tag{5.15}$$

where r is the particle radius [55]. The scattering cross section Q_s depends on the parameter $\chi = \frac{2\pi r}{\lambda}$ and is given as [53]

$$Q_s = \frac{2\lambda^2}{3\pi}\chi^6 \left|K\right|^2 = \frac{128\pi^5 r^6}{3\lambda^4}\left|K\right|^2. \tag{5.16}$$

The volume backscattering coefficient σ_v can be defined in terms of the density ρ_s and the mass volume-scattering coefficient σ_{vm} as [54]

$$\sigma_v = \rho_s \sigma_{vm}. \tag{5.17}$$

Due to lack of data, the parameter σ_{vm} is unknown. In this model, it is used as a tuning parameter when comparing the model results to QuikSCAT data. When comparing actual

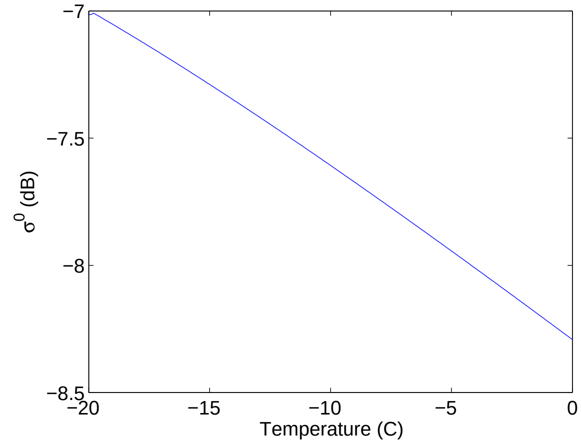

Figure 5.8: Simulated backscatter dependence on temperature. In this plot, $\sigma_{vm} = 0.1$.

σ^0 to simulated backscatter, the value of σ_{vm} is chosen to align the simulated data with the actual data. Since the dependence of simulated σ^0 on σ_{vm} is multiplicative, the dependence in dB is additive. Therefore, tuning the simulated σ^0 with σ_{vm} is equivalent to shifting the simulated backscatter in dB.

Figure 5.8 shows the simulated backscatter for temperatures between $-20°$ and $0°$ C. This figure shows that according to the model, temperature can cause backscatter to vary by more than 1 dB in dry snow. While this is slightly higher than the observed seasonal variation in σ^0, this provides evidence that temperature may be causing the seasonal variation in σ^0.

Comparison to QuikSCAT Data

Figures 5.9 to 5.11 show the simulation results using AWS data at three locations in different years. The first location (Fig. 5.9) is at station 6 in 2003. The simulated backscatter follows the actual backscatter during the summer months quite well especially from JD 164 to 217. After these days, the simulated backscatter tends to overestimate the decrease in σ^0. However, the simulated backscatter still tracks the general trend quite well even though the correlation coefficient of temperature and σ^0 at this point is only -0.389. During the winter months, the simulated backscatter is constant using this model. This is due to the assumption in the model that temperature only affects snow at temperatures between $-20°$

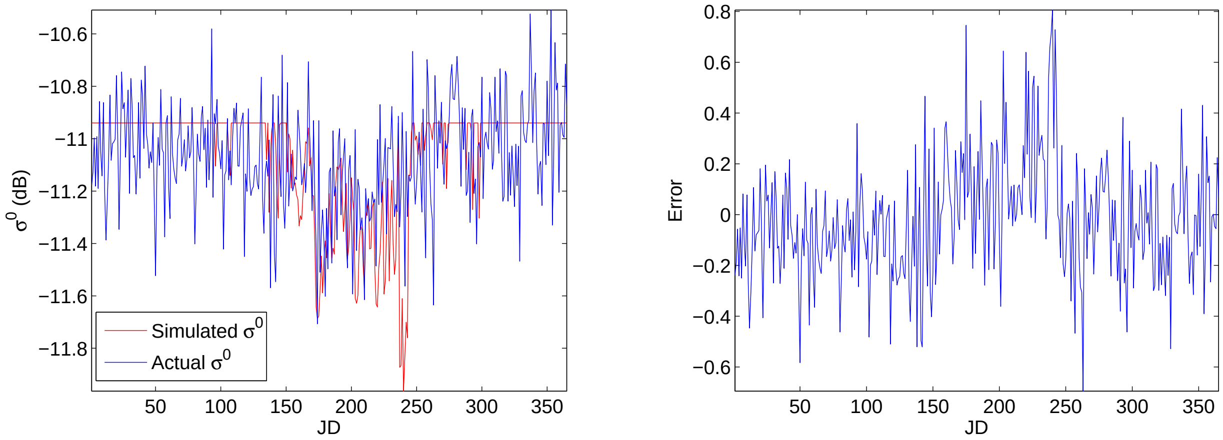

(a) Simulated and actual backscatter.

(b) Error in dB.

Figure 5.9: Simulation results at station 6 in 2003. The correlation coefficient between temperature and σ^0 is -0.380. (a) Simulated and actual backscatter and (b) the error.

and 0° C. The actual backscatter is not constant during the winter. This is likely due to noise and other factors that influence backscatter such as accumulation.

The simulated results are compared to the actual backscatter at station 5 in 2004 in Fig. 5.10. This figure shows that the simulated backscatter consistently overestimates the decrease in σ^0 during the summer months. This is expected since the simulated backscatter dependence on temperature in Fig. 5.8 shows a wider range in σ^0 than is typically observed. Overestimation could occur from failing to account for grain growth in the model which can increase σ^0. However, the simulated backscatter does track the general behavior of σ^0 fairly well during this time period.

Figure 5.11 shows the results at station 7 in 2006. At this point, the correlation coefficient between temperature and actual σ^0 is -0.704. However, the simulated backscatter does not track the actual backscatter as well as in the previous two examples. For example, the simulated backscatter does not begin to decrease at the same time as the actual backscatter. This could be due to accumulation which is not included in the model and causes a decrease in backscatter. However, the high correlation of σ^0 with low temperature suggests that temperature may also affect σ^0 at temperatures below $-20°$ C. Additionally,

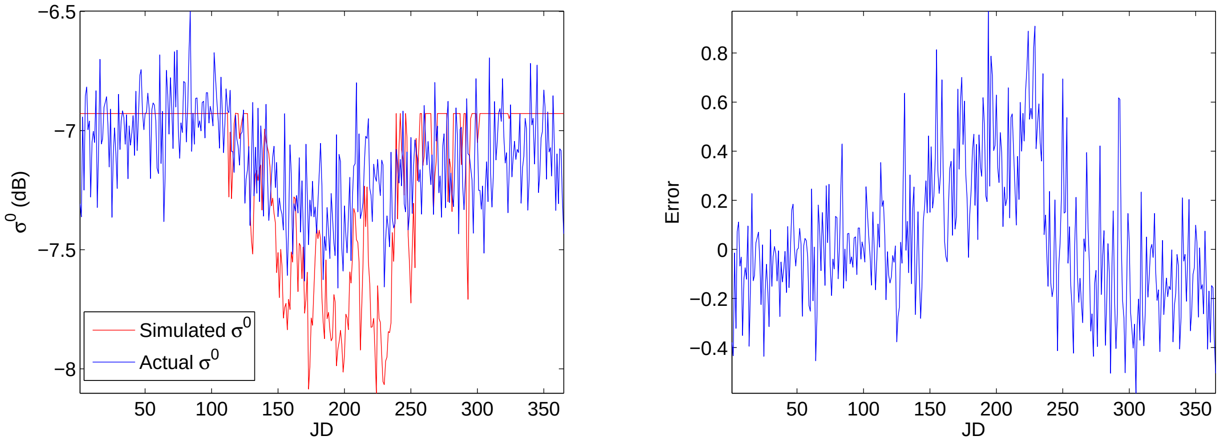

(a) Simulated and actual backscatter.

(b) Error in dB.

Figure 5.10: Simulation results at station 5 in 2004. The correlation coefficient between temperature and σ^0 is -0.519. (a) Simulated and actual backscatter and (b) the error.

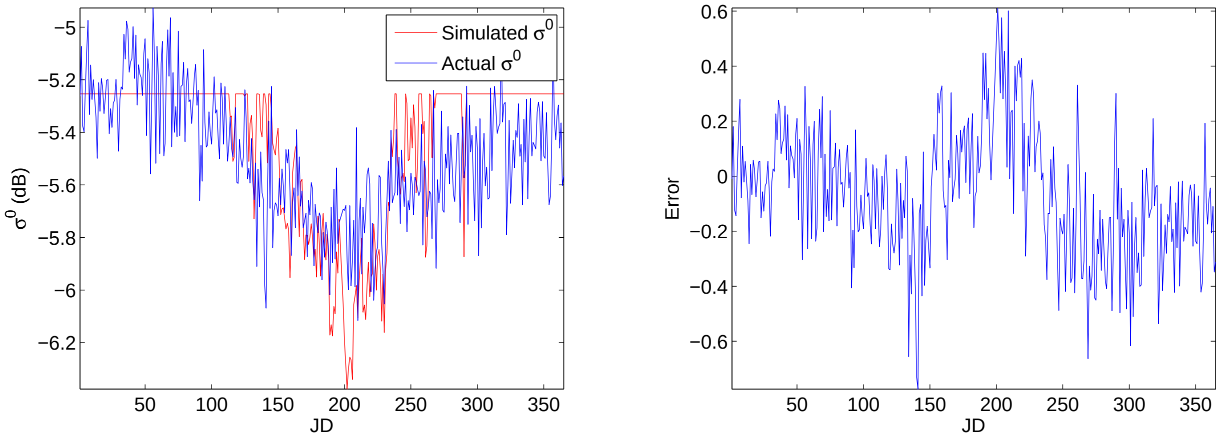

(a) Simulated and actual backscatter.

(b) Error in dB.

Figure 5.11: Simulation results at station 7 in 2006. The correlation coefficient between temperature and σ^0 is -0.704. (a) Simulated and actual backscatter and (b) the error.

the estimated backscatter is generally higher at the end of the year than the actual backscatter. The actual backscatter is lower due to effects not accounted for in the model such as snow accumulation.

Overall, the simulated backscatter tracks the general movement of the actual backscatter quite well. The simulated backscatter tends to overestimate the decrease in σ^0 during the summer months. This may be due to the exclusion of snow grain growth in the model. Additionally, the simulated backscatter does not always begin to decrease as early as the actual backscatter. This may be due to the exclusion of accumulation or a possible backscatter dependence on temperatures below $-20°$ C. Including these parameters would increase the accuracy of the model but the lack of information precludes it. Despite the limitations of the model, the performance of the model suggests that temperature plays an important role in backscatter in the dry snow zone and that seasonal variations in temperature may be causing the seasonal variation in σ^0.

5.5 Summary

The temporal behavior of backscatter in the dry snow zone, the high correlation between temperature and σ^0 in dry snow, and electromagnetic modeling of dry snow all suggest that the seasonal temperature patterns are driving the seasonal variation in σ^0. Wind speed and direction may play a small role in seasonal variation in σ^0 although the relationship with temperature is generally much stronger. Temporal variations in azimuth modulation do not appear to influence the seasonal variation. Therefore, I conclude that seasonal temperature patterns are the primary driver of the seasonal variation in σ^0 in the dry snow zone.

Chapter 6

Conclusion

The Greenland ice sheet is an important factor that influences the global climate. Because of this influence, knowledge of temporal changes in the ice sheet is crucial to understanding changes in the global climate. Scatterometer measurements are useful for studying these temporal changes in the ice sheet because of their sensitivity to snow grain size, the presence of liquid water, and subsurface features.

The dry snow zone is the largest facie of the ice sheet and is important for its role in the earth's climate. Additionally, since σ^0 in dry snow is relatively constant over time, backscatter measurements in the dry snow zone can be used in scatterometer calibration. Studying the temporal backscatter in the dry snow zone aids in understanding the temporal changes in the dry snow zone and in scatterometer calibration. Unanticipated seasonal variation in QuikSCAT backscatter in the dry snow zone is mentioned in Chapter 3. It is important to understand the cause of the seasonal variation to verify the accuracy of QuikSCAT products, to better understand the ice sheet conditions, and to improve scatterometer calibrations.

This thesis provides a study of the temporal behavior of backscatter in the dry snow zone of the Greenland ice sheet focusing on seasonal variation. QuikSCAT SIR images of the Greenland ice sheet are used to identify the dry snow zone using the Q-α melt detection method and altitude thresholding. This method of dry snow zone identification displays interannual consistency as well as some variability that takes into account changes in the ice sheet. Spatial averaging and the KL transform are used to identify and study the dominant patterns in annual backscatter behavior. Seasonal variation is well-described by a low-order basis generated by the KL transform.

Several instrumental parameters including incidence angle, local time of day, azimuth angle, and others are tested as possible causes of seasonal variation in σ^0 in the dry snow zone. These parameters are tested to verify the accuracy of QuikSCAT measurements. None of these parameters are found to be related to seasonal variation. Further evidence suggests that the cause of the seasonal variation is geophysical. The temporal behavior of backscatter in the dry snow zone, the high correlation between temperature and σ^0 in dry snow, and electromagnetic modeling of dry snow all lead me to conclude that the seasonal temperature patterns are driving the seasonal variation in σ^0. Wind may also play a minor role in causing the seasonal variation.

6.1 Contributions

The research contributions of this thesis include the following:

1. Maps of the dry snow zone from 2000 to 2008 are created from QuikSCAT SIR images. They are derived using the Q-α method and altitude thresholding. This method of dry snow zone classification displays interannual consistency as well as some variability that takes into account changes in the ice sheet.

2. Observations of temporal behavior in σ^0 in dry snow are provided. The KL transform and spatial averaging are used to identify and study the dominant patterns in annual backscatter behavior. The backscatter can be accurately reconstructed by estimating the coefficients of the resulting basis. The patterns found using the KL transform include seasonal variation, resets, and general decreases in backscatter. Seasonal variation is found to be the dominating pattern in σ^0 in the dry snow zone. Additionally, regions of reset behavior can be predicted using the values of the estimated coefficients.

3. Possible instrumental causes of seasonal variation in σ^0 in the dry snow zone are investigated to verify the accuracy of QuikSCAT measurements. All of the tested instrumental parameters are ruled out as causes of the seasonal variation. Therefore it is unlikely that seasonal variation in σ^0 affects the accuracy of existing scatterometer products. The possible causes investigated include incident angle variation, orbital drift, local time of day variation, and azimuth angle variation.

4. Strong evidence is provided that seasonal variability in σ^0 in the dry snow zone is caused by geophysical effects. This evidence includes similar seasonal variability in

Antarctica, the spatial consistency and variability of seasonal variation in Greenland, and the presence of seasonal variation in multiple scatterometers.

5. An analysis of the effects of averaging random variables on the correlation coefficient with a separate random variable is performed and verified by simulation. It is found, for example, that averaging σ^0 for adjacent pixels and then correlating the average with air temperature results in a correlation coefficient higher than the average of the individual correlation coefficients. Based on patterns in the temporal variance of σ^0, it is concluded that the maximum number of pixels included in a spatial average for noise mitigation may be limited to between 361 and 625 pixels.

6. Several potential geophysical causes of seasonal variation in σ^0 are investigated. These geophysical effects include azimuth modulation, wind, and temperature. Variation in azimuth modulation is unlikely to contribute to seasonal variation while wind may play a minor role. Temperature is highly related to backscatter in the dry snow zone. Evidence of this relation is found in backscatter in the dry snow zone near the dry snow line, the high correlation of σ^0 with temperature, and electromagnetic modeling.

6.2 Future Work

The work in this thesis can be extended in a variety of ways. Examples are given in the following:

1. A method of automatically identifying the dry snow zone using QuikSCAT SIR images is presented in this thesis. Future research could include identifying the other facies of the ice sheet. The KL transform could be applied to the region outside of the identified dry snow zone to find the dominating temporal patterns in σ^0. This may aid in distinguishing between the percolation, wet snow, and ablation zones. This method may then be extended to other scatterometers to create a record of the location of the ice facies over time.

2. Some general observations of the temporal backscatter in the dry snow zone are provided in Chapter 3. The temporal behavior of σ^0 could be investigated further by using the estimated coefficients of the basis set generated using the KL transform.

3. Using the estimated coefficients of the basis set generated from the KL expansion, future temporal variation in σ^0 in the dry snow zone may be predicted. This could be used to improve future scatterometer calibration.

4. Based on observations in Chapter 5, the observed seasonal variation in σ^0 does not appear to be directly related to wind speed and direction. Wind could cause the seasonal variation less directly by creating wind slabs or breaking apart snow grains. Future work could investigate this.

5. An empirical analysis of the effects of spatial averaging of σ^0 in the dry snow zone on temporal variance is given. Spatially averaging σ^0 for a small region generally results in decreased temporal variance compared to a single pixel. However, increasing the size of the region can affect the temporal variance of σ^0 depending on the location of the region within the dry snow zone. Future research could investigate this.

6. The relationship between temperature and backscatter in the dry snow zone could be explored further. Further work is required to learn how temperature may cause the seasonal variation in σ^0. Electromagnetic modeling plays an important role in this. Although the estimated backscatter from the electromagnetic model in Chapter 5 tracks the general trends of σ^0 well, its accuracy could be improved by incorporating accumulation, snow grain growth, multiple layers of snow, a liquid-like layer of water at the surface, depth dependent snow density, and other backscatter dependencies on temperature. Including some of these factors in the model requires access to grain size measurements and other *in situ* data.

Bibliography

[1] F. Naderi, M. Freilich, and D. Long, "Spaceborne radar measurement of wind velocity over the ocean-an overview of the NSCAT scatterometer system," *Proceedings of the IEEE*, vol. 79, no. 6, pp. 850–866, 1991. 1

[2] H. Anderson and D. Long, "Sea ice mapping method for SeaWinds," *Geoscience and Remote Sensing, IEEE Transactions on*, vol. 43, no. 3, pp. 647–657, 2005. 1

[3] D. Long and P. Hardin, "Vegetation studies of the Amazon Basin using enhanced resolution Seasat scatterometer data," *Geoscience and Remote Sensing, IEEE Transactions on*, vol. 32, no. 2, pp. 449–460, 1994. 1

[4] D. G. Long and M. R. Drinkwater, "Greenland ice-sheet surface properties observed by the Seasat-A scatterometer at enhanced resolution," *Journal of Glaciology*, vol. 40, no. 135, pp. 213–230, 1994. 1, 2, 6, 7, 8, 9, 10, 11, 12, 25, 50

[5] W. Abdalati and K. Steffen, "Snowmelt on the Greenland ice sheet as derived from passive microwave satellite data," *Journal of Climate*, vol. 10, no. 2, pp. 165–175, 1997. 1, 2

[6] ——, "Greenland ice sheet melt extent: 1979-1999," *Journal of Geophysical Research*, vol. 106, no. D24, pp. 33 983–33 988, 2001. 2

[7] W. Tsai, J. Graf, C. Winn, J. Huddleston, S. Dunbar, M. Freilich, F. Wentz, D. Long, and W. Jones, "Post-launch sensor verification and calibration of the NASA scatterometer," *IEEE Trans. Geosci. Remote Sens.*, vol. 37, no. 3, pp. 1517–1542, May 1999. 3

[8] R. Kumar, S. Bhowmick, K. Babu, R. Nigam, and A. Sarkar, "Relative calibration using natural terrestrial targets: A preparation towards Oceansat-2 scatterometer," *IEEE Transactions on Geoscience and Remote Sensing*, vol. 49, pp. 2268–2273, 2011. 3

[9] R. Kennett and F. Li, "Seasat over-land scatterometer data. ii. selection of extended area and land-target sites for the calibration of spaceborne scatterometers," *Geoscience and Remote Sensing, IEEE Transactions on*, vol. 27, no. 6, pp. 779–788, 1989. 3

[10] J. Zec, W. Jones, and D. Long, "NSCAT normalized radar backscattering coefficient biases using homogeneous land targets," *Journal of geophysical research*, vol. 104, no. C5, pp. 11 557–11 568, 1999. 3

[11] L. Kunz and D. Long, “Calibrating SeaWinds and QuikSCAT scatterometers using natural land targets,” *Geoscience and Remote Sensing Letters, IEEE*, vol. 2, no. 2, pp. 182–186, 2005. 3

[12] M. Richards, J. Scheer, and W. Holm, *Principles of modern radar: Basic principles*, 10th ed. Raleigh, NC: SciTech Pub., 2010, vol. 1. 5

[13] I. Ashcraft and D. Long, “Comparison of methods for melt detection over Greenland using active and passive microwave measurements,” *International Journal of Remote Sensing*, vol. 27, no. 12, pp. 2469–2488, 2006. 7, 21

[14] L. Wang, M. Sharp, B. Rivard, S. Marshall, and D. Burgess, “Melt season duration on Canadian Arctic ice caps, 2000–2004,” *Geophysical Research Letters*, vol. 32, no. 19, p. L19502, 2005. 7

[15] L. Wang, M. Sharp, B. Rivard, and K. Steffen, “Melt season duration and ice layer formation on the Greenland ice sheet, 2000–2004,” *Journal of Geophysical Research*, vol. 112, 2007. 7, 8, 9, 10, 23

[16] G. Wolken, M. Sharp, and L. Wang, “Snow and ice facies variability and ice layer formation on Canadian Arctic ice caps, 1999–2005,” *Journal of Geophysical Research*, vol. 114, no. F3, p. F03011, 2009. 7, 8

[17] P. Panday, K. Frey, and B. Ghimire, “Detection of the timing and duration of snowmelt in the Hindu Kush-Himalaya using QuikSCAT, 2000–2008,” *Environmental Research Letters*, vol. 6, p. 024007, 2011. 7

[18] C. Benson, “Stratigraphic studies in the snow and firn of the Greenland ice sheet,” Ph.D. dissertation, California Institute of Technology, 1960. 7, 8

[19] I. Bhattacharya, K. Jezek, L. Wang, and H. Liu, “Surface melt area variability of the Greenland ice sheet: 1979–2008,” *Geophysical Research Letters*, vol. 36, p. L20502, 2009. 8

[20] M. Fahnestock, R. Bindschadler, R. Kwok, and K. Jezek, “Greenland ice sheet surface properties and ice dynamics from ERS-1 SAR imagery,” *Science*, vol. 262, no. 5139, pp. 1530–1534, 1993. 8, 9, 10

[21] D. Long and M. Drinkwater, “Cryosphere applications of NSCAT data,” *Geoscience and Remote Sensing, IEEE Transactions on*, vol. 37, no. 3, pp. 1671–1684, 1999. 8

[22] M. Drinkwater, “Snow and sea-ice applications of radar scatterometry.” Ankara, Turkey: Presentation at the TSMS/EUMETSAT Training Workshop. 9

[23] C. Benson, “Stratigraphic studies in the snow and firn of the Greenland ice sheet,” SIPRE Research Report, Tech. Rep. 70, 1962. 8, 9, 10, 61

[24] K. Jezek, P. Gogineni, and M. Shanableh, “Radar measurements of melt zones on the Greenland ice sheet,” *Geophysical Research Letters*, vol. 21, no. 1, pp. 33–36, 1994. 10

[25] E. Burgess, R. Forster, J. Box, E. Mosley-Thompson, R. Bromwich, R. Bales, and L. Smith, “A spatially calibrated model of annual accumulation rate on the Greenland Ice Sheet (1958–2007),” *Journal of Glaciology*, vol. 115, no. F2, p. F02004, 2010. 11, 13

[26] M. Spencer, C. Wu, and D. Long, “Tradeoffs in the Design of a Spaceborne Scanning Pencil Beam Scatterometer: Application to SeaWinds,” *IEEE Transactions on Geoscience and Remote Sensing*, vol. 35, no. 1, pp. 115–126, 1997. 13

[27] I. Ashcraft and D. Long, “The spatial response function of Seawinds backscatter measurements,” in *Proceedings of SPIE*, vol. 5151, 2003, pp. 609–618. 14

[28] W. Tsai, M. Spencer, C. Wu, C. Winn, and K. Kellogg, “SeaWinds on QuikSCAT: sensor description and mission overview,” in *Geoscience and Remote Sensing Symposium, 2000. Proceedings. IGARSS 2000. IEEE 2000 International*, vol. 3. IEEE, 2000, pp. 1021–1023. 14

[29] J. Johnson, L. Williams Jr, E. Bracalente, F. Beck, and W. Grantham, “Seasat-A satellite scatterometer instrument evaluation,” *Oceanic Engineering, IEEE Journal of*, vol. 5, no. 2, pp. 138–144, 1980. 14

[30] E. Attema and P. Lecomte, “The ERS-1 and ERS-2 wind scatterometers, system performance and data products,” in *Geoscience and Remote Sensing Symposium Proceedings, 1998. IGARSS’98. 1998 IEEE International*, vol. 4. IEEE, 1998, pp. 1967–1969. 14

[31] J. Figa-Saldana, J. Wilson, E. Attema, R. Gelsthorpe, M. Drinkwater, and A. Stoffelen, “The advanced scatterometer (ASCAT) on the meteorological operational (MetOp) platform: A follow on for European wind scatterometers,” *Canadian Journal of Remote Sensing*, vol. 28, no. 3, pp. 404–412, 2002. 14

[32] D. Long, P. Hardin, and P. Withing, “Resolution enhancement of spaceborne scatterometer data,” *IEEE Transactions on Geoscience and Remote Sensing*, vol. 31, no. 3, pp. 700–715, 1993. 14

[33] D. Early and D. Long, “Image reconstruction and enhanced resolution imaging from irregular samples,” *IEEE Transactions on Geoscience and Remote Sensing*, vol. 39, no. 2, pp. 291–302, 2001. 14

[34] D. Long and M. Drinkwater, “Azimuth variation in microwave scatterometer and radiometer data over Antarctica,” *IEEE Transactions on Geoscience and Remote Sensing*, vol. 38, no. 4, pp. 1857–1870, 2000. 16

[35] I. Ashcraft and D. Long, “Azimuth variation in microwave backscatter over the Greenland ice sheet,” in *Geoscience and Remote Sensing Symposium*, vol. 4, 2001, pp. 1779–1781. 16

[36] K. Steffen, J. E. Box, and W. Abdalati, “Greenland Climate Network: GC-Net,” *CRREL Special Report on Glaciers, Ice sheets and Volcanoes, trib. to M. Meier*, vol. 96-27, pp. 98–103, 1996. 16, 17, 18

[37] T. K. Moon and W. C. Stirling, *Mathematical Methods and Algorithms for Signal Processing*, 1st ed. New Jersey: Prentice Hall, 2000. 25, 26, 27

[38] D. Long and B. Hicks, "Standard BYU QuikSCAT and Seawinds land/ice image products," 2010. 44

[39] H. Rott, K. Sturm, and H. Miller, "Active and passive microwave signatures of antarctic firn by means of field measurements and satellite data," *Annals of Glaciology*, vol. 17, pp. 337–337, 1993. 47

[40] H. Rott and W. Rack, "Characterization of Antarctic firn by means of ERS-1 scatterometer measurements," in *Geoscience and Remote Sensing Symposium, 1995. IGARSS'95.'Quantitative Remote Sensing for Science and Applications', International*, vol. 3. IEEE, 1995, pp. 2041–2043. 47

[41] M. Ledroit, F. Remy, and J. Minster, "Observations of the Antarctic ice sheet with the Seasat scatterometer: Relation to katabatic-wind intensity and direction," *Journal of Glaciology*, vol. 39, no. 132, pp. 385–394, 1993. 47

[42] D. Bromwich, T. Parish, and C. Zorman, "The confluence zone of the intense katabatic winds at Terra Nova Bay, Antarctica as derived from airborne sastrugi surveys and mesoscale numerical modeling," *Journal of Geophysical Research*, vol. 95, no. D5, pp. 5495–5509. 47

[43] I. Ashcraft and D. Long, "Relating microwave backscatter azimuth modulation to surface properties of the Greenland ice sheet," *Journal of Glaciology*, vol. 52, no. 177, pp. 257–266, 2006. 47

[44] I. S. Ashcraft and D. G. Long, "Observation and characterization of radar backscatter over Greenland," *IEEE Transactions on Geoscience and Remote Sensing*, vol. 43, no. 2, pp. 225–237, 2005. 53

[45] D. G. Long and M. R. Drinkwater, "Azimuth variation in microwave scatterometer and radiometer data over Antarctica," *IEEE Transactions on Geoscience and Remote Sensing*, vol. 38, no. 4, pp. 1857–1870, July 2000. 53

[46] W. Dierking, S. Linow, and W. Rack, "Toward a robust retrieval of snow accumulation over the Antarctic ice sheet using satellite radar," *Journal of Geophysical Research*, vol. 117, no. D9, p. D09110, 2012. 58

[47] A. Hachikubo and E. Akitaya, "Effect of wind on surface hoar growth on snow," *Journal of Geophysical Research. D. Atmospheres*, vol. 102, pp. 4367–4373, 1997. 58

[48] S. Colbeck, "Air movement in snow due to windpumping," *J. Glaciol*, vol. 35, no. 120, pp. 209–213, 1989. 58

[49] A. S. Thut, "Snow density and its underlying variables," Atmospheric and Oceanic Sciences, University of Wisconsin-Madison, Tech. Rep., 2006. 61, 72, 73

[50] A. Judson, N. Doesken, and C. Center, “Density of freshly fallen snow in the central Rocky Mountains,” *Bulletin of the American Meteorological Society*, vol. 81, no. 7, pp. 1577–1588, 2000. 61, 72, 73

[51] H. Bluhm, D. Ogletree, C. Fadley, Z. Hussain, and M. Salmeron, “The premelting of ice studied with photoelectron spectroscopy,” *Journal of Physics: Condensed Matter*, vol. 14, p. L227, 2002. 61

[52] M. Goertz, X. Zhu, and J. Houston, “Exploring the liquid-like layer on the ice surface,” *Langmuir*, vol. 25, no. 12, pp. 6905–6908, 2009. 61

[53] F. Ulaby, R. Moore, and A. Fung, *Microwave Remote Sensing: Active and Passive.* Norwood, Massachusetts: Artech House, 1986, vol. 1. 72, 74, 75

[54] ——, *Microwave Remote Sensing: Active and Passive.* Norwood, Massachusetts: Artech House, 1986, vol. 2. 72, 74, 75

[55] ——, *Microwave Remote Sensing: Active and Passive.* Norwood, Massachusetts: Artech House, 1986, vol. 3. 72, 73, 74, 75

[56] D. Stillman and R. Grimm, “Electrical properties of ice and implications for solar system exploration,” in *Lunar and Planetary Institute Science Conference Abstracts*, vol. 39, 2008, p. 2277. 73

Appendix A

Spatial Averaging and the Correlation Coefficient

In this appendix, the effects of averaging N random variables on the correlation coefficient with another random variable is analyzed. This question arises in the context of spatially averaging and then correlating σ^0 and temperature. The analysis is performed first for $N = 2$ and then for arbitrary N. The results are then verified by simulation for the $N = 2$ case.

A.1 Analysis for $N = 2$

Let X_1 and X_2 be positively correlated random variables. Let Y also be a random variable correlated with both X_1 and X_2. The Pearson correlation coefficient of the random variables X_k and Y is defined as

$$\rho_{X_k Y} = \frac{\mathrm{Cov}(X_k, Y)}{\sigma_{X_k}\sigma_Y} \tag{A.1}$$

where σ_{X_k} and σ_Y are the standard deviations of X_k and Y. If $Z = \frac{X_1+X_2}{2}$, then

$$\begin{aligned}\sigma_Z^2 &= \mathrm{Var}\left(\frac{X_1+X_2}{2}\right)\\ &= \frac{1}{4}(\sigma_{X_1}^2 + \sigma_{X_2}^2 + 2\mathrm{Cov}(X_1, X_2))\\ &= \frac{1}{4}(\sigma_{X_1}^2 + \sigma_{X_2}^2 + 2\sigma_{X_1}\sigma_{X_2}\rho_{X_1X_2}).\end{aligned} \tag{A.2}$$

The covariance of Z and Y is then

$$\begin{aligned}\mathrm{Cov}(Z, Y) &= E[ZY] - E[Z]E[Y]\\ &= \frac{1}{2}(E[X_1Y] + E[X_2Y]\\ &\quad - E[X_1]E[Y] - E[X_2]E[Y])\\ &= \frac{1}{2}(\mathrm{Cov}(X_1, Y) + \mathrm{Cov}(X_2, Y))\\ &= \frac{1}{2}\sigma_Y(\rho_{X_1Y}\sigma_{X_1} + \rho_{X_2Y}\sigma_{X_2}).\end{aligned} \tag{A.3}$$

The correlation coefficient of Z and Y then becomes

$$\rho_{ZY} = \frac{\rho_{X_1Y}\sigma_{X_1} + \rho_{X_2Y}\sigma_{X_2}}{\sqrt{\sigma_{X_1}^2 + \sigma_{X_2}^2 + 2\sigma_{X_1}\sigma_{X_2}\rho_{X_1X_2}}}. \tag{A.4}$$

If it is assumed that $\sigma_{X_1} \approx \sigma_{X_2}$, then the correlation coefficient becomes

$$\rho_{ZY} = \frac{\rho_{X_1Y} + \rho_{X_2Y}}{\sqrt{2(1 + \rho_{X_1X_2})}}. \tag{A.5}$$

Since X_1 and X_2 are positively correlated, $0 < \rho_{X_1X_2} < 1$, which gives bounds on ρ_{ZY} as

$$\frac{|\rho_{X_1Y} + \rho_{X_2Y}|}{2} < |\rho_{ZY}| < \frac{|\rho_{X_1Y} + \rho_{X_2Y}|}{\sqrt{2}}. \tag{A.6}$$

These results can be applied in the following manner. Assume that X_1 and X_2 represent σ^0 at two nearby pixels. Since the pixels are adjacent, it is likely that $\sigma_{X_1} \approx \sigma_{X_2}$ and $0 < \rho_{X_1X_2} < 1$ which means that Eq. (A.6) is valid. Equation (A.6) then shows that if σ^0 is averaged for these two adjacent pixels and then correlated with air temperature, the resulting correlation coefficient will be greater than the average of the individual correlation coefficients.

A.2 Analysis for Arbitrary N

This can be extended to $N \geq 2$. Define $Z_N = \frac{1}{N}\sum_{n=1}^{N} X_n$ where each X_n is a random variable positively correlated with the others. Then the variance of Z_N is

$$\begin{aligned}\sigma_{Z_N}^2 &= \frac{1}{N^2}\sum_{n=1}^{N}\sum_{m=1}^{N}\mathrm{Cov}(X_n, X_m)\\ &= \frac{1}{N^2}\sum_{n=1}^{N}\sum_{m=1}^{N}\rho_{X_nX_m}\sigma_{X_n}\sigma_{X_m}\end{aligned} \tag{A.7}$$

and the covariance of Z_N and Y is

$$\begin{aligned}\mathrm{Cov}(Z_N, Y) &= \frac{1}{N}\sum_{n=1}^{N}\mathrm{Cov}(X_n, Y)\\ &= \frac{\sigma_Y}{N}\sum_{n=1}^{N}\sigma_{X_n}\rho_{X_nY}.\end{aligned} \tag{A.8}$$

The correlation coefficient is then

$$\rho_{Z_NY} = \frac{\sum_{n=1}^{N}\sigma_{X_n}\rho_{X_nY}}{\sqrt{\sum_{n=1}^{N}\sum_{m=1}^{N}\rho_{X_nX_m}\sigma_{X_n}\sigma_{X_m}}}. \tag{A.9}$$

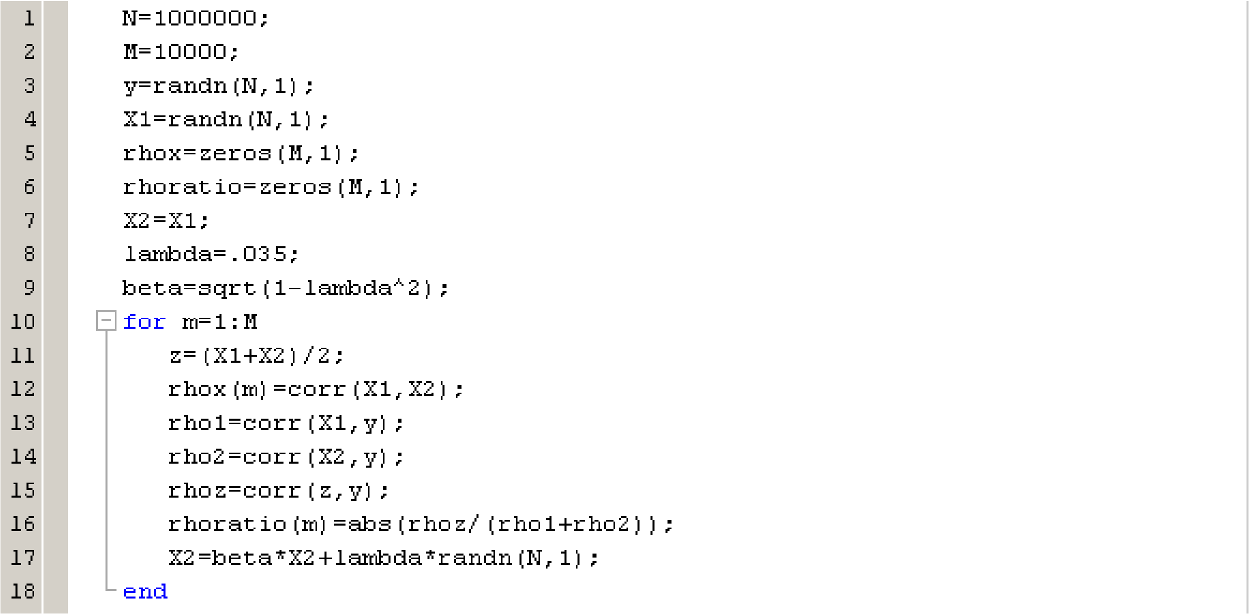

```
N=1000000;
M=10000;
y=randn(N,1);
X1=randn(N,1);
rhox=zeros(M,1);
rhoratio=zeros(M,1);
X2=X1;
lambda=.035;
beta=sqrt(1-lambda^2);
for m=1:M
    z=(X1+X2)/2;
    rhox(m)=corr(X1,X2);
    rho1=corr(X1,y);
    rho2=corr(X2,y);
    rhoz=corr(z,y);
    rhoratio(m)=abs(rhoz/(rho1+rho2));
    X2=beta*X2+lambda*randn(N,1);
end
```

Figure A.1: MATLAB code for the simulation.

If it is assumed that $\sigma_{X_n} \approx \sigma_{X_m}$ for all n and m and that $\rho_{X_n X_m} \approx \rho_X$ for all $n \neq m$, then $\rho_{Z_N Y}$ simplifies to

$$\rho_{Z_N Y} = \frac{\sum_{n=1}^{N} \rho_{X_n Y}}{\sqrt{N + (N-1)N\rho_X}}. \tag{A.10}$$

Since the X_n's are positively correlated with each other, then $0 < \rho_X < 1$. This means that

$$\frac{1}{N}\left|\sum_{n=1}^{N} \rho_{X_n Y}\right| < |\rho_{Z_N Y}| < \frac{1}{\sqrt{N}}\left|\sum_{n=1}^{N} \rho_{X_n Y}\right|. \tag{A.11}$$

As an example, this shows that for adjacent pixels, the magnitude of the correlation coefficient of the spatial average of σ^0 with temperature is greater than the magnitude of the spatial average of the individual correlation coefficients.

A.3 Simulation for $N = 2$

To verify the analysis, the $N = 2$ case is simulated. Figure A.1 gives the MATLAB code to run the simulation. Two zero-mean unit variance normally distributed random vectors with length 1000000 ($\mathbf{Y}$ and $\mathbf{X_1}$) are generated. The vector $\mathbf{X_2}$ is initially equal to $\mathbf{X_1}$ meaning $\rho_{X_1 X_2} = 1$. The correlation coefficient $\rho_{X_1 X_2}$ is slowly decreased to zero by generating a zero-mean low variance normally distributed random vector multiple times and

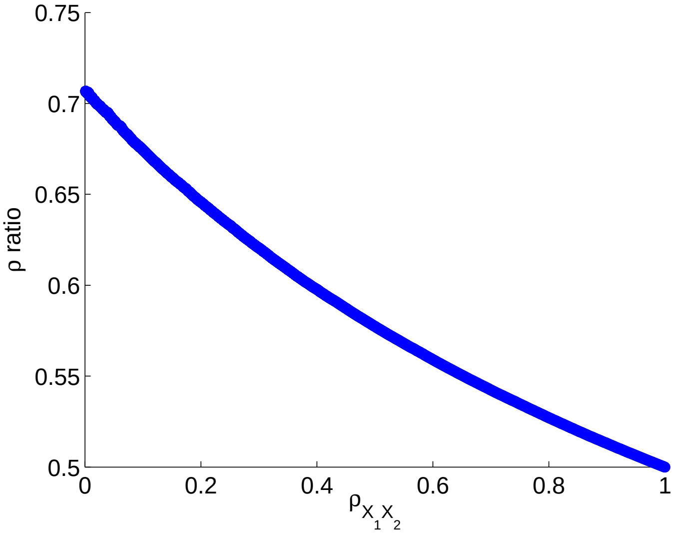

Figure A.2: Simulated results for the correlation analysis where $N = 2$. The value ρ ratio is defined in Eq. (A.12).

adding it to $\mathbf{X_2}$. The value ρ ratio is calculated at each step where

$$\rho \text{ ratio} = \frac{|\rho_{ZY}|}{|\rho_{X_1Y} + \rho_{X_2Y}|}. \tag{A.12}$$

Then from the previous sections,

$$\frac{1}{2} < \rho \text{ ratio} < \frac{1}{\sqrt{2}}. \tag{A.13}$$

Figure A.2 gives the results for the simulation which agree with Eq. (A.13).

A.4 Conclusion

The results of this appendix demonstrate that spatial averaging can artificially increase the correlation coefficient. According to Fig. A.2, this occurs the most when the pixels are not highly correlated. This suggests that to mitigate noise effects on the correlation coefficient, a spatial average of a smaller and more correlated region gives more accurate results than using the spatial average of the entire ice sheet.

Appendix B

Diurnal Correlation of Temperature and Backscatter

If seasonal variation in temperature is driving the seasonal variation in σ^0 in the dry snow zone, then diurnal variation in temperature may create diurnal variation in σ^0. In this appendix, the diurnal relationship between temperature and σ^0 in the dry snow zone is explored.

B.1 Data

For each day and polarization, there are three QuikSCAT SIR images of Greenland based on the time of the satellite passes. One image uses all the available passes to calculate σ^0. Data from all-pass images are used throughout this entire thesis. The other images calculate σ^0 from passes categorized as either morning or evening passes. The morning and evening images can be used to study diurnal variations in σ^0 in the dry snow zone.

Unfortunately, the morning images of Greenland include only passes that occur in the early morning. Additionally, all the evening passes occur late in the day. This means that there may not be much change in temperature between the morning and evening images. To improve the temporal resolution in σ^0, midday images from the SeaWinds on ADEOS scatterometer are used (referred to as SeaWinds hereafter). SeaWinds operated from JD 100 to JD 297 in 2003 and is nearly identical in specifications to QuikSCAT. However its orbital pattern causes it to pass over Greenland in the evening and midday. Combining the midday SeaWinds images with the evening and morning QuikSCAT images gives a finer temporal resolution (3 samples/day) in σ^0. Temperature records from AWS are then used with this sequence of images to study diurnal variations in temperature and σ^0 in the dry snow zone.

B.2 Results

Table B.1 provides the correlation coefficients of temperature and σ^0 at AWS in the dry snow zone in 2003. The values in the first column use the QuikSCAT all-pass images and the average daily temperature to calculate the correlation coefficient. This gives a baseline for comparison. These values are slightly lower than those given in Table 5.5. This is likely due to the shorter record used in Table B.1.

The values in the second column use the diurnal sequence of σ^0 and the temperature measurement taken at the corresponding pixel times to calculate the correlation coefficient. An increase in the magnitude of the correlation coefficient in this column compared to the first column would suggest that diurnal variations in temperature are correlated with diurnal variations in σ^0. However, this is not the case. The magnitude of the correlation coefficient is generally smaller when the diurnal sequence is used. The decrease in magnitude

Table B.1: Correlation coefficients of temperature and σ^0 at stations in the dry snow zone in 2003 from JD 100 to JD 297. The all-pass column uses all-pass image data and average daily temperature while the diurnal column uses the diurnal sequence of σ^0 and the temperature measurement taken at the corresponding pixel times. The delta column uses the change in σ^0 and the change in temperature.

AWS	All-pass	Diurnal	Delta
5	-0.558	-0.394	-0.173
6	-0.383	-0.346	-0.311
7	-0.563	-0.406	-0.141
12	-0.499	-0.370	-0.153
14	-0.291	-0.307	-0.279

may be caused by noise. The SIR algorithm essentially temporally averages σ^0. Averaging the backscatter mitigates the effects of noise. Therefore images created from more passes generally have less noise. It is possible that using morning, evening, and midday passes buries some of the backscatter dependence on temperature in the higher noise level of subdaily versus daily samples, resulting in a decrease in the correlation coefficient.

Additionally, some of the decrease in the magnitude of the correlation coefficient may be caused by using unaveraged air temperature data. Backscatter in snow depends on the snow conditions which are affected by snow temperature. Snow temperature is generally affected more by the average air temperature than the air temperature at a single point in time. This may account for some of the decrease in the magnitude of the correlation coefficient.

The values in the third column use the change in σ^0 and the change in temperature to calculate the correlation coefficient. Comparing the change in the two data sets mitigates the correlation due to the seasonal cycle. Table B.1 shows that the magnitude of the correlation coefficient between these two parameters is low but statistically significant. This suggests that diurnal variations in temperature may drive small diurnal variations in σ^0. However, noise appears to limit the analysis.

Figure B.1 shows plots of temperature, backscatter, the change in temperature, and the change in backscatter for a twenty day period in 2003. These plots give an example of the relationship between temperature and backscatter. Figures B.1(a) and B.1(c) show that there is a negative correlation between temperature and σ^0. This is observable around JD 147 where lower temperatures are associated with higher backscatter. Similarly, Figs. B.1(b) and B.1(d) show that there is a negative correlation between the change in temperature and the change in σ^0. This is observable between JD 140 and JD 145 where large (small) changes in temperature are associated with large (small) changes in σ^0. However, these relationships are not observable everywhere in Fig. B.1. This is likely due to the explanations given previously.

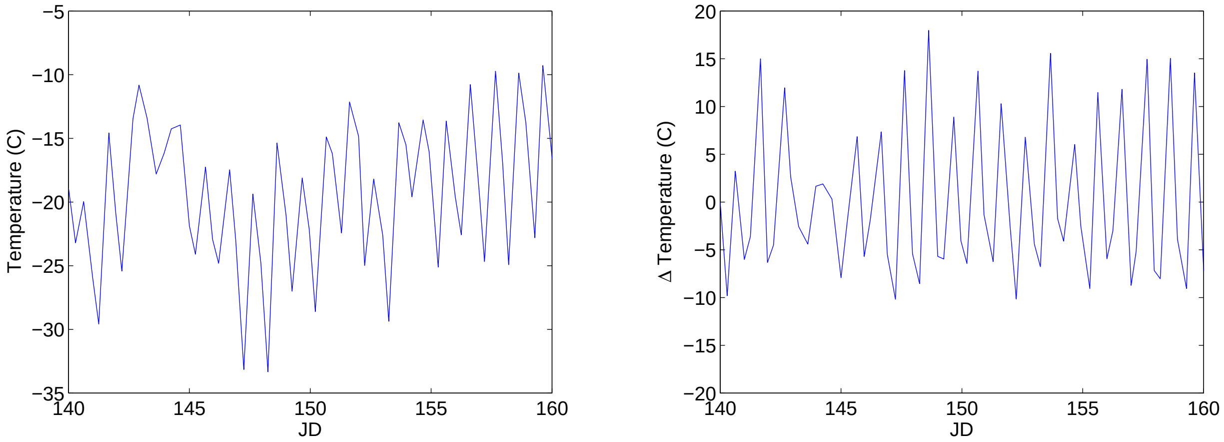

(a) Air temperature

(b) Change in air temperature

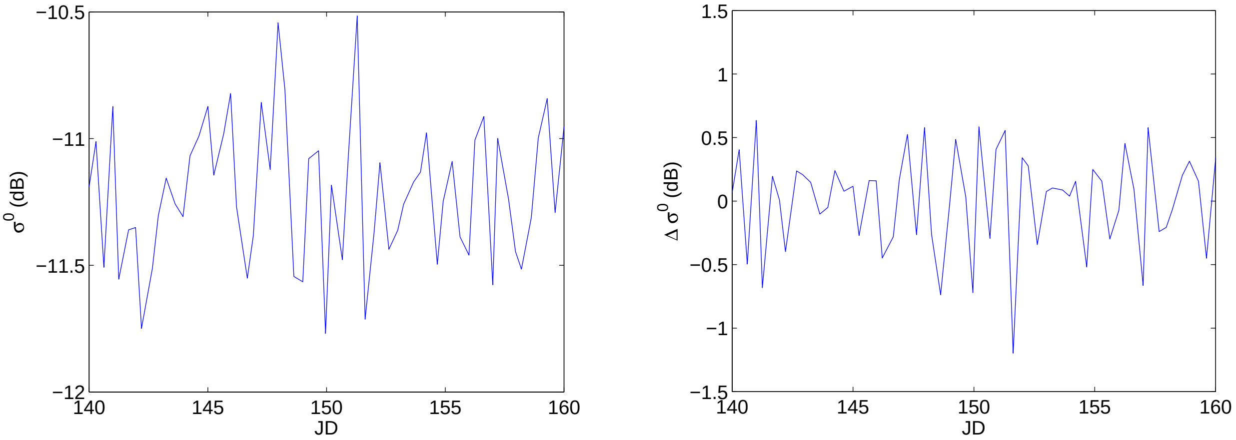

(c) Backscatter

(d) Change in backscatter

Figure B.1: Plots at the summit in 2003 from JD 140 to JD 160 of (a) air temperature, (b) the change in air temperature, (c) σ^0, and (d) the change in σ^0.

B.3 Summary

The correlation coefficient between the change in temperature and the change in σ^0 suggest that diurnal variations in temperature may drive small diurnal variations in σ^0. However, the correlation is quite low. Additionally, the correlation coefficient of the diurnal sequence of temperature and σ^0 is lower than the correlation coefficient of all-pass images of σ^0 and the average daily temperature. This may be due to the higher noise level in images used in the diurnal cycle as well as the effects of using unaveraged air temperature to calculate the correlation coefficient.